Small-scale power generation using paper based fuel cells

Sweta Lal

Roll number: CH14RESCH11002

A Thesis Submitted to

Indian Institute of Technology Hyderabad

In Partial Fulfillment of the Requirements for

the Degree of

Doctor of Philosophy

भारतीय प्रौद्योगिकी संस्थान हैदराबाद
Indian Institute of Technology Hyderabad

Department of Chemical Engineering

Indian Institute of Technology Hyderabad

Sangareddy, Hyderabad- 502 285

September 2018

Declaration

I declare that this written submission represents my ideas in my own words, and where ideas or words of others have been included, I have adequately cited and referenced the original sources. I also declare that I have adhered to all principles of academic honesty and integrity and have not misrepresented or fabricated or falsified any idea/data/fact/source in my submission. I understand that any violation of the above will be a cause for disciplinary action by the Institute and can also evoke penal action from the sources that have thus not been properly cited, or from whom proper permission has not been taken when needed.

Sweta Lal

(Signature)

SWETA LAL

Sweta Lal

CHI4RESCHII002

(Roll No.)

Approval Sheet

This thesis entitled **Small-scale power generation using paper based fuel cell** by Sweta Lal is approved for the degree of Doctor of Philosophy from IIT Hyderabad.
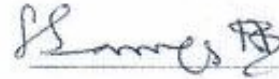
Prof Sampath Srinivasan

Dept. of Chemistry, IISc Bangalore

(Examiner 1)
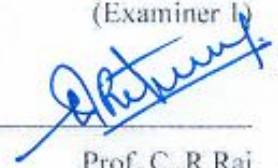
Prof. C. R Raj

Dept. of Chemistry, IIT Kharagpur

(Examiner 2)
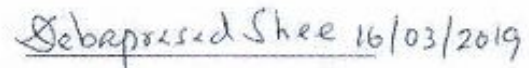
Prof. Debaprasad Shee

Dept. of Chemical Engineering, IIT Hyderabad

(Internal Examiner)
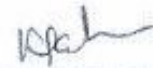
Prof. Kirti Chandra Sahu

Dept. of Chemical Engineering, IIT Hyderabad

(Adviser/Guide)
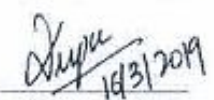
Prof. Vinod Janardhanan & Prof. Deepa Melepurath

IIT Hyderabad

(Co-Advisers)
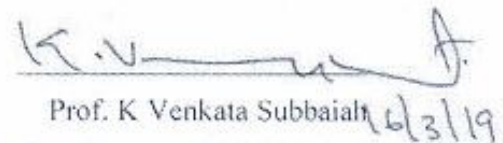
Prof. K Venkata Subbaiah

Dept. of Mechanical and Aerospace Engineering, IIT Hyderabad

vi

(Chairman)

Acknowledgements

First and foremost, I would like to express my deepest gratitude to my supervisor Prof. Kirti Chandra Sahu. He has always been the constant source of support and motivation throughout my journey at IIT Hyderabad. His tips and guidance has helped me in shaping up my research skills. Also, I am extremely grateful to my co supervisor Dr. Vinod Janardhanan, whose valuable ideas and suggestions have helped me perform my experiments in order to obtain fruitful results. His calmness and positive approach about every problem has always been inspirational for me. Next, I would to like thank my co-supervisor Dr. M Deepa from the department of chemistry. She has always been supportive about my ideas and hepled me out in understanding the concepts of electrochemistry. Her appreciations has always motivated me to improve my work.

I am indebted to all of my supervisors, who have stood like pillars in my tough times and always encouraged to perform better. This journey would not have been possible without their immense support and faith in me.

I am grateful to the members of my doctoral committee Dr. Ch. Subrahmanyam and Dr. Praveen Meduri, whose valuable suggestions and tips has helped me improve my understanding towards my research area.

I am extremely thankful to the departments of chemical engineering and chemistry, IIT Hyderabad, for providing me the necessary facilities to perform my research.

I would like to express my sincere thankfulness to my parents and family, whose blessings have always kept me going. I can't thank them enough for being so supportive towards my work. Also, I want to thank my husband, because of whose support and guidance, I have been able to accomplish this journey. He has always encouraged me to pursue my dreams and taught me the importance of higher education.

Among my colleagues I want to thank Dr. Premlata, Mounika Balla, P V Prakash and Vivek Pawar, from the department of chemical engineering and Dr. Naresh, Radha Reddy, Satish and Aparajita from the department of chemistry. They have been extremely helpful and co-operative towards me and my work. Also, I would like to thank Rajat Verma, Subrata Chandra and Parmish Kaur, for working with them was another journey of learning and improving my research work.

Finally, I am grateful to the Almighty for blessing me with this life and whatever little I have achieved till

now.

Dedication

This thesis is dedicated to MAA.

Abstract

Background

Paper based microfluidics has emerged as a promising technology for the development of low cost energy devices such as, paper based fuel cells for powering point-of-care (POC) diagnostic devices. These devices include glucometers, pregnancy detection kits etc. The diagnostic devices that are used in the environmental, health monitoring, micro/nano electromechanical systems (MEMS), wireless electronics etc. require power for a short duration and in milli-nano watt range for the analysis and display of the results/diagnosis. These are referred to as micro-nano devices (MNS). These devices are low power consuming and require the electrical input for a few seconds to a few minutes and are usually disposed after one-time use.

Currently Li-ion batteries are used as the source of power in these devices. Apart from batteries other potential powering sources are solar cells and microbial fuel cells, however these have certain limitations associated with them. For instance, functioning of solar cells is dependent on the availability of sunlight, microbial fuel cells deliver power in the micro-watt ranges and require strict environment control for their operation. The use of batteries in single-use, disposable devices is not recommended as it leads to under utilization of stored energy and resourceful materials. Moreover, keeping in view of the growing energy demand which may surpass the available energy sources, finding cost-effective powering sources for low-power requiring devices is necessary.

Micro-fuel cells can be thought of as an alternative to the aforementioned power sources. However, in general fuel cells require metering devices for the supply of fuel and oxidant, which makes the overall system cumbersome. Paper can transport liquid fuels due to its remarkable intrinsic properties such as, porosity and capillarity. Furthermore, paper is cheap, easily available, easy to shape and dispose (biodegradable), without posing any environmental threats. Due to these benefits paper can easily provide the platform for the functioning of energy devices which are based on liquid fuel, oxidants and electrolytes. Due its intrinsic transport properties, paper based fuel cells don't need any external pumping mechanism or ancillary parts to pump the fluids through the system. This not only reduces the fabrication and operational complexity to a great extent, but also minimizes the overall cost.

The development and fabrication of various paper-based fuel cells in different architectures,

has been extensively studied by researchers recently. However, some of these either use expensive noble metal catalyst (Pt, Au, Pd) to attain high power densities or micro-organisms (bacteria) for their operation (as in microbial fuel cell), which limits their application in MNSs.

The primary objective of this thesis is to develop, fabricate and characterize low-cost, easy to use and disposable paper based fuel cells for powering micro-nano devices at room temperature.

Motivation and objectives

The main objective of the work is to fabricate and characterize fuel cells supported on paper. The specific objectives are

1. Design paper supported fuel cells with different geometrical configuration to limit the fuel and oxidant cross over to the opposite electrodes.

2. Identify different fuel oxidant pairs to form the anolyte and catholyte that can deliver high theoretical standard potentials.

3. Characterize various electrodes and catalyst that can improve the cell performance for a given redox pair.

4. Optimize the fuel concentration and catalyst loading to achieve the best performance.

5. Characterize the performance of the cell with and without ion conducting membrane and study the performance stability.

6. Demonstrate the potential of the paper supported cell for practical applications by lighting a 3 mm LED with a few drops and anolyte and catholyte.

Cell fabrication

The paper based fuel cells reported in this thesis are based out of Whatman filter paper (ashless 42) and function by discharging the anolyte (fuel and electrolyte) and catholyte (oxidant and electrolyte) manually using dropper, near the electrodes. This thesis investigates different types of fuels such as, formic acid, hydrazine monohydrate, methanol and ethanol, with two paper based fuel cell configurations have been investigated in this thesis, as mentioned below:

- U-shaped membraneless paper based fuel cell

- T-shaped paper based fuel cell with PAM/H$^+$ and Na-PSS gel, acting as the electrolyte/membrane.

In the membraneless configuration, a 7 cm long paper strip with a width of 1.4+d$_s$ cm serves as the medium of flow for the fluids. In order to delay the mixing and cross-over of the anolyte and catholyte a thin slit measuring 3.5 cm in length with varying width (2 mm, 4 mm and 6 mm)is made, this results in two paper strips separated till the mid-length, as shown in the schematic in Fig. 2.6 (a). Graphite sheets of area 0.35 cm^2 serve as the electrodes and are placed on either sides of the strip and an absorbent pad is placed at the end of the strip to absorb the excess fluids. The whole assembly is placed on a microslide. In the T-shaped configuration two 7 cm long L-shaped paper strips are placed on a microslide at distance of 0.2 cm, and conjoined by a PAM/H$^+$ or Na-PSS gel in between. The electrodes and current collector consist of carbon cloth and stainless steel plates respectively. A schematic representation of the cell assembly is shown in Fig. 2.6 (b).

Organization of thesis

This thesis contains seven chapters.**Chapter-1** includes a detailed discussion on micro-nano devices, history, working principle and different types of fuel cells. The motivation and objective of the thesis is also discussed in this chapter. **Chapter-2** discusses the state of the art of various types of laminar flow and paper based fuel cells, reported in literature. In **Chapter-3** the fabrication and characterization of membraneless paper based formic acid fuel cells is investigated. **Chapter-4** contains the fabrication and characterization of membraneless paper based fuel cells with hydrazine hydrate as the fuel, Cu NPs, f-MWCNTs and Cu NPs@f-MWCNTs as the catalysts. In **Chapter-5** cell performance of a T-shaped cell with a polyacryl amide gel/membrane is studied. Methanol is the fuel and NiCo$_2$O$_4$, N-rGo and NiCo$_2$O$_4$@N-rGo spherical flowers are implemented as the catalysts. The practical application of the cell is demonstrated by illuminating an LED. The experimental results are validated using a model based on Butler-Volmer equations. **Chapter-6** investigates the cell performance of ethanol-based T-shaped paper cell. MoO$_3$ NRs are used as the catalysts and the practical application of the cell is demonstrated by illuminating an LED. Finally **Chapter-7** summarizes the thesis and enlists the future scope of this work.

Brief discussion of the results

Membraneless paper-based formic acid-permanganate fuel cell

The performance of the membraneless paper based fuel cell employing different concentrations of formic acid (HCOOH), i.e., 6 M, 8 M and 10 M, as the fuel with 1 M $KMnO_4$ as the oxidant, is studied in this chapter. The anolyte and catholyte are formed by mixing 4 M H_2SO_4 with the fuel and oxidant. Graphite sheets without any catalysts serves as the electrodes. The best cell performance is determined by the dc-polarization curves obtained at different HCOOH concentrations while keeping the anolyte concentration constant at 1 M $KMnO_4$ in 4 M H_2SO_4.

The maximum power density of 0.57 mW cm^{-2} is attained at 8 M HCOOH at 0.77 V. The cell at this concentration delivers an OCV of 1.3 V, which is lower than the theoretical OCV of 1.76 V. The decrease in OCV is due to the eventual cross-over and diffusion of the fuel and oxidant across the slit. Therefore, in order to understand the effect of the slit width on the cell performance, dc-polarization curves are recorded for varying slit widths, and it found concluded that a slit width of 4 mm delivers the maximum power density. Similarly, the positioning of electrodes near and away from the end of the slit can also effect the cell performance as this affects the Ohmic resistance due to increase/decrease of the diffusion path length for the ions migrating from the anode to the cathode or vice-versa. To this end, experiments are done by changing the electrode position, and it is found that the best cell performance is obtained by placing the electrodes 1 cm away from the slit. In addition to these, electrochemical impedance spectroscopy (EIS) studies are also done at 6 M, 8 M, 10 M and 12 M HCOOH at OCV, which reveal that the reaction kinetics are sluggish due to the slow oxidation rates of HCOOH and $KMnO_4$ on graphite. The corresponding bode plots exhibit that the phase angle lies between -25 and -35 degrees for all HCOOH concentrations, at the characteristic frequency. The EIS plot for 8 M HCOOH at 0.77 V shows high polarization resistance, depicting slow reaction kinetics at operating voltage.

Paper based hydrazine monohydrate-permanganate fuel cells

Although the cell performance achieved by the HCOOH-H_2SO_4-$KMnO_4$ based paper cell is sufficient to power MNSs which require power in milli-nano watt ranges, the cell performance can be enhanced by changing the fuel-oxidant pair with high theoretical OCV and also by incorporating different catalysts that can ameliorate the oxidation kinetics of the fuel. Therefore, hydrazine monohydrate ($N_2H_4.H_2O$) is chosen as the next fuel, since it has a high volumetric energy density of 5.4 kWh l^{-1} as compared to formic acid (1.75 kWh l^{-1}), more negative oxidation potential of -1.21 V.

The experimental studies are performed on the same membraneless configuration as reported in Chapter 3, except,s the electrodes in this case consist of carbon cloth with stainless steel plate current collectors. The anolyte is a mixture of varying concentrations of $N_2H_4.H_2O$ (4 M, 6 M, 8 M) in 4 M NaOH and the catholyte is a mixture of 1 M $KMnO_4$ in 4 M H_2SO_4. Cu-NPs, f-MWCNTs and Cu-NPs@f-MWCNTs composites loaded on carbon cloth are used as catalysts/electrodes to improve the cell performance. Based on this analysis it is found that, the average particle size of the Cu-NPs range from 8-30 nm and in the composite these adhere to the fibrillar structures of the f-MWCNTs, in the form aggregates. Prior to studying the cell performance with catalysts, the fuel concentration is optimized and it is found that the cell delivered the maximum power density of 1.16 mW cm^{-2} with 6 M $N_2H_4.H_2O$.

For determining the best the cell performance in the presence of catalysts, experiments are performed with different catalyst combinations at the anode and cathode. A cell with Cu-NPs@f-MWCNTs loaded anode and f-MWCNTs loaded cathode delivers a maximum power density of 3.57 mW cm^{-2}. This is due to the good catalytic activity of Cu-NPs towards hydrazine oxidation in alkaline medium and the enhanced effective electrochemical area offered by the f-MWCNTs. Cu NPs are not stable in acidic medium, but f-MWCNTs are stable in both acidic and alkaline medium. The synergistic effects of the Cu-NPs and f-MWCNTs lead to better cell performance. In addition to this, the paper cell in this configuration has a stable OCV sustained for more than 10 minutes. It can regenerate its current density from a perishing value to its original magnitude of 4.5 mA cm^{-2} at an operating voltage of 0.9 V. The EIS studies show that 4 M $N_2H_4.H_2O$ has the least Ohmic resistance. Thus, the incorporation of low cost catalysts such as Cu-NPs and f-MWCNTs, cheap and easily available materials such as paper, carbon cloth, stainless steel plates for the device fabrication and the sustainable performance attained by the paper based hydrazine monohydrate fuel cells, renders it as an apposite candidate for a cost-effective on-board energy source for POC diagnostic devices.

Methanol-based fuel cell on paper support with N-doped graphene/nickel cobaltite composite catalyst

In order to explore the capability of the paper based fuel cells to power the MNSs, a demonstration of its application is presented in Chapter 5 and 6 of the thesis, where methanol and ethanol are used as fuel, respectively. Methanol is low cost, easily available and can deliver sufficient power density at room temperature. The experimental studies are performed on the T-shaped cell architecture, with carbon cloth electrodes and stainless steel plate current

collectors, and the setup is shown in Fig. 5.1.

Here, methanol is implemented as the fuel and PAM/H$^+$ gel has been used as the membrane to prevent the mixing and cross-over of the fuel and oxidant and to facilitate the ion transportation between the electrodes. The catholyte consists of 1 M KMnO$_4$ and 4 M H$_2$SO$_4$ through all the experiments, while the anolyte has varying concentrations of methanol i.e., 2 M, 4 M and 6 M in 4 M NaOH. For attaining better power densities NiCo$_2$O$_4$ hollow micro-spheres, N-rGO and a composite of NiCo$_2$O$_4$@N-rGO are employed as catalyst in the paper cell.

As a result of which, the cell fed with 4 M methanol delivers a maximum power density of 4.67 mW cm^{-2} with NiCo$_2$O$_4$@N-rGO composite containing 10 wt% N-rGO, present at both the electrodes. This cell could regenerate its decaying current density thrice upon replenishing it with fresh anolyte and catholyte. This exhibits the regenerative ability and re-usability of the paper based methanol fuel cell. A stack of two such cells (Fig. 5.14) connected in series could illuminate an LED for about 30 minutes, demonstrating its practical utility for powering low power requiring devices. In addition to this, a simple mathematical model is also formulated based on Butler-Volmer equation to predict the current densities at different methanol concentrations. The results obtained from the model where validated with the experimentally obtained current densities. The values predicted by the mathematical model and the experiments show good agreement.

Ethanol-dichromate based fuel cells on a paper substrate

Unlike the previous studies reported in the thesis, wherein potassium permanganate serves as the oxidant, here potassium dichromate is used as the oxidant along with ethanol to form the redox couple. In this study, we have developed another novel paper based fuel cell system with fairly high performance. This system is based on the T-shaped cell architecture as reported in Chapter 5 of the thesis, but with entirely new set of components, as shown in Fig. 6.1.

Here, ethanol is the fuel, K$_2$Cr$_2$O$_7$ is the oxidant, H$_2$SO$_4$ is the electrolyte, proton conducting poly(4- styrenesulfonate) (Na-PSS) gel serves as the membrane and hydrothermally synthesized MoO$_3$ nanorods (NRs) loaded carbon cloth are the electrodes. The Na-PSS gel is a cheaper substitute for Nafion and has an ionic conductivity of 0.063 S cm^{-1}. The electrodes are loaded with 0.18 mg cm^{-2} of MoO$_3$ NRs. 4 M ethanol and 0.3 M K$_2$Cr$_2$O$_7$ (both in 4 M H$_2$SO$_4$), attains a power density of 6.32 mW cm^{-2} and a stable OCV of 1.42 V. The cell performance with MoO$_3$ NRs is also compared with Ag NPs synthesized by microwave

irradiation, where the latter delivers a relatively power density of 5.06 mW cm^{-2}, depicting that the MoO$_3$ NRs have better catalytic activity than the noble metal catalyst. Finally, in order to demonstrate its practicality for powering micro-analytical systems, a stack of two cells (Fig. 6.15 (a)) is assembled on acrylic sheets. This stack could illuminate an LED for over 40 minutes. In addition to this, the stack was left unused for 24 hours, and could illuminate the LED successfully on replenishing with anolyte and catholyte. These studies justify the practical applicability and re-usability of the above reported fuel cell systems, for powering micro-nano devices cost-effectively.

A comparison of the cell performances across all the systems using formic acid, hydrazine hydrate, methanol and ethanol is presented in Fig. 1.
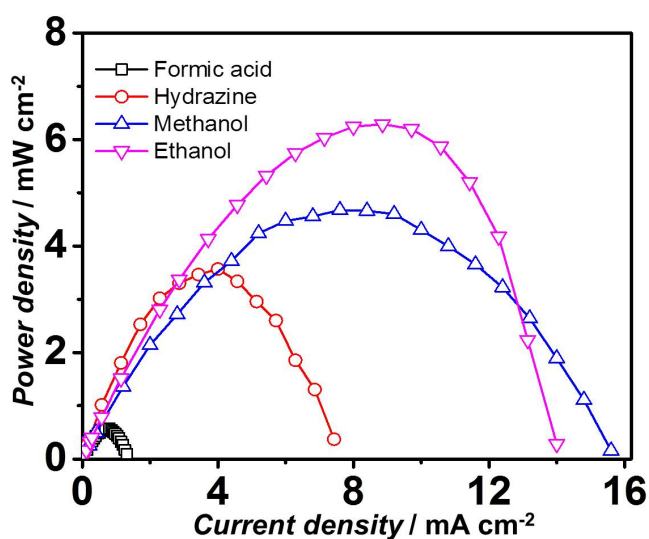
Figure 1: Comparison of the performance of various paper based fuel cells with formic acid, hydrazine hydrate, methanol and ethanol as fuel

List of publications

1. **S Lal**, V M Janardhanan, M Deepa, A Sagar, K C Sahu, Low cost environmentally benign porous paper based fuel cells for micro-nano systems, J. Electrochem. Soc., 162 (14), F1402-F1407, 2015.

2. **S Lal**, M Deepa, V M Janardhanan, K C Sahu, Paper based hydrazine monohydrate fuel cells with Cu and C composite catalysts, Electrochim Acta, 232, 262-270, 2017.

3. S Chandra (equal contribution), **S Lal (equal contribution)**, V M Janardhanan, K C Sahu, M Deepa, Regenerative ethanol based fuel cell on paper support, J. Power sources, 396, 725733, 2018.

4. Rajat Verma, **S Lal**, M Deepa, V M Janardhanan, K Chandra Sahu, Sodium percarbonate based, mixedmedia fuel cells supported on paper with gold/nickel oxide ChemElectroChem, 4 (2), 310-319, 2016.

5. **S Lal**, V M Janardhanan, M Deepa, K C Sahu, Experimental and modeling studies of paper based methanol, ECS transactions, 80, 843-849, 2017.

6. **S Lal**, V M Janardhanan, K C Sahu, M Deepa, Methanol-based fuel cell on paper support with N-doped graphene/nickel cobaltite composite catalyst J. Electrochem. Soc., 166 (4), F1-F8, 2019.

   Patent

7. **S Lal**, M Deepa, V M Janardhanan, K C Sahu, Direct paper based fuel cells for micro-nano systems3515/CHE/2015 (filed)

List of conferences

1. 232nd **S Lal**, V M Janardhanan, M Deepa, K C Sahu, Experimental and modeling studies of paper based methanol, Electrochemical Society (ECS) meeting, 2017, Maryland, VA, USA (oral presentation).

2. **S Lal**, M Deepa, V M Janardhanan, K C Sahu, Paper based hydrazine fuel cells with Au and Cu catalysts, National symposium on Electrochemical science and technology (NSEST), 2016, Electrochemical Society India, IISC Bangalore.

Contents

Chapter 1

Introduction

Globalization and technological advances have revolutionazied the market of portable electronics, such as laptops, cellular phones, micro-sensors etc, since the last few decades. This has undoubtedly eased out our day-to-day life, but simultaneuosly, increasd the energy demands on the global scale. The power requirement for different devices is quite diverse as, shown in Fig.1.1, and it varies from 1 MW for powering airplanes to as low as 1 μW for powering micro-nano systems/devices (MNS). Recently, MNS have gained a lot of attention worldwide because of their wide range of applications in healthcare, environmental monitoring, micro/nano-electromechanical systems (MEMS), wireless electronics etc [1, 2]. These devices (MNS) require power in micro and nano watt ranges for a short duration. For healthcare applications, lateral flow devices such as glucometers, dengue-detection kits, pregnancy detection kits are being used extensively as point-of-care devices, for rapid diagnosis and qualitative/quantitative analysis. These devices are usually disposed after one-time use [3, 4]. The integration of these devices with suitable energy sources has been the subject of interest for researchers, recently. In this context, energy storage and energy conversion devices which harvest energy from the renewable resources are best suited for powering MNSs. Below is the list of various energy storage units which can be used for powering MNS.

- Li-ion batteries

- Zn-air batteries

- Fuel cells/microbial fuel cells

- Enzymatic cells

- Quantum dot solar cells

- Dye-sensitized solar cells

1

Although these have been used successfully in powering various devices, a few of them have certain drawbacks associated with them. For instance, energy storage in solar cells is expensive and their efficeincy is limited to availability of sun light. Bio-fuel cells such as microbial and enzymatic fuel cells usually operate in controlled environment and deliver power in mirco (µ) watt range [5, 6], and therefore, their application is limited to a very few low power requiring devices. Moreover, the specimen (bacteria/micro-organism) required for the operation of bio-fuel cells are very sensitive to the environment and their handling and preservation is little inflexible. On the other hand the, the power density obtained in batteries is quite high, but it is not continuous and their shelf-life is subject to the amount of reactants stored in it, and once they are consumed the batteries are either disposed or need to be recharged. Most of the point-of-care devices function on button cells or batteries and after single use, the whole device is discarded along with the batteries. This is not economically viable and the disposal of batteries is an environmental concern, because they usually come with metal packaging and casing, which is not bio-degradeable.
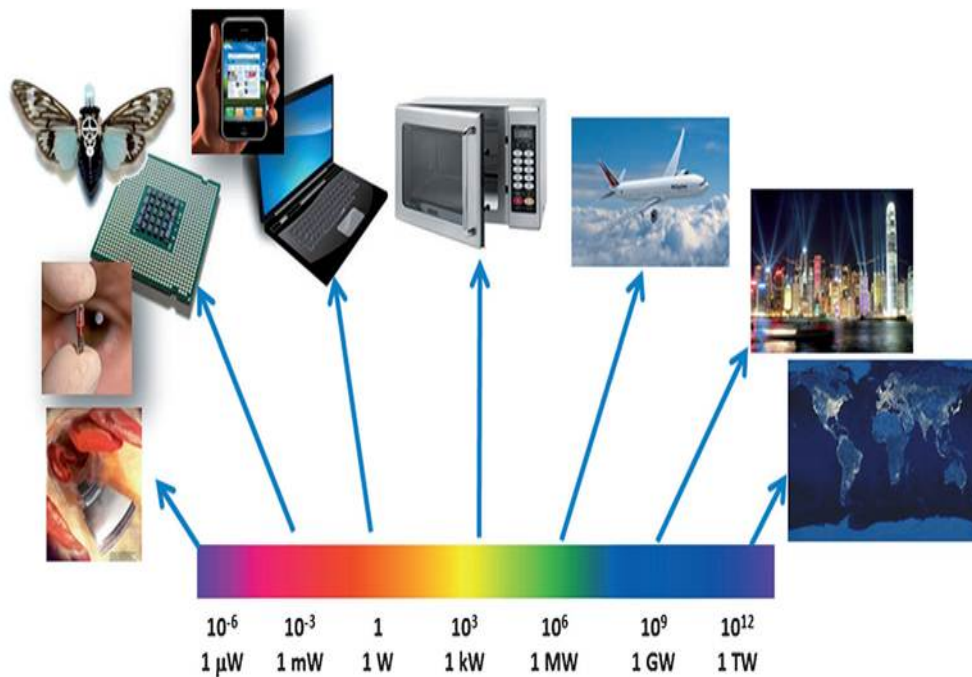
Figure 1.1: Power requirement for different devices

Keeping in view of the aforementioned challenges in finding suitable powering sources for such devices, laminar flow and paper based microfluidic fuel cells have emerged as promising candidates. These fuel cells are different from the conventional bulky fuel cells, for they are miniaturized in scale and size, and require only small quantity of fuel to operate. The working principle of paper based fuel cells will be discussed in detail in the

following section.

1.1 Introduction to fuel cells

1.1.1 History and working of fuel cells

The first fuel cell was developed in 1839 by Sir William Groves, while reversing the electrolysis of water by an electrolytic cell using gaseous hydroden and oxygen. It was only during 1960s when fuel cells started gaining lot of attention worldwide by researchers, but couldn't be used for practical applications because of their high cost of installation, until around 1960-66, when fuel cells were first used by NASA as an energy providing source in space shuttles [7, 8]. The development of solid oxide fuel cell (SOFC) technology began in 1937-39, while direct methanol fuel cell (DMFC) were developed nearly half a century later in 1992, by Jet Propulsion laboratory. Post this, lot of research had begun towards the technological improvements of different types of fuel cells, to reduce its cost and make it more robust for practical applications. However, the actual commercialization began in the early 2000 [9].

A fuel cell is an electrochemical device which converts chemical energy to electrical energy as long as there is a continuous supply of fuel and oxidant. A fuel cell has three main parts, namely- anode, cathode and electrolyte. The fuel is fed to the anode where it undergoes electrochemical oxidation and releases electrons. These electrons reach the cathode where the oxidant is electrochemically reduced. The electrons formed at the anode are responsible for generating the electrical energy in the fuel cell. The electrolyte present between the anode and cathode is responsible for the transfer of charged species and inhibits the flow of electrons through it, thus preventing the short-circuit of electrodes. Some electrolytes conduct only anions, whereas others conduct only cations and different fuel cells use different types of electrolyte membranes depending upon the type of charged species that complete the electrical circuit. For example, a polymer electrolyte membrane fuel cell (PEMFC) uses a proton conducting/exchange membrane, whereas a solid oxide fuel cell (SOFC) uses YSZ electrolyte which conducts only oxygen ions. The typical cell reactions are given by

$$H_2 \leftrightarrow 2H^+ + 2e^- \tag{1.1}$$

$$1/2O_2 + 2H^+ + 2e^- \leftrightarrow H_2O \tag{1.2}$$

Equations 1.1 and 1.2 describe the anode and cathode reactions, respectively. Here the H^+ liberated at the anode migrate to the cathode through the acidic electrolyte/membrane sandwiched between the electrodes [9], and completes the reduction reaction. Figure 1.2

represents the working of a such fuel cell.
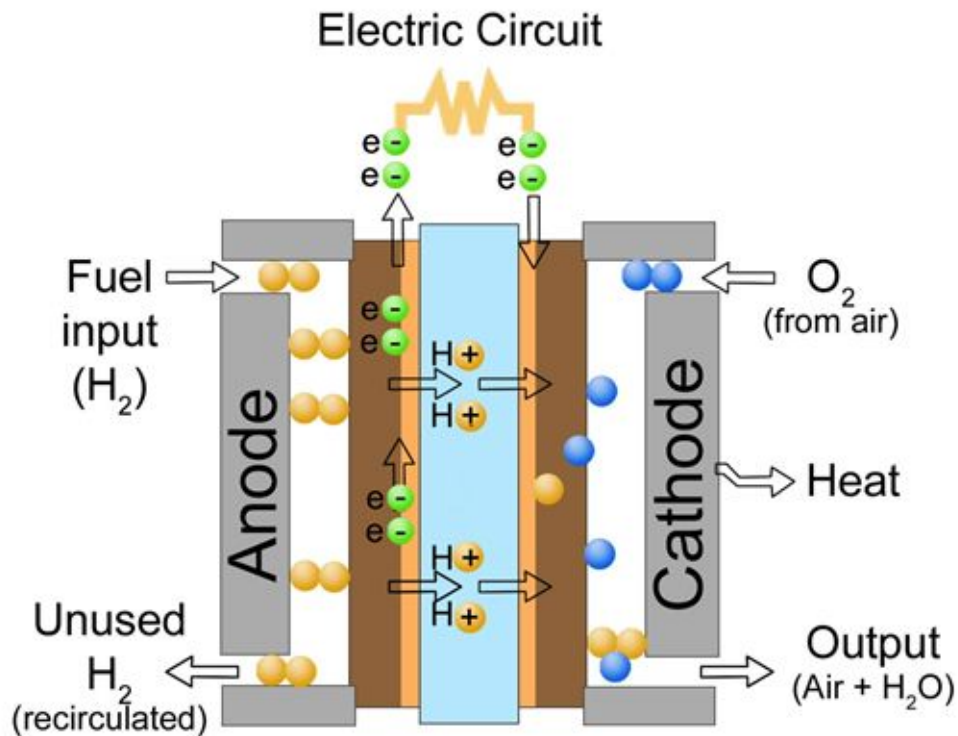
Figure 1.2: Working of a proton conducting fuel cell

1.1.2 Types of fuel cells

Fuel cells can be categorized based on the type of fuel, electrolyte and operating temperature. Each type has its own characteristics and produces output in different power ranges with different efficiency. The different types of fuel cells are listed below

- Polymer electrolyte membrane fuel cell (PEMFC)

- Direct methanol fuel cell (DMFC)

- Molten carbonate fuel cell (MCFC)

- Solid oxide fuel cell (SOFC)

- Phosphoric acid fuel cell (PAFC)

- Alkaline fuel cell (AFC)

- Bio-fuel cell (BFC)

A brief description and comparison of the above mentioned fuel cells is given in Table. 1.1

Table 1.1: Comparison of different types of fuel cells

Fuel cell	P, mW cm^{-2}	T_{opt}, °C	Catalyst	Mobile ion	Electrolyte	Fuel	Oxidant	Reference
PEMFC	100-1500	60-180	Pt-C, Pt-Ru	H$^+$	Nafion	H$_2$	O$_2$	[9, 10, 11]
DMFC	35-120	30-110	Pt-C, Pt-Ru Pt-Ni, Pt-Pd	H$^+$	Nafion	Methanol	O$_2$	[9, 12, 13] [14, 15]
MCFC	120- 150	600-700	NiCr, NiO	CO$_3^{2-}$	Liquid alkali, carbonate , (Li$_2$CO$_3$), Na$_2$CO$_3$, K$_2$CO$_3$) in Lithium aluminate (LiAlO$_2$)	Methane/H$_2$	O$_2$	[9, 16, 17]
SOFC	150-2000	600-1000	Ni-YSZ, Sr-doped LaMnO$_3$	O^{2-}	solid yttria-stabilized zirconia YSZ	Methane	O$_2$	[9, 18, 19]
PAFC	> 180	160-220	Pt-C	H$^+$	H$_3$PO$_4$	H$_2$	O$_2$	[9, 19]
AFC	60-200	50-200	Ni, Ag	OH$^-$	KOH	H$_2$, N$_2$H$_4$	O$_2$	[9, 19, 20]
BFC	0.004-2	20-60	Bio-catalyst Pt/C	H$^+$	Nafion	Organic matter Glucose	O$_2$	[9, 21]

P - **Power density**

T$_{opt}$ - **Operating temperature**

Paper based fuel cells- Recently, a new technology based on paper microfluidics has emerged, which uses paper as the substrate and medium of flow. These devices does self-transporting of fuel and devoid of any moving/metering parts and generally use liquid fuel with a liquid/gaseous oxidant. They can generate power densities upto several milli-watts. Paper based fuel cells are discussed in detail in section 4.2.3.

1.1.3 Potential losses in a fuel cell

The performance of each type of fuel cell is limited because of certain irreversible losses occurring in the system, which could be due to various reasons. Figure 1.3 depicts the different types of losses in a fuel cell. The different losses are classified as-
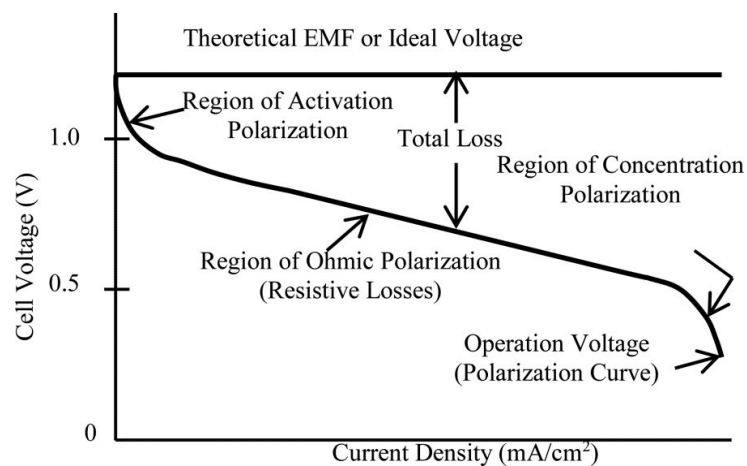
Figure 1.3: Representation of losses in a fuel cell

- **Activation losses** - When reaction kinetics are slow/sluggish at the anode/cathode or at both the electrodes, a part of the cell voltage is lost in overcoming the activation energy barrier inorder to start the reaction. This loss in voltage is referred as the activation loss and this usually occurs at at low current densities (1-100 mA/cm^2). This also known as the activation overpotential and accounts for the major losses in the fuel cell systems. The magnitude of activation loss depends on the exchange current density. A low exchange current density typically leads to high activation losses.

- **Ohmic losses** - The cell voltage drop can occur due to the resistance in flow of electrons at the conducting parts of the cell and the resistance to the flow of ions through the electrolyte/membrane. Such as losses are attributed to ohmic overpotentials/losses

6

and is given by

$$\eta_{ohm} = i(R_{\text{elec}} + R_{\text{ionic}}) \quad (1.3)$$

Since the electronic conductivity is several order of magnitude higher than the ionic conductivity, the electrical resistance is typically ignored in fuel cell analysis.

- **Mass transfer/concentration losses** - These losses arise due to the very fast electrochemical reaction rates compared to the mass transfer rates and typically occurs at very high current densities. The situation leads to negligible concentration of electrochemically active species at the reaction interfaces and the resulting current density is called limiting current.

- **Leakage overpotentials** - This occurs due to the crossover of fuel or oxidant to the cathode or anode leading to unwanted side reactions, hence loss in the cell voltage [22, 23].

1.1.4 Applications of fuel cells

Fuel cells have been used for various practical applications for a quite a long time now, and span a wide range of applications. The performance of fuel cell and its potential to be used as an energy source in a given application depends on its efficiency, start-up time and dynamic behaviour (changes in load can lead to changes in the temperature changes in the stack material of the FC). Moreover, its feasibility to be used for an application also depends on the fuel availability and energy density. For example hydrogen has a high energy density, but its transportation, handling and storage is a major setback. To counter this, liquid fuels such as methanol has been used widely in direct methanol FC, but at the cost of low energy density as compared to hydrogen. Based on the market requirement, fuel cells can be used for (a) portable and (b) stationary applications.

(a) Portable applications

The electronics market is flooded with a plethora of different portable devices, such as mobile phones, cordless phones, camera, notebooks, laptops. These devices require power in the range of 5 W-75 W. Currently, Li-ion batteries are being employed for powering computers, mobile phones, laptops etc, because of their relative low cost, compactness and easy operation. Given the fact, that the market size for portable electronics is large and the existing potential lithium scarcity [24], we have limited options available for power providing units, potential alternatives for these are the need of the hour. Till now, FC have not been able to replace Li-ion batteries on a commercial scale, but recently FC driven by H_2 catridges have been used in external chargers for mobile phones, laptops etc [25]. Recently, portable FC, such as PEMFC have seen a growing demand in the military applications because of their high efficiency, energy density and silent operation. In the year

2013-2014, the shipment of portable FC increased with an annual sales of 10000. Horizon have successfully launched fuel cell handheld USB chargers, in 2011[26]. The next step towards the deep penetrating application of fuel cells in portable electronics and MNSs is the miniaturization. In this regard various technologies based on micro-electro-mechanical systems (MEMS) and paper microfluidics, are being explored to develop fuel cell designs which are simpler and cheaper.

(b) Stationary applications

In addition to providing power for portable devices, fuel cells have received significant attention for stationary applications, due to their, high efficiency, and low-level emissions of undesirable products. They are used for a wide range of other applications such as, distributed power generation, auxiliary units as a power back system in residential units, where upto 5kW of power can be produced. Another advantage of using fuel cell in stationary applications is that can be used to produce both heat and electricity, with less ecological constraints[27]. Both high and low temperature fuel cells can be used for stationary applications, for providing power in locations where a grid cannot reach and also as an auxiliary or supporting power system in powering units which use capacitors, batteries, solar cells etc. High temperature fuel cells have an added advantage that they liberate heat upon their operation, which can be used in the other applications, low temperature fuel cells such as PEMFC benefit from the fast start-up time. Kohlstruck *et.al* have demonstrated the use of PEMFC in a cogeneration (combined heat and power-CHP) plant, which can lead to lesser emission of CO_2 and better fuel utilization [28].

1.2 Motivation and objective

As discussed in section 1.2.4 fuel cells can be used for a wide range of applications and they are constantly finding new markets as a result of significant research and development. A market segment, which is currently dominated by batteries and not resourceful is that of disposable diagnostic devices, which are used only once. There also other applications that involve MNSs such as environmental monitoring and communications technology. Use of fuel cells in these applications can disrupt the market if their cost and ease of operation can be made comparable to batteries. Since Li is in high demand due to increasing battery applications in automotive sector, their disposal after single use in point of care diagnostic devices cannot be justified. Furthermore, their disposal is environmental hazard if disposed without proper treatment methods.

| (a) Dengue detection kit | (b) Pregnancy detection kit | (c) Glucometer with paper test strip |

Figure 1.4: Paper based diagnostic devices.

However, in order to replace battery in these devices, a paradigm shift in the design and operation of fuel cells is required. The recent advent of paper based microfluidic devices is an attempt towards this. Paper can be successfully used to fabricate a fuel cell that can deliver power in the nano to micro watt to range. The inherent physical properties of paper such as capillary action and the porosity allows the unobstructed transport of liquids through the micro channels. This innate property of paper be exploited to achieve the transport of liquids in fuel cells without the use of any external metering devices. The absence of pumps for metering the fluids offer tremendous scope for miniaturization of paper supported fuel cells. Since paper can be cut into any shape and size the fabrication of these devices is very easy. Furthermore, paper is made of cellulose fibers and that makes the disposal of paper based cells environmental friendly. For example dengue, pregnancy and glucose detection kits, as shown in Fig 1.4 (a)-(c) which are based on paper, provide simple and rapid diagnosis and analysis of the disease, and their disposal after the use is easy. The main objective of the work is to fabricate and characterize fuel cells supported on pa-

per. The specific objectives are

i) Design paper supported fuel cells with different geometrical configuration to limit the fuel and oxidant cross over to the opposite electrodes.

ii) Identify different fuel oxidant pairs to form the anolyte and catholyte that can deliver high theoretical standard potentials.

iii) Characterize various electrodes and catalyst that can improve the cell performance for a given redox pair.

iv) Optimize the fuel concentration and catalyst loading to achieve the best performance.

v) Characterize the performance of the cell with and without ion conducting membrane and study the performance stability.

vi) Demonstrate the potential of the paper supported cell for practical applications by lighting a 3 mm LED with a few drops and anolyte and catholyte.

Chapter 2

Literature review

2.1 Laminar flow fuel cells, LFFC

The characteristics of flow and working of a paper based fuel cell is similar to that of laminar flow fuel cells. Laminar flow fuel cells generally do not use a physical membrane to achieve the separation of electrodes and the transport of ionic species that are responsible for charge transfer. In order to achieve the ionic transport between the electrodes, the fuel and the oxidants are mixed with appropriate electrolytes to form the anolyte and the catholyte. The anolyte and the catholyte are then passed parallely through micro channels. The electrodes are deposited at the walls of the channel. Since the flow of the anolyte and catholyte over the electrodes through the channel is laminar, their mixing is confined to the liquid-liquid interface, which acts as the virtual membrane. The laminar flow prevents the convective mixing of the anolyte and catholyte.

The flow principles are very much similar in a paper based fuel cell. However, the anisotropic orientation of cellulose fibers in paper leads to random pore networks. The transport of liquids in a paper is achieved by the capillary effect of the pore networks and the absorption capacity of the cellulose fibers. The random nature of pore network leads to non uniform capillary effects and leads to eventual mixing and cross over of anolyte and catholyte. On the other hand, the depletion region is created at the electrodes, due to the consumption of the reactants. [30], as depicted in Fig 2.1 and Fig 2.2.

Based on the concepts of laminar flow, various microfluidic cells (MFC) with different fuel-oxidant pair and noticeable performances, have been reported in the literature. These MFC can be with or without a physical membrane to achive the separation of electrodes. Cation and anion exchange membranes (AEM) are used for separating anode and cathode [31]. There are several advantages of using these membranes, such as limited fuel cross-over and better ion-transportation within the use of a membrane brings complexity in the fabrication of the cell and also adds a substantial cost to it. To further simplify the design
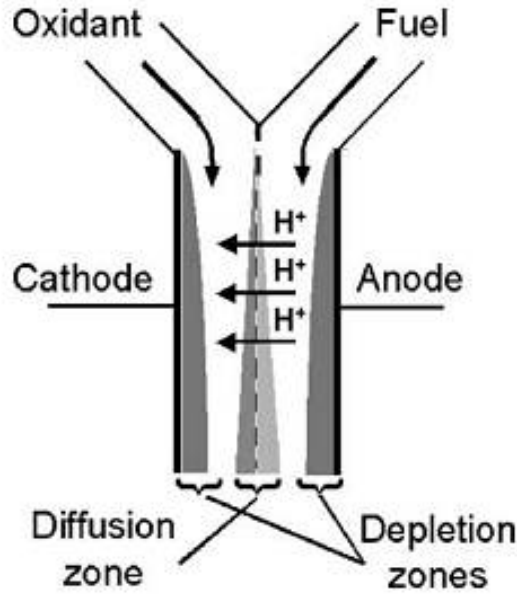
Figure 2.1: Schematic depicting laminar flow and mixing and depletion regions in an LFFC [29].
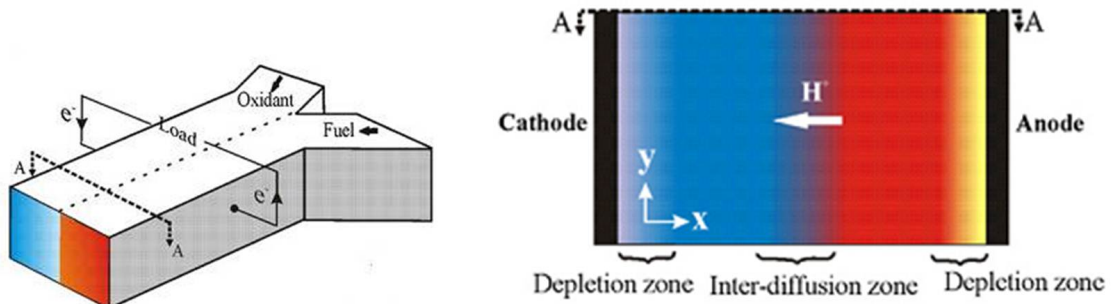
Figure 2.2: Pictorial representation of different regions formed in a Y-shaped LFFC [30].

and fabrication, membraneless microfluidic fuel cells (MMFC) have emerged as promising candidates to meet the power requirements at low cost with minimal complexity.

In the recent years, various architectures of MMFC have been reported, which can deliver power densities of ≈ 30 mW cm^{-2}. These fuel cells have micro-channels etched on a polymer-based substrate such as PDMS (polydimethylsiloxane) and PMMA (polymethyl-methacrylate). The catalyst layer/ink is deposited on these micro-channels which serve as the electrodes. The etching of the microchannels onto the substrate is done by various techniques such as, soft lithography, photography etc. The solutions of fuel and oxidant are pumped into the channels using syringe pumps. The pioneering works on MMFCs are by Ferrigno and co-workers. They have demonstrated the working of a redox fuel cell using vanadium redox couple, V(V)/V(IV) and V(III)/V(II), as the reducing and oxidizing streams, respectively. Although a stack of three cells delivered a power density of 192 mW

cm^{-2}, the low fuel utilization is one of the drawbacks of the cell [32]. The limitations of low fuel utilization and fuel/oxidant cross-over through the mixing region, can be overcome by changing the geometry of the cell.
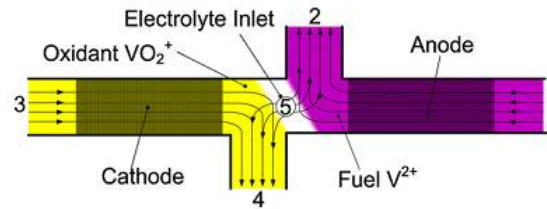
(a) Counter flow MMFC using vanadium as fuel and oxidant [33].
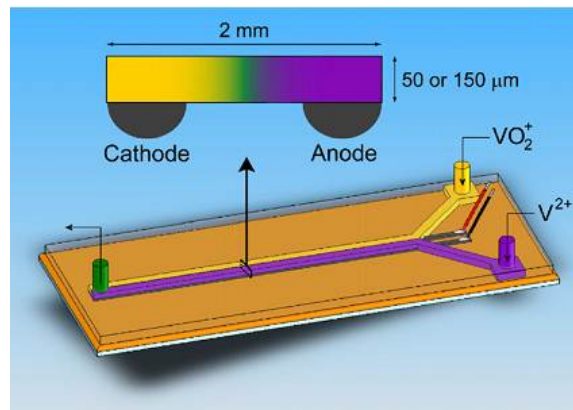
(b) Y-shaped MMFC with vanadium redox couple as fuel and oxidant [34].
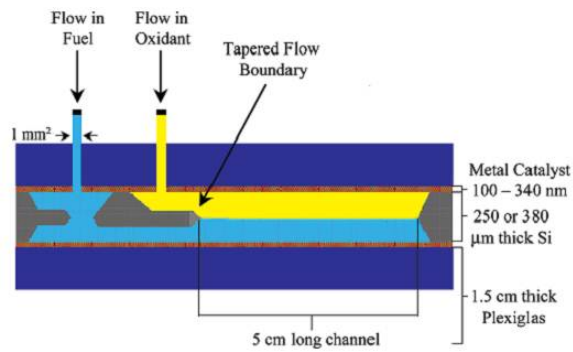
(c) An MMFC depicting planar flow of reactants [35].
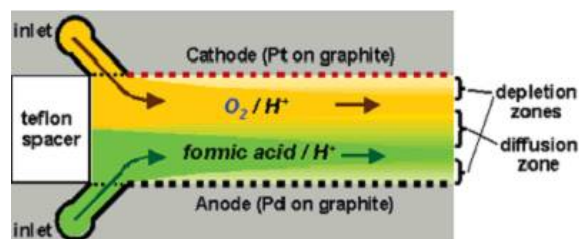
(d) An air-breathing MMFC with HCOOH-air fuel-oxidant pair [36].

Figure 2.3: Schematic of different microfluidic fuel cells reported in literature.

An H-shaped MMFC, can successfully eliminate these setbacks. Park *et. al*, fabricated an H-shaped cell, comprising of a small passage between the anode and cathode. They compared its performance with a rectangular cell which has co-laminar flow of reactants in the respective microchannels. The H-shaped cell delivered a power density of 13 mW cm^{-2} as compared to the latter (7 mW cm-2). The width of the mixing region in the H-shaped cell was also lesser, due to the passage [37].

The scalability of MMFC is another limiting factor in its operation as a powering source for portable devices. Wang and co-workers have reported the stacking of four T-shaped micro fuel cells with a scaling-out strategy. Formic acid (HCOOH) has been used as a fuel with hydrogen peroxide (H_2O_2) as the oxidant. The characterization of the cell has been done by both experimentally and mathematical modeling. The parallel stack of these cells delivered a maximum power of 265 μW [38]. Choban and co-workers have reported a Y-shaped micro-fuel cell, with multi-stream laminar flow of fuel and oxidant at a micro-scale, operating at room temperature. HCOOH/KMnO$_4$ and O$_2$ were used as the fuel and oxidant, respectively. Although the reported cell performance is low, the novel design can be useful in the fabrication of miniaturized fuel cells. The cell performance can be improved by employing bimetallic catalysts, which have better catalytic activity towards HCOOH [29].

Various other cell architectures, such as, counter flow MMFC [33] and 3D microfuel cell based on graphite electrodes [34], have also been reported. The schematic of different configurations of MMFC are shown in Fig 2.3.

The performance of microfluidic is dependent on the properties of the fuel, oxidant and also largely depends on the nature of the micro channels and the wettability of the fuel and oxidant for the particular material in question. Since in a membraneless fuel cell, the interphase between the anolyte and the catholyte acts as the membrane, the transport of ions occurs through this virtual membrane. This implicates that this 'virtual membrane' plays a vital role in the cell performance. The aqueous solutions of most of the fuels that are employed in a microfluidic fuel cell are not strong electrolytes, such as, CH_3OH, C_2OH, H_2O_2 etc.

In order to achieve better conductivity, these need to be mixed together with strong electrolytes such as H_2SO_4, H_3PO_4, NaOH, KOH, HCl, HClO$_4$ etc. to form the anolyte. The same holds true for oxidants as well, and suitable electrolytes are mixed with them to form catholytes. The choice of the electrolyte also depends on the oxidation/reduction potential that the fuel/oxidant pair can attain in the given medium. For instance, KMnO$_4$ has a reduction potential of 1.51 V in an acidic medium, whereas, in an aqueous medium it is 0.6 V. Therefore, it is desirable to opt for an acidic solution of KMnO$_4$, in order to attain higher OCV of the cell. This means that the same species can have different reduction/oxidation potentials in different medium. Thus, the choice of the electrolyte for the fuel and oxidant

should be based on the maximum theoretical OCV delivered by the anolyte-catholyte pair, dispersed in their suitable electrolyte.

For example, in H_2/O_2 membraneless fuel cell, the system delivered a maximum OCV of 1.4 V with dual (acid-alkaline) electrolyte, as compared to single (acid/alkaline) electrolyte system, where the OCV obtained is between 0.85-0.9 V. The fuel (H_2) is mixed with KOH and the oxidant (O_2) is mixed with H_2SO_4 [35]. In another investigation, a CH_3OH-air based MMFC delivered the maximum power density in a mixed media system, where the anolyte is acidic and catholyte is alkaline [39]. Apart from conventional fuels such as H_2 and CH_3OH, other fuels such as sodium perboarate ($Na_2BO_3.4H_2O$) have also shown better cell performances in dual/bipolar electrolytes systems, as compared to only acidic and only alkaline systems. $Na_2BO_3.4H_2O$ can be be used both as fuel and oxidant by mixing/dispersing it in suitable electrolytes. A fuel cell which uses $Na_2BO_3.4H_2O$ as fuel and oxidant delivered an MPD of 34 mW cm^{-2} at room temperature, in a bipolar electrolyte system. NaOH and H_2SO_4 have been used as the electrolytes for the fuel and oxidant, respectively. Although the OCV obtained experimentally were well below the thermodyanimc value, this MFC is free of any membrane and by-products, such as, CO_2. The only factor that limits/controls the cell performance is the concentration of the oxidant, and the cell performance can be improved by increasing the oxidant concentration [40].
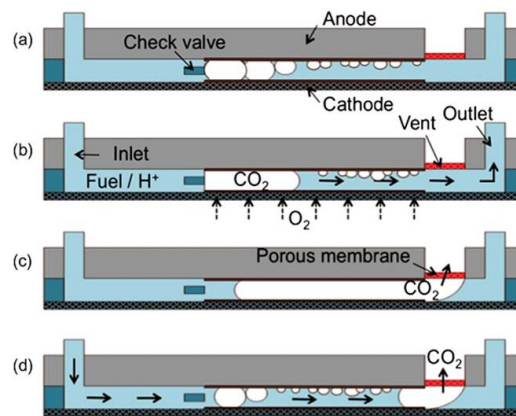
Figure 2.4: Schematic illustration of bubble pumping mechanism in a self-pumping $HCOOH-O_2$ membraneless fuel cell (a) Formation of CO_2 bubble (b) Growth and movement of CO_2 bubbles towards the membrane (c) Venting out of bubbles (d) Shrinkage of bubbles and fuel streaming into micro-channel [42].

Apart from experimental studies, Chen and co-workers have reported a theoretical study on MMFC. Here they have studied the flow in a micro-fuel cell consisting of planar micro-channel, comprising of HCOOH as the fuel and O_2 as the oxidant. This planar design provides better contact areas between the anolyte/catholyte and the electrodes, and the stacking of these micro-fuels is easier as compared to a Y-shaped MMFC. A thorough report of the various parameters effecting the cell performance has been presented [41]. These parameters included the flow rate, length of the micro-channel, thickness of catalyst layers etc. On the basis of this study they concluded that the cell performance was majorly limited by the low oxygen transportation rate, and can be overcome by increasing the flow rate and the catalyst layers' thickness [41].

It is worth mentioning here that, all the above reported MFC use a syringe pump to discharge the reactants into the channels. Several works on self-pumping MFC with and without membranes have also been demonstrated. For instance, the working and fabrication of a self-pumping MMFC with bubble pumping mechanism has been elaborately presented, as shown in Fig. 2.4. The flow of fuel (HCOOH) in the reactant channel is regulated by the movement of the CO_2 bubble formed at the electrode. The cell delivered a power density of 16.7 mW cm^{-2} [42]. Another self-pumping and self-breathing micro direct fuel cell has been reported by Sun and co-workers. This fuel cell utilizes the same mechanism for fuel pumping, as stated above. Methanol has been used as the fuel and the cell delivered an MPD of 7.4 mW cm^{-2} [43]. These findings lead us to the conclusion that by changing the geometry, the pumping mechanism, optimizing the geometry/design of the channels and employing different combinations of fuel/oxidant and electrolytes, one can optimize the fuel cell performance and attain the desired power densities.

2.2 Paper based fuel cells

As discussed above in section 2.1, the design and architecture of laminar flow cells effect the cell performance largely. Since the working of paper based fuel cells is also based on the principles of laminar flow of reagents, different configurations and designs of these fuel cells can lead to optimization of the cell performance. The development of these fuel cells is aimed at the miniaturization of energy devices for powering MNS, POC diagnostic devices and other portable consumer electronics, which require low power densities for their operation. This can be a novel approach towards finding suitable alternatives for batteries in certain applications. Although the performance of paper based energy devices (fuel cells/batteries) may not be as high as obtained in batteries and laminar flow microfluidic cells, their design and geometry can be optimized easily in order to achieve the desired performances. Recent studies have reported high power densities attained by paper based

fuel cells, which are comparable to the previously reported LFFC.

Esquivel and co-workers have recently developed a miniaturized paper based hydrogen fuel cell (Fig. 2.5(b)) with exceedingly better cell performance. This paper cell utilizes hydrogen gas as the fuel which is generated as a by-product of Mg oxidation. This device consists of two sections- a hydrogen generator compartment and a fuel cell compartment. The liquid or saline solution is discharged in the inlet which travels to the hydrogen generator and reacts with MgFe alloy upon its absorption in the NaCl pad. The H_2 which is generated as a result of this reaction travels to the fuel cell section that contains the electrodes and a KOH pad, which acts as the electrolyte and provides the medium for ion transportation. The maximum power density obtained was 103.2 mW cm^{-2}, which is the maximum reported for any paper based fuel cell reported so far. However, the cell performance depends upon the concentration of the Mg stored in the generator section, and the extent of the reaction. This fuel cell is compact in design and approach, and its perfromance is very much comparable to the conventional coin cells available in the market [44]. There are several reports, which investigated different designs for paper based fuel cells.

For example, a membraneless paper fuel cell, which uses hydrogen peroxide as the fuel and oxidant. The cell design comprising of a single-compartment power source, is achieved by microelectromechanical systems (MEMS) techhnology, as shown in Fig 2.5(a). Although the whole cell is supported onto a silicon (Si) wafer substrate, the medium of flow for the reagents is Whatman filter which is bonded onto the Si wafer. The carbon electrodes are screen printed onto the paper and the Ni and Al catalysts are spray coated on the electrodes. Since paper is the medium of flow, no pumps or ancillary metering devices are used to inject the fluids (fuel/oxidant). This miniaturized paper based fuel cell could deliver an MPD of 0.81 mW cm^{-2} [45]. Fig 2.5 depicts the different paper based fuel cell architecture reported in literature.

Another paper based fuel cell with fairly high power density using methanol as a fuel and ambient air as the oxidant has been reported (Fig. 2.5(c)) [3]. A prototype for the paper cell has been fabricated , wherein the fuel (methanol) and electrolyte (KOH) are stored in an agar-agar gel and an absorbent pad, respectively. The design consists of the electrodes, the methanol containing agar gel and KOH containing conjugate absorbent pad on a single strip of Whatman filter paper. The electrodes are separated by a slit, and the cell is activated upon discharge of H_2O, which leads into the formation of aqueous solutions of methanol and KOH. The cell delivered a peak power density of 4.4 mW cm^{-2}, with a maximum operational time of 7 minutes under a current load of 1mA. However, the use of Pt and Au at the electrodes, may limit its use as a cheap on-board energy source. Another microfluidic cell, which is fabricated with paper combined with polymeric laminate materials has also been reported [46]. The device is configured by laminating paper between pressure sensitive
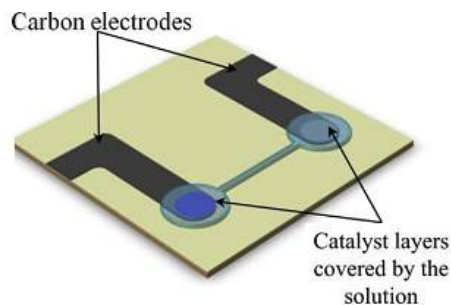
(a) Paper based H_2O_2 single-compartment fuel cell [45].
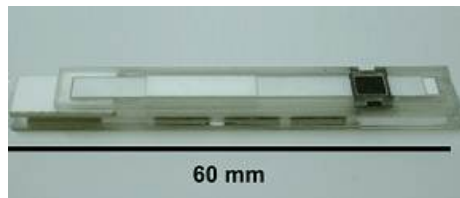
(b) A paper based hydrogen fuel cell [44].
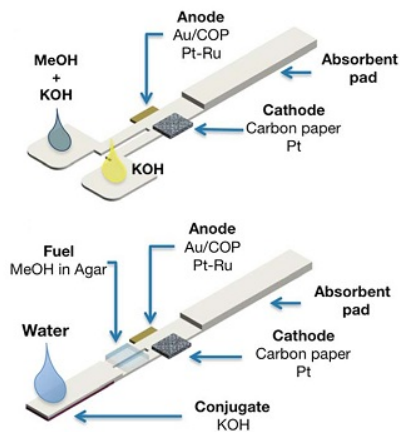
(c) Paper based microfluidic methanol fuel cells [3].
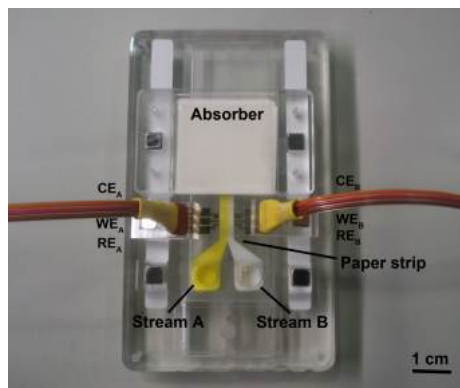
(d) A paper based microfluidic fuel cell [46].
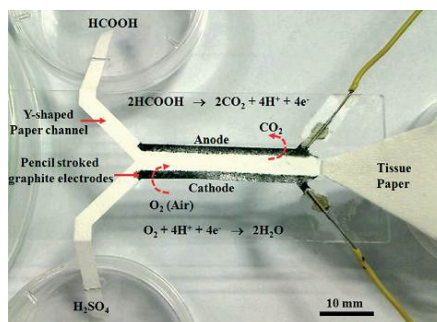
(e) Self-pumping and air-breathing paper based fuel with pencil stroked electrodes [47].

Figure 2.5: Different paper based fuel cell architectures reported in literature.

(a) A paper based formic acid fuel cell with no catalysts   (b) A T-shaped paper based cell with PAM gel acting as the proton exchange membrane.
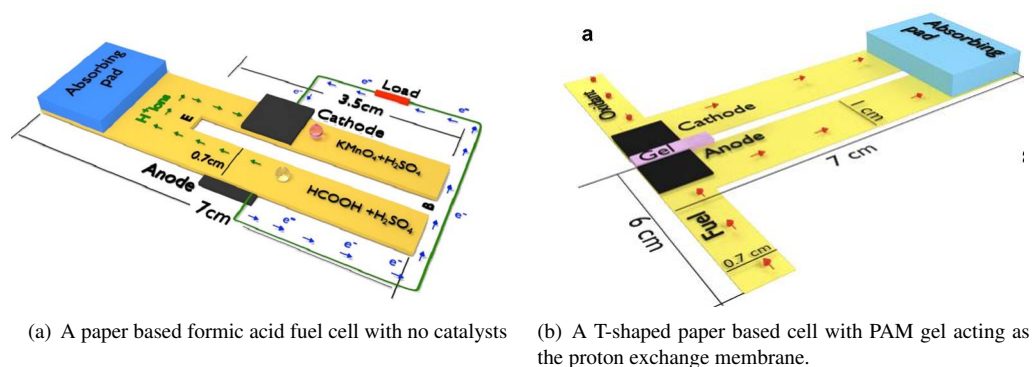
Figure 2.6: Schematic of membraneless and with membrane paper based fuel cell

adhesives. Au-COP spray coated by Pt-Ru and Pt catalysts are used as anode and cathode, respectively. A photograph of the device is shown in Fig. 2.5(d). Methanol, KOH and O_2 serve as the fuel, electrolyte and oxidant. The cell could deliver an OCV on 0.52 V with 200 μl of fuel and a power density of 1.05 mW cm^{-2}.

In addition to methanol, other fuels such as formic acid and hydrazine monohydrate have also been used in paper based membraneless fuel cells. One such membraneless cell architecture has been reported by Lal and co-workers. Here, the cell design consists of a single paper strip with a slit in between, resulting in two parallel strips which merge at the mid of the paper strip, as shown in Fig 2.6(a). Graphite sheets were used as electrodes and no catalyst was employed. The cell uses formic acid as the fuel and $KMnO_4$ as the oxidant, and delivered a peak power density of 0.57 mW cm^{-2}. An interesting feature of this paper cell is that, it does not use any expensive reagents catalyst. Since the cell could deliver sufficient power density for powering short-time use diagnostic devices, with minimal input of non-toxic reagents and no catalysts, this can be a cost-effective and eco-friendly powering source [4].

Another alternative to graphite sheet based electrodes would be to directly rub/deposit graphite powder onto the paper, which can serve as electrodes. This can reduce the cost and complexity of paper cell fabrication. One such paper based fuel cell, with Hb-pencil stroked electrodes onto the paper, has been reported by Arun and co-workers [47]. Here formic acid-H_2SO_4-O_2, fuel-electrolyte-oxidant system, has been employed to yield high power densities and stable performance from the paper cell. The electrodes were created by stroking an Hb-pencil onto the filter paper. They have studied the effect of number of pencil strikes (k) on the cell voltage, wherein the potential increased upto 0.33 V with increase in k upto 200, and thereafter, the voltage dropped . Also, this paper cell attained a reportedly high power density of 32 mW cm^{-2}, with an operational time of 1000 minutes with 1mL of fuel and oxidant. The cell performance for this paper cell is exceedingly superior as compared to the other paper cells reported. However, these authors have not reported the

electrochemically active area that had been used to calculate the current density. The performance reported by the authors without the use of any catalyst is surprisingly high for a paper based HCOOH fuel cell as the performance is comparable to that of low temperature PEM fuel cells using HCOOH as fuel and Pt as catalyst [48].

In addition to this, various other designs for paper based fluidic batteries, origami based 3D paper batteries and bacetria-powered paper batteries [49, 50, 51] have also been reported, which can be incorporated in the fabrication of miniaturized paper based fuel cells. Other than paper cell architectures which are based on a single paper substrate, a plethora of microbial, enzymatic bio-fuel cells, have also been investigated by the researchers recently, and their working and operation has been studied elaborately, as shown in Fig 2.7.

(a) A stackable microbial fuel cell [52].

(b) A paper based microbial fuel cell under continuous operation [5].

(c) Paper based microbial fuel cell with paper impregnated with Na-PSS as the electrolyte [53].
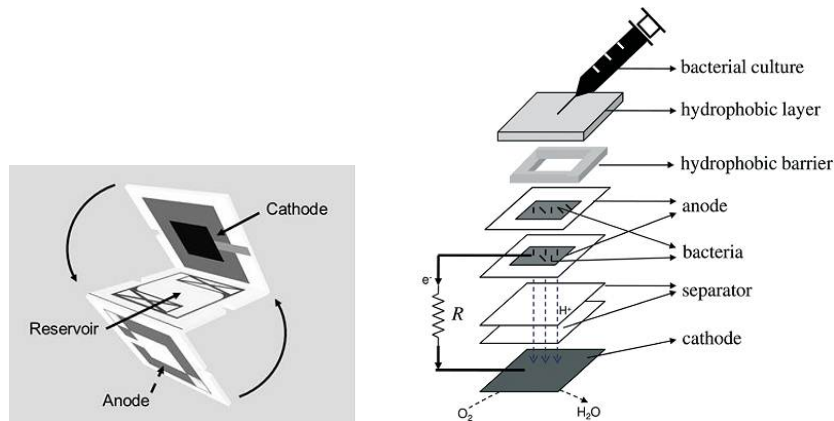
(d) 3D paper based enzymatic fuel cell [54].

(e) Schematic of paper based bacterial bio-fuel cell [55].

Figure 2.7: Different types of paper based microbial and enzymatic biofuel cells reported in literature

Biofuel cells are of two types-microbial fuel cell (MFC) and enzymatic fuel cell (EFC). Microbial fuel cell generates electricity by bio-degradation/oxidation of organic matter by bacteria. The power generated from these fuel cells is of small order (0.4 μW-1 mW cm^{-2}), but sufficient enough to provide power for sensors and low-power requiring diagnostic de-

vices [53]. On the other hand in an enzymatic bio-fuel cell, enzymes are employed as catalysts to assist the oxidation of organic/bio-degradable matter at the anode. In these fuel cells the power can obtained can be as low as 25 nW. Nevertheless, the enzymatic bio-fuel cells can be efficiently used for monitoring/sensing glucose levels in glucose sensing devices. Fischer and co-workers have successfully investigated the working of a 3D origami based enzymatic bio-fuel cell made out of paper substrate for glucose monitoring. The unique design consists of a 3D foldable paper cell where the anode enzymes are immobilized on the paper itself and the cathode is air-breathing [54]. Inspite of the multiple advantages associated with the environment- friendly EFC, few setbacks such as, temperature maintenance, half-life and purification cost of enzymes [55], may limit its commercial application. To this end, use of micro-organisms to catalyze the anode reactions can result comparatively longer shelf-lives of bio-fuel cells. Hashemi and co-workers have reported an MFC which works under continuous flow condition, for straight 5 days without any manual intervention (Fig. 2.7(b)). *Shewanella oneidensis MR-1* was used in the anolyte and potassium ferricyanide was used in the catholyte. The path for the flow of the liquid was created by printing hydrophobic wax on the paper. Carbon cloth was used as the electrodes. This paper based MFC yields a power density of 25 W m^{-3} [5].

In order to obtain high power densities and output voltage, stacking of fuel cells is required. Fraiwan and co-workers, have reported the working of a stack of four paper-based MFC, as shown in Fig. 2.7(a). Each cell in stack could yield an OCV of 0.4 V and the stacked series could generate a stable OCV of 1.6 V and MPD of 1.27 μW cm^{-2}, with a discharge of 50 μl each of anolyte and catholyte [52]. Recently, paper based multi-anode microbial fuel cells (PMMFC) have also been reported. These fuel cells find its applications in bio-sensors for assessing waste-water quality [56]. Although, the above mentioned MFC and EFC possess numerous advantages as they are eco-friendly, bio-degradable and easy to dispose, their miniaturization still remains as a challenge for their practical application in portable electronics. This is because the functioning and operation of bio-fuel cells, require strict and controlled environment maintenance for their species (bacteria) and enzymes. Also, at most care has to be taken to prevent the contamination of these species, as this may totally affect the performance and output of bio-fuel cells.

2.3 Role of electrolyte, fuel and oxidant in ameliorating the cell performance

As discussed in section 2.2, the design and geometry of paper based fuel cells play an integral role in improving the cell performance, similarly, the cell performance and cell voltage, depends largely on the fuel-oxidant (anolyte-catholyte) redox couple chosen.

The anolyte and catholyte pair chosen should posses high ionic conductivities for facile transport of the cations from the anode to the cathode or anions from the cathode to the anode. For instance, a laminar flow fuel cell with HCOOH as the fuel and H_2SO_4 saturated with O_2 as the oxidant was successfully demonstrated [57], where H_2SO_4 acted as the medium for the transport of H^+ ions. In another example of paper based fuel cell using CH_3OH as fuel, KOH was used as the electrolyte phase for the transport of OH^- ions, which were formed at the cathode [3].

The oxidation and reduction kinetics of fuel and oxidant is also influenced by the nature of the electrolyte. Thus, the resulting oxidation and reduction potential of particular species can vary by changing the type of the media/electrolyte. Lopez-Rico tested the cell performance of an ethanol-based air-breathing nanofluidic fuel cell in different media i.e., all acidic, all alkaline and mixed media (alkaline anolyte and acidic catholyte). Two different types of the electrocatalysts are used, i.e., commercial Pd/C ETEK and Pd/C IL syntesized by reduction method. It is observed that the cell performance changed by varying the pH of the electrolytes. The current density of a mixed media cell increased by a factor of three as compared to all-alkaline and all-acidic. The cell delivered a maximum power density of 100 mW cm^{-2}. The improvement in the cell performance can be attributed to the increase in cell voltage due to the variation of pH and its effect in the Nernst potential [58]. A similar trend in the cell performance was observed in a membraneless sodium borohydride based fuel cell with sodium perborate as the oxidizer. The cell performance was investigated in different electrolyte combinations, i.e., all acidic, all alkaline, mixed acidic-alkaline. The maximum power density of 27.75 mW cm^{-2} was obtained by dispersing sodium borohydride in alkaline medium (NaOH) and sodium perborate in acidic medium (H_2SO_4). This high yield of power density can attributed to the high OCV of 2.06 V obtained in the mixed electrolyte configuration, which allows the extraction of maximum energy from the fuel and oxidant in alkaline and acidic medium respectively [59].

Similar to direct borohydride fuel cell, direct hydrazine monohydrate fuel cell with hydrogen peroxide as the oxidant exhibited exceedingly better cell performance, by delivering a power density of 195.4 mW cm^{-2} at 80 °C. In this case too, the anolyte is alkaline, consisting of hydrazine monohydrate and NaOH, and the catholyte is acidic comprising of H_2O_2 and H_2SO_4. The charge carrier for this system was reported to be Na^+ [60]. In all of these examples the electrolyte phase facilitates the transport of ions to the respective electrodes. Thus higher conductivity of the resulting anolyte and catholyte will result in lower Ohmic resistances and improved cell performances.

Another desirable property of an anolyte-catholyte pair is that it should deliver a high theoretical standard potential at room temperature. In addition to this, the cell reactions involving these should not lead to the formation of hazardous by-products at ambient condi-

tions.The storage and handling of reagents of the species should not be stringent, and they should not self-decompose at room temperature. Since paper based cells operate at room temperature, only fuels that undergo electrochemical oxidation at room temperature can be used. Formic acid (HCOOH) and methanol (CH_3OH) have gained significant interest in the recent past as direct fuels for use in low temperature fuel cells [61, 62, 63, 64, 65, 66, 67] (e.g. Proton exchange membrane fuel cells (PEMFCs), which typically function in the range of 80° - 120°).

Nevertheless, these can also be used in fuel cells that operate at room temperature [64, 3, 68]. Therefore they have been the most commonly used liquid fuels for laminar flow membraneless fuel cells [69]. Pure formic acid has a volumetric energy density of 2.08 kWh l^{-1} [63] and that of methanol is 4.69 kWh l^{-1} [63], both of which are higher than that of liquid hydrogen and are good sources of hydrogen. Also methanol is cheap, easy to handle and store, available in plenty and can be renewed from wood alcohol [70]. Although the volumetric energy density is higher for CH_3OH, the theoretical open circuit potential of the $HCOOH/O_2$ system is 1.45 V, which is higher than that of the CH_3OH/O_2 system (1.2 V) [4]. Moreover, formic acid being a proton conductor, also serves as a strong electrolyte for the transport of protons [62]. In order to obtain better conductivity for methanol based systems, one can mix them in the suitable electrolyte, acid or alkali. In addition to methanol, ethanol is another alcohol that has been widely used as fuel in different types of fuel cells-acid and alkali. Ethanol has a high volumetric energy density (as compared to methanol and formic acid) of 6.28 kWh l^{-1}, and is considered as renewable fuel [73]. Although, ethanol is non-toxic, it has slow electrochemical oxidation rates and low reaction efficiency, due to difficulty in the C-C bond cleavage, thus reducing the cell performance [74]. However, the cell performance can be improved by employing suitable catalysts to enhance the oxidation kinetics.

Apart from these fuels such as CH_3OH, C_2H_5OH, HCOOH, H_2O_2, hydrazine monohydrate ($N_2H_4.H_2O$), is a promising candidate for application to laminar flow paper based fuel cells. The oxidation of hydrazine monohydrate leads to the formation N_2 and H_2O, both of which are harmLess to the environment. Moreover, hydrazine based fuel cells can operate at low temperatures and deliver high power densities [75, 60]. One downside of using hydrazine is that, it is hazardous when handled in pure form. Therefore, it is generally stored in aqueous solutions or in solid form as hydrazone. Although not for laminar flow based systems, the working of hydrazine-hydrogen peroxide fuel cells at low temperatures has also been demonstrated [75, 60].

Typically, Pt has been used as the electro-catalyst in these systems. Replacing expensive noble metals with other electro-catalysts has always received considerable attention. Similar to hydrazine monohydrate, ammonia borane too has a high hydrogen content of 19.6

wt% and high volumteric energy density of 5.4 kWh l^{-1}, and has been successfully imple-
mented as fuel in combination with O_2 and other oxidants in direct ammonia borane fuel
cells. Besides this, it also has expedient properties such as, non-toxicity, chemical stability
and high solubility in water. This implies that ammonia borane can be a potential alter-
native to other hydrogen containing fuels [76]. The volumetric energy densities of various
fuels is presented in Table 2.1 (may vary slightly to what has been reported in section 2.3).

Table 2.1: Volumetric energy density of different fuels reported in literature [77]

Type of fuel	Volumetric energy density (kWh l^{-1})
Methanol	4.82
Ethanol	6.28
Propanol	7.08
Ethylene Glycol	5.8
Glycerol	6.4
Formic acid	1.75
Dimethyl ether	5.61
Hydrazine	5.4
Ammonia borane	6.1

Other than fuel and electrolyte, oxidant/oxidizing agent also plays a vital role in deciding
the cell performance; for a strong oxidizing agent can lead to low activation losses. Ambi-
ent air or electrolytes sufficiently saturated with O_2 has been efficaciously implemented as
oxidant in different laminar flow microfluidic fuel cells [30, 67, 42] and paper based fuel
cells [47, 3, 44]. The microfluidic fuel cells with air-breathing cathode, that are based on
laminar flow have exhibited prolific cell performance. However, in case of a paper based
system the cell performance largely relies on the diffusion of the species (fuel/oxidant)
through the capillaries of the paper (as stated in section 2.1), unlike the conventional lam-
inar flow cells, where the reagents flow in a micro-channel. Also, oxygen bubble growth
at the cathode can lead to formation of two-phase system at the cathode and thus, deter the
cell performance [78]. Since, oxygen reduction reaction kinetics is slow, strong oxidizing
agents can be directly used as the oxidant in aqueous forms, or by mixing them with appro-
priate electrolytes. This can lead to better diffusion of the oxidant as paper can completely
absorb the liquid phase species and supply the required concentration to the electrodes.
Over and above this, a liquid phase oxidant with more positive reduction potential as com-
pared to O_2, can provide higher theoretical OCV and removes the cell design limitation
by providing customization of cell architecture, where the cathode need not necessarily be
air-breathing.
To this end a plethora of oxidizing agent such as $KMnO_4$, $K_2Cr_2O_7$, H_2O_2 and $Na_2CO_3.3H_2O_2$
have employed as oxidants in both laminar flow and paper-based fuel cells [4, 79, 80, 81,
37], in combination with different fuels. It is also important to disperse these in their suit-

able electrolyte to obtain the desired OCV and impart sufficient ionic conductivity for easy transportation of ions from cathode to anode. For comparison the standard reduction potentials versus SHE (standard hydrogen electrode) of different oxidants is provided in Table 2.2.

Table 2.2: Comparison of reduction potential of different oxidizing agents

Type of oxidizing agent	Reaction (in acidic medium)	n_e	E^o vs. SHE
$KMnO_4$	$MnO_4^- + 8H^+ + 5e^- \leftrightarrow Mn^{2+} + 4H_2O$	5	1.51 V
H_2O_2	$H_2O_2 + 2H^+ + 2e^- \leftrightarrow 2H_2O$	2	1.77 V
$K_2Cr_2O_7$	$Cr_2O_7^{2-} + 14H^+ + 6e^- \leftrightarrow 2Cr^{3+} + 7H_2O$	6	1.33 V
$Na_2CO_3.1.5H_2O_2$	$2Na_2CO_3.3H_2O_2 \rightarrow 2Na_2CO_3 + 3H_2O_2, H_2O_2 + 2H^+ + 2e^- \leftrightarrow 2H_2O$	2	1.76 V

2.3.1 Role of different metal catalysts for ameliorating fuel electro-oxidation rates and cell performance

A fuel with a higher hydrogen content is not the only condition for better cell performance and efficiency. The easiness of fuel oxidation is very important in achieving good cell performance. For example, ethanol has a slightly high hydrogen content of $\approx$ 13.2 wt% than methanol which has $\approx$ 12.5 wt% of hydrogen. However, as stated in section 2.3, the electrochemical oxidation of ethanol is slow and complex due to the difficulty in the cleavage of strong C-C bond, and therefore, it may result in inferior cell performance and efficiency, as compared to a methanol fuel cell. Hence, methanol is a preferable choice over ethanol in spite of its relatively less hydrogen content. However, the cell performance can be augmented by the use of electro-catalyst in fuel cells that use formic acid, methanol, ethanol, hydrazine hydrate, ammonia borane as the fuel.

The electro-oxidation of formic acid follows dual pathway, namely (1) direct dehydrogenation path and (2) dehydration path. The direct dehydrogenation of formic acid involves multiple electron transfer and the formation of formate ($HCOO^-$) as the intermediate which further leads to formation fo CO_2, whereas, in dehydration path CO is evolved as the intermediate which further leads to the evolution of CO_2, involving single electron transfer. The evolution of CO at the anode can lead to the poisoning of catalyst used (for example Pt) [74]. The reactions involving formation of CO as an intermediate with Pt are described below [48].

$$HCOOH + Pt^0 \rightarrow Pt - CO + H_2O \qquad (2.1)$$

$$Pt^0 + H_2O \rightarrow Pt - OH + H^+ + e^- \qquad (2.2)$$

$$Pt - CO + Pt - OH \rightarrow 2Pt^0 + CO_2 + H^+ + e^- \qquad (2.3)$$

25

The overall reaction is given by

$$HCOOH \rightarrow CO_2 + 2H^+ + 2e^- \qquad (2.4)$$
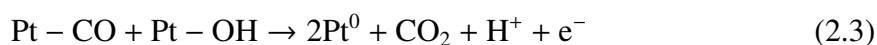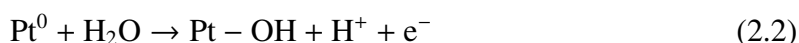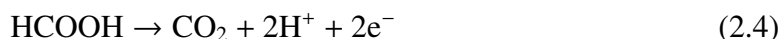
By and large, whichever pathway formic acid follows, the oxidation potential is -0.25 V. Generally Pt or Pd or Au have been used as catalysts in anode of direct formic acid fuel cells and the formation of CO is favored more in the presence of Pt, as described above. However,the use of expensive noble metals can not be justified for use in MNSs or in single use diagnostics devices that are disposed after use. Therefore, non-noble metal catalysts with desired catalytic activity for formic acid can be an alternative to these expensive metal catalysts. Other than this carbon supported Pt- and Pd-based catalysts have been an alluring substitute for stand-alone Pt-based catalysts. The presence of carbon imparts better electronic conductivity and more active surface area to the catalyst, hence better electro-oxidation rates. Also this can lead to better cell performance with lower metal loading and less catalyst deactivation due to poisoning [82].

The carbon supported and unsupported non-noble metal catalysts, such as, Cu, Ni, Co, Mo, have also been successfully used in enhancing the electro-oxidation rates of other fuels, such as, methanol, hydrazine hydrate, ammonia borane and ethanol. They have attracted significant attention from the researchers, because of their low cost, availability and have shown good electro-oxidation rates, comparable to that of Pt, Pd, Au, Rh etc. For instance, Cu has been successfully used in different forms and structures for electrochemical oxidation of hydrazine [83, 84, 85]. A Cu-based nanostructured anode [86], (Cu-Ni nanostructured catalyst), where a Cu-foam is electroplated using a Ni-salt [87] or Cu nanocubes grown on graphene paper [88], have shown high catalytic activity towards hydrazine oxidation, with long-term stability of the fuel cell. The electro-oxidation of hydrazine and suppression of its hydrolysis is favored more in an alkaline medium. The electro-oxidation of hydrazine in alkaline medium occurs according to the following reactions [89].

$$N_2H_4 + OH^- \rightarrow NH_3 + (1/2)N_2 + H_2O + e^- \qquad (2.5)$$

$$N_2H_4 + 2OH^- \rightarrow N_2 + H_2 + 2H_2O + 2e^- \qquad (2.6)$$

$$N_2H_4 + 4OH^- \rightarrow N_2 + 4H_2O + 4e^- \qquad (2.7)$$
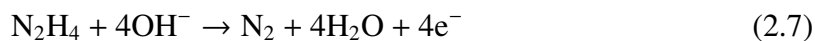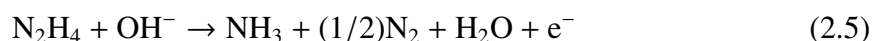
The standard reduction potential for this reaction is 1.61 V. When hydrazine is dissolved in water it undergoes hydrolysis and dissociates into $N_2H_5^+$ and OH^- ion. The hydrolysis of hydrazine can lead to its cross-over from anode to cathode (migration of $N_2H_5^+$ ion), and thus deter the cell performance [90]. Therefore, hydrazine is usually mixed with NaOH to form the anolyte, since the addition of OH^- ions can suppress the hydrolysis of

hydrazine and the cross-over of $N_2H_5^+$ ions [91, 75]. Recently,a surfeit of non-noble metal catalyst have been reported which have good electrocatalytic activity towards hydrazine. For instance, Asazawa and co-workers investigated different non-noble metal catalyst and compared their catalytic activity towards hydrazine oxidation with Pt. They found that the onset potentials of Co(-0.178 V) and Ni(-0.108 V) were lower than that of Pt (-0.062 V) [92]. This implicates the better functioning of Co and Ni in enhancing the oxidation kinetics. Along with stand alone metal based catalsyts, alloys of non-noble metals in nano-particles form have also been reported. An alloy of Ni-Fe plated on carbon has been found to have high catalytic activity towards hydrazine [93].

Since the catalyst support plays a major role in deciding the electro-catalytic activity of the metal, combining Cu nanostructures on carbon supports, such as functionalized multi-walled carbon nanotubes (f-MWCNTs), single walled carbon nanotubes (SWCNTs) and graphene can improve it's electro-catalytic activity. Stand-alone Cu nanoparticles (Cu-NPs) tend to agglomerate, but when dispersed on a support such as f-MWCNTs or graphene pa-per, this problem is overcome, which otherwise leads to a decrease in active surface area, and hence low activity. Apart from this, Cu-MWCNTs hybrid microstructures have also been fabricated by calcination and H_2 reduction method [94]. The aforementioned carbon nanostructures have been used as support materials for Pd, Ni, and Ag [95, 96]; however, not for application in laminar flow fuel cells operating at room temperature.

Similar to hydrazine, ammonia borane too exhibits good electrochemical activity in an al-kaline medium. The electro-oxidation of ammonia borane occurs as follows [76].

$$NH_3BH_3 + 6OH^- \rightarrow BO_2^- + NH_4^+ + 4H_2O + 6e^- \quad E^0 = -1.216V \quad (2.8)$$
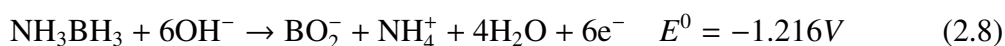
Various metal-based complexes with high activity towards hydrogen release and dehydr-genetion have been reported. Iridium pincer complex was found to be an active species for the generation of H_2 from ammonia borane [97]. Noble metals such as Pt and Au micro-electrodes have been employed as electro-catalysts in ammonia borane fuel cells and for effeccient electro-oxidation in alkaline medium [76, 98]. Other than these Co-Ni nanoparticles supported on rGO, unsupported monodispersed Ni nanoparticles, carbon supported Ni nanoparticles and Ag-based core shell nanoparticles supported on graphene, have also shown high activity towards H_2 generation and hydrolysis of ammonia borane [99, 100, 101, 102].

Methanol has reportedly slow electro-oxidation rates [103] (in acidic medium) and high cross-over as compared to ethanol [104]. The electro-oxidation of methanol in an aqueous medium, occurs at a low oxidation potential of $E^0 = 0.04V$, whereas, in an alkaline medium the oxidation potential of methanol is quite high, i.e., $E^0 = -0.81V$, as shown in equation

2.9.

$$CH_3OH + 6OH^- \rightarrow CO_2 + 5H_2O + 6e^- \quad E^0 = -0.81V \qquad (2.9)$$

This implicates that its oxidation is favorable in alkaline medium rather in aqueous or acidic medium. However, the environment of reaction (acidic/alkaline/aqueous), is not the only factor responsible for improving the kinetics, but catalysts with high activity, (such as Pt) are also required. To this end, Kakati and co-workers studied the effect of different nano-structural forms of Pt, such as, nano-wires, nano-rods, nano-cubes, nano-flowers, on the oxidation of methanol, in order to implement the direct methanol based fuel cells for commercial applications [70]. But in a paper based fuel cell, the use of Pt curbs down its implementation as a commercial on-board energy source, as these noble metals are expensive. Inexpensive non-noble metal catalysts based out of Co, Ni, Cu, bimetallic oxides and hydroxides of these have also been reported with fairly high catalytic activity. For instance, a cobalt hydroxide modified glassy carbon electrode has been reported by Jafarian and co-workers, wherein, they obtained large anodic current, indicating good catalytic activity of the electrode proposed [105].
Recent reports on high catalytic activity of bimetallic oxides such as, nickel cobaltite ($NiCo_2O_4$), in different morphologies, towards methanol, stimulates their use as a catalysts for paper based fuel cells. $NiCo_2O_4$ is mixed valence oxide with high electrical conductivity and the redox couples of Ni^{2+}/Ni^{3+} and Co^{2+}/Co^{3+} provide rich electro-active sites for electron transfer [106], thus providing better reaction rate. Moreover, composites of these, with layered carbon-based supports such as graphene oxide (GO) and reduced graphene oxide (rGO) have shown exceedingly better methanol electro-oxidation rates. For instance, a composite of rGO-$NiCo_2O_4$ nanoparticles with long term stability and excellent electrocatalytic activity towards methanol has been reported [107]. Further the catalytic properties of rGO and its composites can be enhanced by doping them with nitrogen, as it imparts more electron cloud density, electronic conductivity and more active surface [108]. This, can be helpful in attaining high power densities and cell performance in a methanol based fuel cell. Also, for the development of low cost paper based fuel cells, these can be potential replacements for Pt, Pd, Au, Ag and other noble metals, which may not serve the purpose of cost-effective fabrication and development of paper based methanol fuel cells.
Ethanol is known for its slow electrochemical oxidation kinetics. The standard reaction for electro-oxidation of ethanol is given by [104]

$$C_2H_5OH + 3H_2O \leftrightarrow 2CO_2 + 12H^+ + 12e^- \qquad (2.10)$$

However, the oxidation of ethanol is generally complex and occurs through dual pathways,i.e. (i) through complete oxidation of ethanol by C-C bond cleavage, resulting in

the formation of adsorbed CO and eventually to CO_2, with release of 12 e^- [109] and (ii) through partial oxidation of ethanol to CH_3CHO, CH_3COOH, CO_2, CO_{ads} (surface adsorbed CO) and CH_x species. The partial oxidation of ethanol in an acidic medium is a $2e^-$ process and generally begins with the formation of CH_3CHO and results in the formation of soluble by products such as CH_3COOH, reaction intermediates such as ethane-1,1 diol and CO_2 as one of the final products. CO_2 may further undergo reduction to form CO_{ads} and CH_x species [110]. It has been reported earlier by researchers that the onset of ethanol oxidation doesn't take place below 0.4 V [111] and therefore, the onset potential should be about $\approx$0.4 V (E_{onset}). Hence, based on the above findings, the oxidation of ethanol on the anode can be summarized by the following reactions

$$C_2H_5OH \xrightarrow{E_{onset}=0.4\ V} CH_3CHO + 2H^+ + 2e^- \tag{2.11}$$

CH_3CHO further leads to formation of CH_3COOH, CO_2 and surface adsorbed CO, according to the following steps.

$$CH_3COOH \rightarrow CO_2 \rightarrow CO_{ads} \rightarrow CH_x \tag{2.12}$$
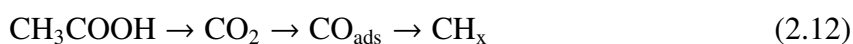
Various metal-based catalysts and binary metal catalysts such as Pt-Ru, Pt-Sn, trimetallic catalyts such as PtRuNi, PtSnNi and carbon supported metal catalysts such as Pt/C, Pd/MWCNTs, PdAg/MWCNTs (multiwalled carbon nanotubes), have been used as anode catalysts for ethanol electro-oxidation. These electrocatalysts have shown promising performance in direct ethanol based fuel cells (DEFC) and microfluidic fuel cells [112, 113, 114]. Molybdenum oxide (MoO_3) is a relatively cheaper alternative to the above mentioned noble metal catalysts, which are expensive and have limited availablility. MoO_3 has a good ethanol sensing property [115], and by preparing the same in nanostructured form, the catalytic surface area can be enhanced which can lead to high oxidation currents. While a composite of MoO_3 with poly(pyrrole) has been used as a support for PtPd nanoparticles for ethanol electroxidation in DEFC [116], but MoO_3 as a stand-alone catalyst in paper based ethanol fuel cell has not been reported, to date.

Chapter 3

Membraneless paper-based formic acid-permanganate fuel cell

3.1 Introduction

Formic acid has been extensively used as a fuel in various microfluidic and direct liquid-based fuel cells. Cai and co-workers have studied the performance of an air-breathing passive formic acid fuel, to understand the real contribution of formic acid in direct formic acid fuel cells (DFAFC). Nafion is used as the membrane, 40 wt% Pt/C and Pd/C are used as the anode/cathode catalysts. The cell performance is compared for different membrane electrode assemblies (MEA) prepared with hot pressed, non-pressed and decal method. The power density attained by the DFAFC with non-pressed MEA is 5.5 mW $^{-2}$. As compared to this, with hot pressed and decaled MEA, a higher power density of ≈ 8 mW cm^{-2} and 45 mW cm^{-2} is obtained, respectively. The increased cell performance in the latter cases can be attributed to the better contact between the PEM and the anode catalyst layers, which promotes the triple phase boundary building. Since formic acid acts both as the fuel and good proton conductor its enhanced contact within the MEA, facilitates the proton conduction at the anode/catalyst layer and the electrolyte (PEM). Based on this, the anode microstructure of the fuel cell is also designed and optimized, and fuel cells equipped with carbon cloth as anode delivered better performance than that of ones with carbon paper, as carbon cloth is more porous than carbon paper [117]. Thus, formic acid plays a key a role in deciding the cell performance, as well as the design and microstructure of the anode in the DFAFC.

Apart from the passive DFAFC, formic acid has been used as the fuel in membraneless microfluidic and laminar flow fuel cells as well, along with KMnO$_4$ or air as the oxidant and H$_2$SO$_4$ as the electrolyte. The cell performance is governed by the flow rates and concentrations of fuel, oxidant, electrolyte, cell geometry and catalysts. The catalyst is generally

present along the walls of the micro-channel within which the anolyte and catholyte flow. Cohen and co-workers reported a power density of 0.18 mW cm^{-2} [118]. The performance of such systems using air as the oxidant is limited to the diffusion of oxygen from air to the microchannels (of Si in the above case). To counter this, Jayashree and co-workers used a porous (Toray carbon paper) air-exposed gas-diffusion electrode as the cathode with Pt nanoparticles as the catalyst [36], which enables better diffusion of air and oxygen-reduction reaction kinetics and could attain a moderate value of 26 mW cm^{-2}. Thus, the range of power density attained by membraneless HCOOH-air systems reported by various researchers is quite variant. Other than oxygen, KMnO$_4$ is another choice for an oxidant in LFFC using formic acid as the fuel and power density in the range of 0.7-2.5 mW cm^{-2} have been reported [119, 29].

The above discussed LFFC are based out of Si, PMMA, PDMS etc., other than these formic acid has also been used fuel cells based on a paper scaffold. Arun and co-workers have fabricated a paper based formic acid fuel cell which could deliver a power density of 33 mW cm^{-2} without any catalysts [47].

As a first attempt towards achieving the objectives presented in section 1.3, a paper based fuel cell using formic acid as fuel and potassium permanganate as oxidant is developed and characterized. The cell uses graphite sheet as electrodes and does not use any metering device for the transport of fuel and oxidant. The cell presented in this chapter does not use a physical electrolyte membrane for the transport of ions form the anode to the cathode. Therefore, the fuel and the oxidants are mixed with H$_2$SO$_4$ to form the anolyte and the catholyte. The geometrical configuration of the cell is designed in such a way that it delays the cross over of anolyte and catholyte.

The half cell reactions occurring at the anode and cathode respectively are

$$\text{HCOOH} \rightleftharpoons 2\text{H}^+ + 2\text{e}^- + \text{CO}_2 \quad (E^0 = -0.25\ V), \quad \text{and} \tag{3.1}$$

$$\text{MnO}_4^- + 8\text{H}^+ + 5\text{e}^- \rightleftharpoons \text{Mn}^{2+} + 4\text{H}_2\text{O} \quad (E^0 = 1.51\ V). \tag{3.2}$$
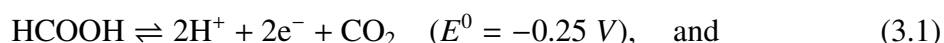
The overall reaction in the cell is given by

$$5\text{HCOOH} + 2\text{MnO}_4^- + 6\text{H}^+ \rightleftharpoons 2\text{Mn}^{2+} + 8\text{H}_2\text{O} + 5\text{CO}_2. \tag{3.3}$$
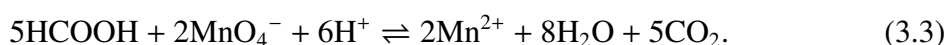
The concentration gradient of the protons and the voltage difference between the anode and cathode leads to the transport of protons from the anode to the cathode. Simultaneously, electrons move from the anode to the cathode via the external circuit. Two different mechanistic pathways have been proposed in the literature for the oxidation of formic acid. One pathway assumes a multiple electron transfer reaction and the other pathway assumes single electron transfer with the formation of CO as an intermediate product. The for-
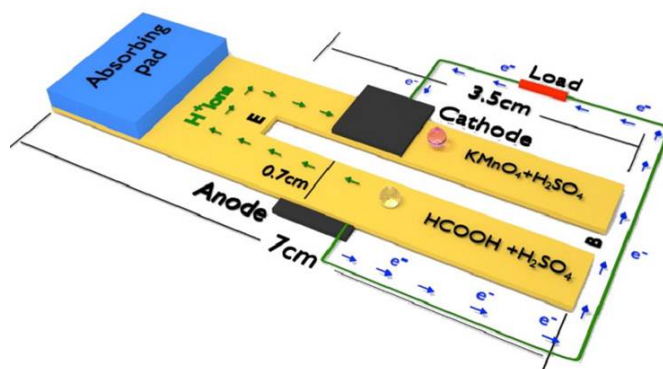
Figure 3.1: Schematic (not to scale) representation of the experimental cell configuration. **E** represents the end of the slit and **B** represents the beginning of the slit. The green arrows show the direction of transport of H^+ ions and blue arrows show the direction of electron transport.

mation of CO is favored when Pt is used as a catalyst. Irrespective of the pathway, the oxidation potential for HCOOH is -0.25 V. At the cathode, $KMnO_4$ dissociates to form K^+ and MnO_4^- ions. The MnO_4^- ions react with H^+ to form H_2O and the reduction potential for this reaction at the cathode is 1.51 V. The overall cell reaction gives an open circuit voltage (OCV) of 1.76 V.

3.2 Experimental procedure

A schematic representation of the experimental set up is shown in Fig. 3.1. A filter paper serves as the medium for the transport of anolyte and catholyte. The paper is cut into a 7 cm long strip having a width of $(1.4+d_s)$ cm, where d_s is the slit width, which is varied. At one extreme end of the strip, an absorbing pad made of tissue paper is attached to absorb the anolyte and catholyte. The graphite electrodes (13 mm × 5 mm × 1.3 mm) are placed on either side of the strip, and these two electrodes are separated by a thin slit. The slit prevents the direct mixing of anolyte and catholyte, although, mixing due to diffusion occurs at the end of the slit. This region is designated by the letter 'E' in Fig. 3.1. The contact area between the electrodes and filter paper is 0.35 cm^2. The graphite sheet at the anode faces down and the cathode faces open air. Since the cathode is porous and open to the atmosphere, it allows air to diffuse into the interface between the paper and graphite electrode. Although the anode faces downwards, a limited diffusion of air can occur at the anode as well. The whole set up is placed on a micro-slide glass plate. The anolyte is prepared by mixing formic acid with H_2SO_4 (4 M) and the catholyte is prepared by mixing potassium permanganate ($KMnO_4$, 1 M) with H_2SO_4 (4 M); all in ultra pure water. Formic acid (100%) and $KMnO_4$ (98.5%) are purchased from Merck and H_2SO_4 (90%) is purchased from Fischer Scientific. Different concentrations of formic acid have been used

(6 M-12 M). Additionally, the position of the electrodes from the end of the slit 'E' and width of the slit, d_s are also varied to determine the effect of electrode positioning and slit width on the performance of the system. Since graphite is a good inexpensive conductor of electrons, other current collectors are not used.

The self-transportation of anolyte and catholyte has been achieved by dipping the two tail ends of the strip (or beginning of the slit marked by 'B' in Fig. 3.1) into separate reservoirs of the anolyte and the catholyte. Since, the rate of flow strongly depends on the nature of the filter paper, two different filter papers (Whatman and Riveria) are used in this study, and both allow very slow transportation of fluids to the respective electrodes. In order to speed up the measurements, droplets of anolyte and catholyte are manually dropped near the electrodes. Droplets are never discharged directly on the electrodes as it may disturb the system. All dc polarization curves and electrochemical impedance spectra were acquired in an Autolab 302 N potentiostat/galvanostat with a frequency response analyzer, equipped with a NOVA 1.9 software.

3.3 Results and discussion

3.3.1 Effect of geometry on cell performance

The slit introduced in the strip between the graphite electrodes restricts the direct mixing of the fuel and the oxidant to a great extent. The variation of OCV with time for different concentrations of formic acid in cells with electrodes placed at a location 2 cm away from the end of the slit for Whatman filter paper (40, ashless, diameter-150mm, purchased from Hychem, Inc.) is shown in Fig. 3.2.
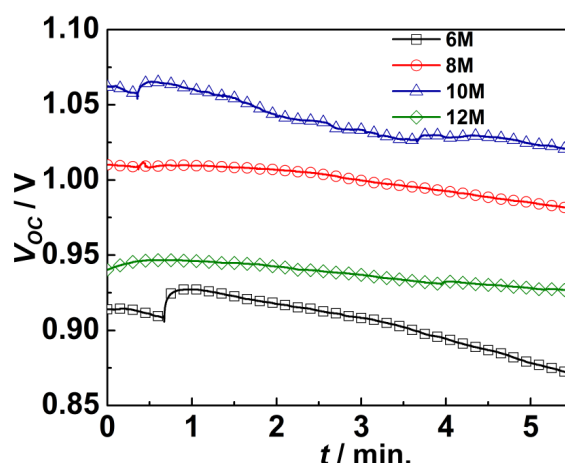
Figure 3.2: Open circuit voltage for different formic acid concentrations. The electrodes are placed 2 cm away from the end of the slit.

It can be seen that the value of OCV decreases slightly with time for all concentrations of formic acid considered in this study, i.e 6 M, 8 M, 10 M, and 12 M. A number of experiments have been performed and Fig. 3.2 shows only a representative sample. The maximum variation in OCV for each formic acid concentration across all experiments with the electrodes placed 2 cm away from the end of the slit is approximately ±0.15 V. In Fig. 3.2, the OCV decreases with time, which is essentially caused by (a) the eventual fuel and oxidant crossover, and (b) the fuel and oxidant dilution effect; factors which are detrimental to the electrochemical performance of the fuel cell. The overall cell reaction leads to the formation of CO_2 at the anode and H_2O at the cathode. Ideally the CO_2 evolved at the anode must diffuse out of the liquid phase. However, since the anode is kept below the paper strip, CO_2 can get trapped and this will lead to poor contact between the paper and the electrode [120]. Similarly the formation of H_2O at the cathode can further dilute $KMnO_4$. All these effects lead to the gradual loss in OCV. The average rate of drop of OCV for cell employing 8 M formic acid is 0.0051 V/min. For other concentrations of the formic acid, the OCV decline rate was found to lie in the range of 0.0025 to 0.0082 V/min.
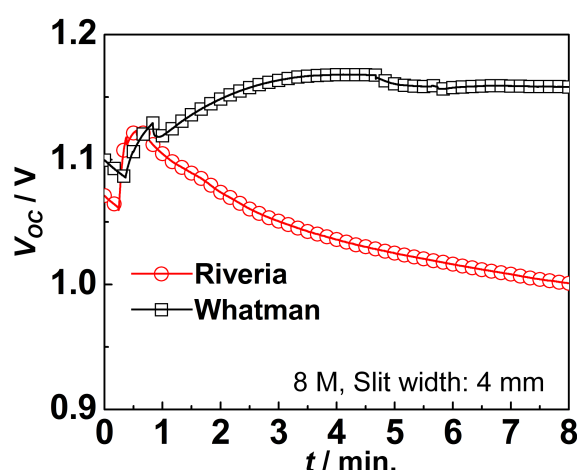
Figure 3.3: OCV versus time plots of cells supported on Whatman and Riveria filter papers with 8 M formic acid. The electrodes are placed 1 cm away from the end of the slit.

A comparison between the OCV generated by cells made using Whatman and Riveria filter papers are shown in Fig. 3.3 and the performance comparison is shown in Fig. 3.4. The difference in the performance between the two papers is due to the micro-structural difference which is shown in Fig. 3.5. From these images, it can be seen that both Whatman and Riveria filter papers appear to be anisotropic. Since Whatman filter paper based cell yields a better performance compared to the cell based on the Riveria filter paper under identical conditions, the remaining experiments were performed on cells supported on Whatman filter paper.
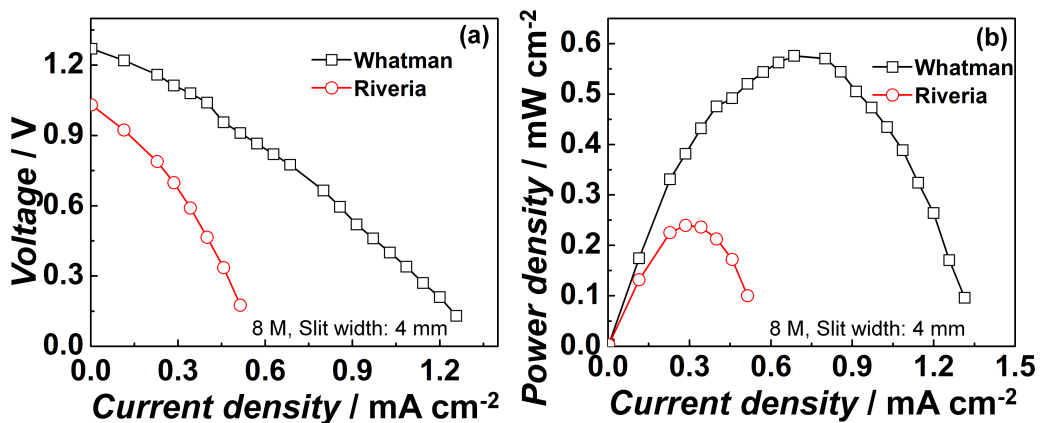
Figure 3.4: Comparisons of (a) voltage versus current density, and (b) power density versus current density between cells supported on Whatman and Riveria filter papers using 8 M formic acid. The electrodes are placed 1 cm away from the end of the slit.
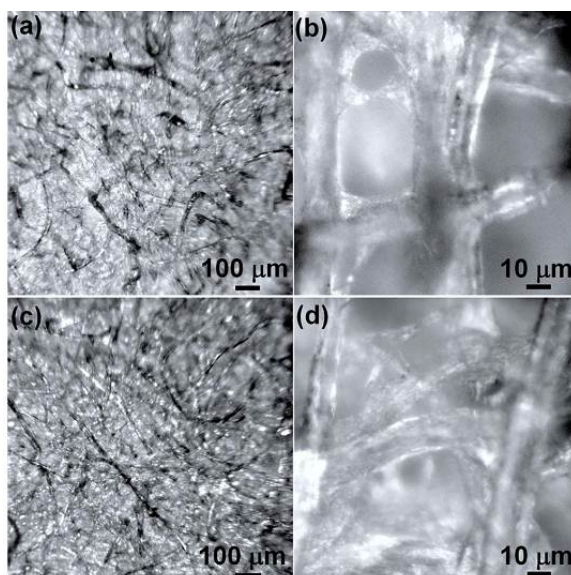
Figure 3.5: Optical microscope images of (a,b) Whatman and (c,d) Riveria filter papers.

The width of the slit and the positioning of the graphite electrodes from the end of the slit 'E' plays a key role in determining the diffusion path length of the ions. If the distance between the electrodes is long, the diffusion path length for the ions that are released at the anode to reach the cathode is enhanced, thus leading to larger Ohmic losses in the system. A similar effect is registered when the slit width is increased. The effect of electrode positioning from the end of the slit (position 'E") on the cell performance is shown in Fig. 3.6 and the corresponding power density is shown in Fig. 3.7.
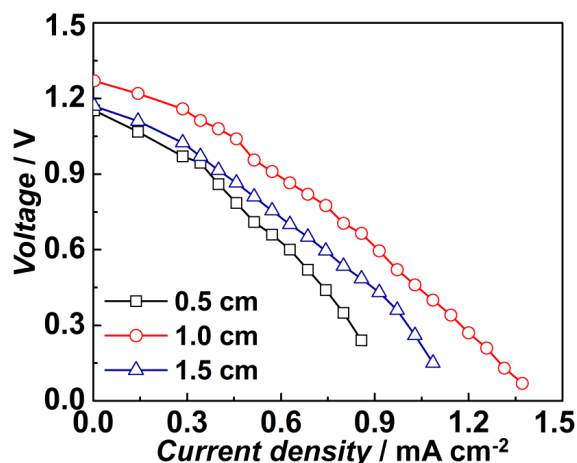
Figure 3.6: Variation in cell voltage as a function of current density for different electrode positions from the end of the slit for 8 M formic acid.
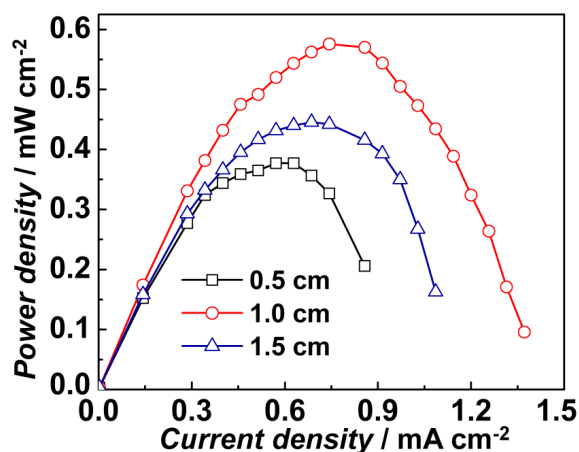
Figure 3.7: Variation in cell power density as a function of current density for different electrode positions from the end of the slit for 8 M formic acid

It is evident from these figures that the cell performance is lower when the electrode position is too close or too away from the end of the slit. When the electrodes are placed too close to the end of the slit, the fuel and oxidant crossover to the opposite electrodes, which in turn adversely affect the cell performance. On the other hand, when the electrodes are placed far away from the slit end, the Ohmic losses due to the longer path of ion transport leads to the drop in cell performance. Since for each experiment, a new cell is used, slight variations in OCV are observed between different runs, and the maximum difference is of the order of ±0.2 V. Variations in room temperature and humidity are also found to influence the cell performance slightly. Therefore, the room temperature is controlled by an air-conditioner, which maintained the room temperature at 24°C. Theoretically, one would
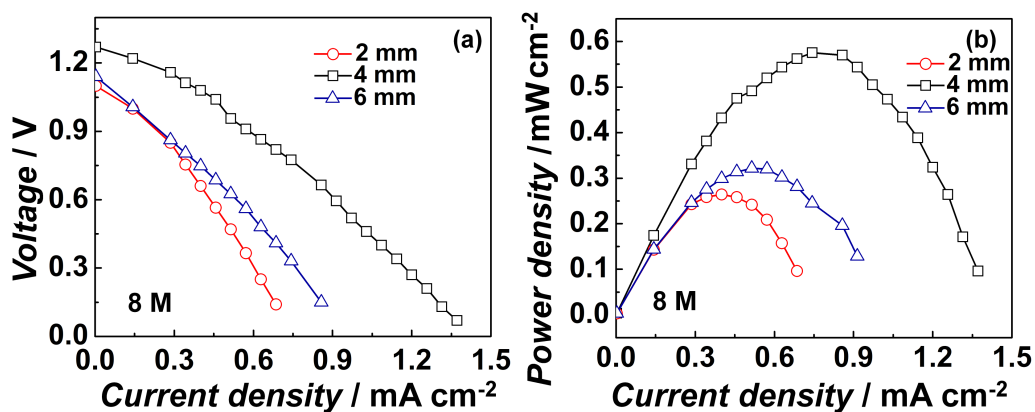
Figure 3.8: Cell performance at different slit widths using 8 M formic acid. The electrodes are placed 1 cm away from the end of the slit 'E'.

expect the same OCV in Fig. 3.6 for all electrode positions, since the Ohmic losses are completely insignificant at open circuit conditions. However, there are slight variations in the experimentally measured OCVs, and we believe that the observed differences are due to the reasons discussed above. Similarly the effect of slit width on cell performance is shown in Fig. 3.8. It can be clearly seen that the cell performance at 4 mm slit width is superior to the other slit widths considered in this study. Based on the observations made from Fig. 3.6, Fig. 3.7, and Fig. 3.8, for the rest of the experiments, the slit width and the position of the electrodes from the end of the slit 'E' are maintained at 4 mm and 1 cm, respectively.

3.3.2 Effect of concentration

The polarization behavior of the cells for different formic acid concentrations is displayed in Fig. 3.9 and Fig. 3.10. It is evident that the best cell performance is observed for the cell with 8 M formic acid and the I−V characteristics at 8 M are found to be almost linear (see Fig. 3.9) above 0.3 mA cm^{-2}. The OCV of the cell at 8 M formic acid concentration is ~1.3 V and the cell delivered a maximum power density of 0.57 mW cm^{-2} corresponding to a cell voltage of 0.77 V (Fig. 3.10). Considering that the graphite electrodes used here do not employ any catalysts, these results are highly encouraging. However, the obtained OCVs are much lower than the theoretically expected value of 1.76 V. The decrease in OCV from the theoretical value can be attributed to several factors, such as fuel cross over to the cathode, fuel and oxidant flow rates, and the rate of removal of H_2O and CO_2 bubbles, and the pH of the fuel and the oxidant [69]. Since paper is highly absorbing, any H_2O produced as a result of reduction reaction will be absorbed and will cause the dilution of the oxidant. CO_2 formation at the anode and its' accumulation may also contribute to the decrease in OCV from the theoretical value according to Nernst equation. Furthermore, the

three phase interface at the anode is accessible to air and hence depending on the oxygen partial pressure, to some extent, the unwanted direct oxidation of formic acid can also occur at the anode. Mn^{2+} formation at the cathode (graphite)/oxidant interface can also impede the reduction process at the cathode. Thus, the decrease in OCV obtained using the best configuration considered in this study from the theoretical value and its' drop with time are due to several factors. Although the presence of the slit eliminates a long mixing zone, which is typically unavoidable in the 'Y' shaped configuration, a small mixing zone is still present at the end of the slit in the cells under consideration. Thus, the presence of the slit delays the fuel and the oxidant crossover to the opposite electrodes, but does not completely eliminate it.
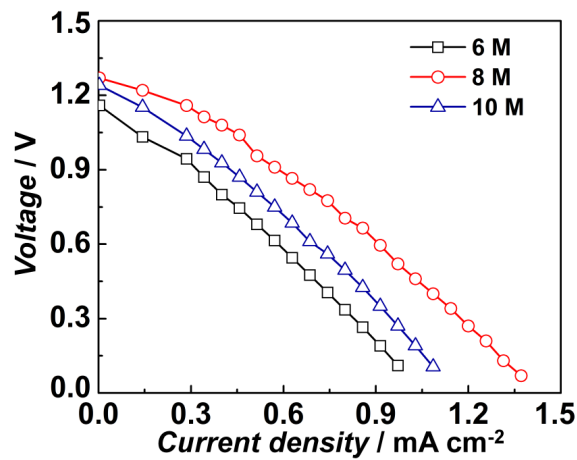
Figure 3.9: Variation in cell voltage as a function of current density for cells based on different formic acid concentrations. The electrodes are placed 1 cm away from the end of the slit 'E'.
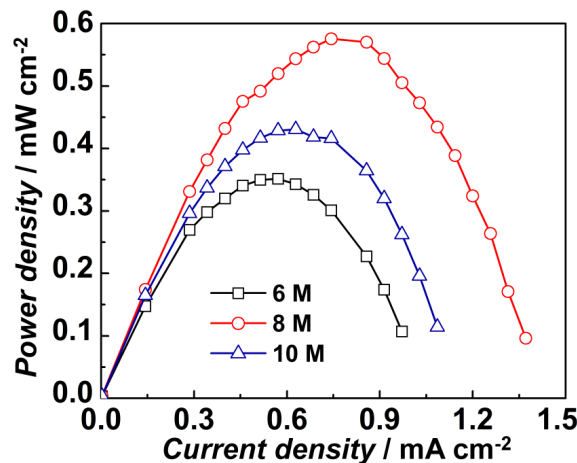
Figure 3.10: Variation in power density as a function of cell current for cells operating at different formic acid concentrations. The electrodes are placed 1 cm away from the end of the slit 'E'.

The decrease in cell performance above a certain concentration of formic acid is observed in other direct formic acid fuel cells as well [62, 63]. All the factors that lead to the drop in OCV from its' theoretical value are responsible for the lower than the expected performance of the polarized cell. At lower concentrations, the transport of formic acid at the anode and low reaction rates limits the cell performance. For higher concentrations of formic acid, faster cross over of formic acid to the cathode and loss of active area due to CO_2 formation are the main reasons for the poor performance of the cell. Since the concentration of the oxidant is kept constant, it is inferred that the the anodic processes limit the cell performance.

3.3.3 Electrochemical impedance spectra measurements

The electrochemical impedance measurement of the cells is carried out in the frequency range of 1 MHz to 0.1 Hz at OCV by applying 10 mV sinusoidal perturbation. The Nyquist plots for cell responses at different formic acid concentrations at OCV are shown in Fig. 3.11.
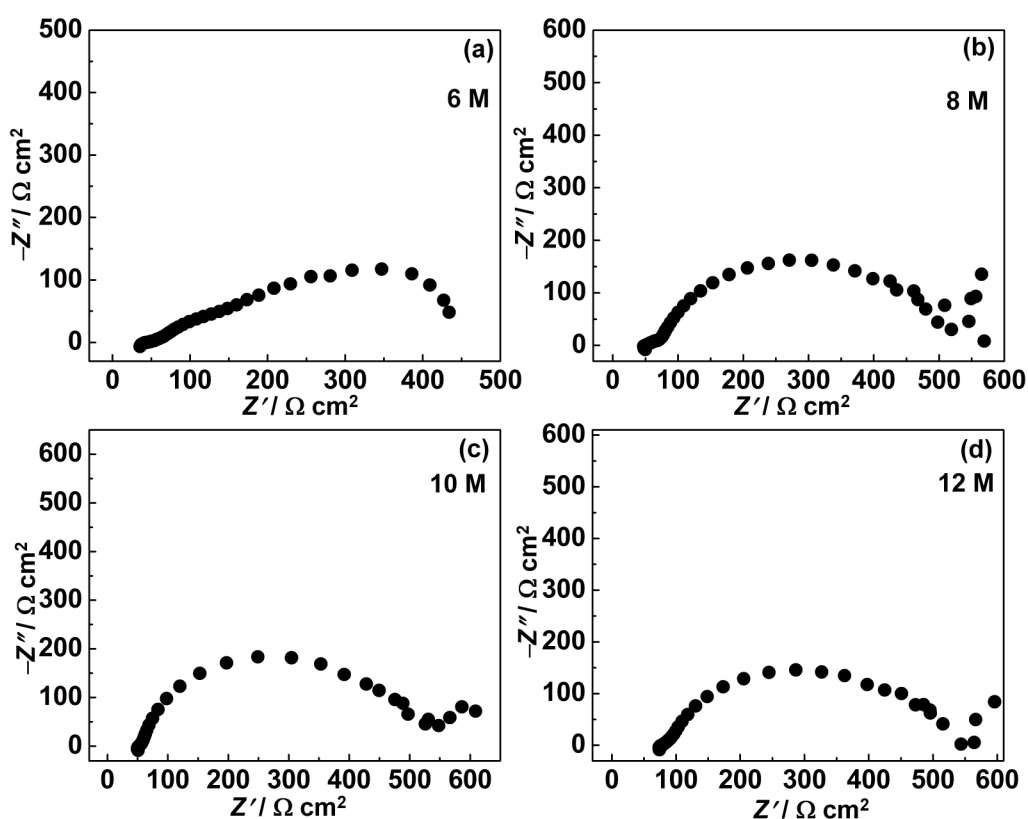
Figure 3.11: Nyquist plots of the cells with different formic acid concentrations. The relaxation frequencies observed for 6 M, 8 M, 10 M, and 12 M are 37.27 Hz and 0.372 Hz, 7.94 Hz, 10 Hz, 13.89 Hz, respectively. Note that two relaxation frequencies are observed for 6 M formic acid concentration.

All the plots exhibit typical depressed semicircle behavior due to frequency dispersion. Except for the cell with 6 M formic acid (Fig. 3.11(a)), for all other concentrations of formic acid, the Warburg impedance component is observed at low frequencies. In Fig. 3.11, panels (b)-(d) show a very limited frequency region over which mass transfer effect is present and this is insignificant as compared to the frequency region over which charge transfer resistance is present. Although the low frequency intercept is not well resolved, the charge transfer resistance of the cell slightly increases with the increase in the formic acid concentration with a moderate difference between 10 M and 12 M formic acid concentrations. Since the electro-oxidation of formic acid is a very slow process[69], significant activation losses can be expected at the anode. The dominance of charge transfer resistance over the Warburg impedance also indicates that the kinetics of the electrode reaction is rather sluggish. Since the oxidant concentration is maintained constant across all experiments, the changes in charge transfer resistances are induced by the variation of formic acid concentration and hence the electrochemical kinetics at the anode. Since the impedance measurements are made at OCV by applying a small amplitude (10 mV) sinusoidal perturbation, the activation over potential will be small and the current response will be linear.
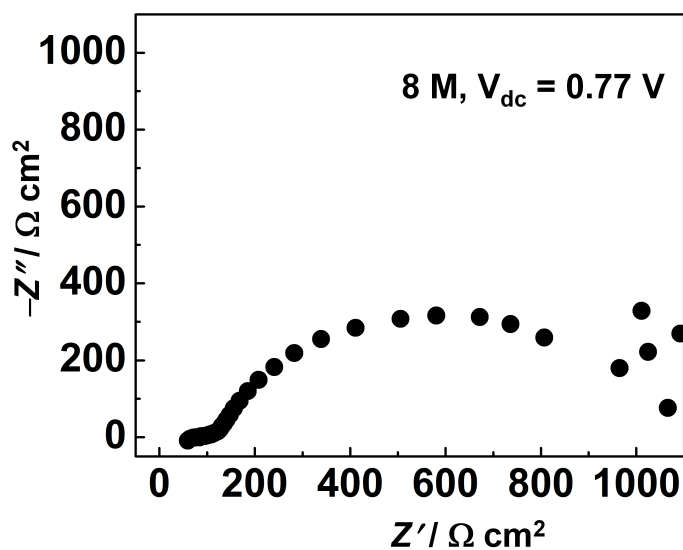
Figure 3.12: Nyquist plot showing the impedance response of the cell at 0.77 V using 8 M formic acid on Whatman filter paper.

Under such conditions, the charge transfer resistance R_{ct} is related to the exchange current density according to,

$$R_{ct} = \frac{RT}{n_e F i_0},$$ (3.4)

which leads to an exchange current density of 10^{-2} mA cm^{-2} for the cell with 8 M formic

acid concentration. The high frequency resistance also varies slightly with the formic acid concentration. The impedance response of the cell with 8 M formic acid at 0.77 V with 10 mV amplitude sinusoidal perturbation in the frequency range of 1 MHz to 0.1 Hz is shown in Fig. 3.12. The potential of 0.77 V corresponds to the maximum power density delivered by the cell with 8 M formic acid using Whatman filter paper (Fig. 3.10). Although not very distinct, two semicircles can be observed in Fig. 3.12. The high frequency intercept ($R_\Omega = 59.68$ Ω cm^2) is comparable with the Ohmic resistance of the cell at open circuit conditions, however, the charge transfer resistance ($R_{ct} = 1000$ Ω cm^2) is much higher at the part load condition. Typically, the polarization resistance should decrease when the cell is partly loaded. Therefore, the increased polarization resistance here is probably due to CO_2 accumulation at the anode. Similar to the cell response at OCV, here also mass transfer limited charge transport is confined to a very narrow range near the low frequency.
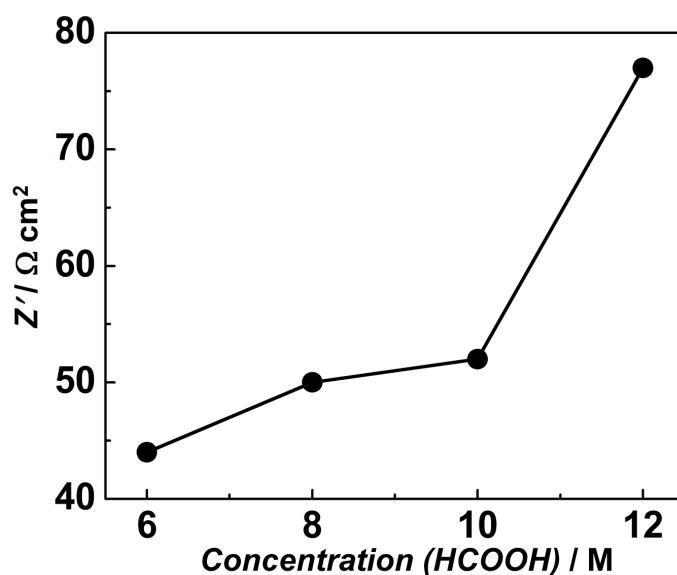
Figure 3.13: Variation of Ohmic resistance of the cells as a function of formic acid concentration.

The variation of Ohmic resistance of the cells with formic acid concentration is shown in Fig. 3.13. As the concentration of formic acid increases, the Ohmic resistance of the cell also increases. When concentrated formic acid is used in cells with a membrane, particularly based on membrane electrode assemblies that require to be maintained in the hydrated state, the high frequency resistance increases due to membrane dehydration [63]. This major drawback is eliminated in the case of a membraneless configuration, such as the one presented here.
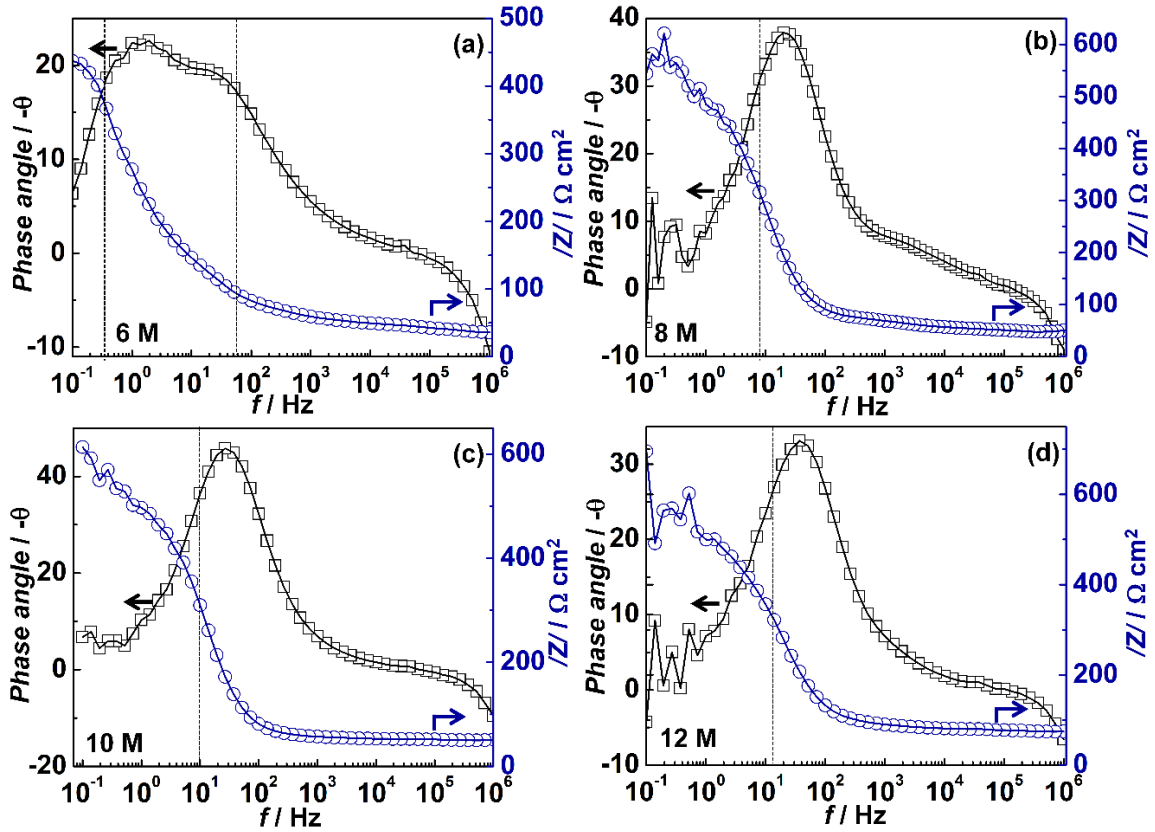
Figure 3.14: Bode diagram corresponding to the impedance curves given in Fig. 3.11. The black dashed constant frequency lines correspond to the relaxation frequencies presented in Fig. 3.11 for different values of concentration of formic acid.

Nevertheless, even in this membraneless configuration, the high frequency resistance increases with formic acid concentration, a behaviour similar to the membrane based cells. This trend is in very good agreement with the findings of Rice et al [62]. However in their case it was the membrane dehydration that resulted in the increase in cell resistance with increase in formic acid concentration. Since the cell considered in the present study is a membraneless one and formic acid is a very good electrolyte, the proportion of protons available for ionic transport is expected to increase with formic acid concentration. Furthermore, H_2SO_4 is also a very good proton conductor. The proton conductivity of 0.5 M H_2SO_4 is of the order of 0.2 S cm^{-2}, which is twice as that of Nafion at 100% relative humidity [69]. In calculating the cell impedance, it is assumed that a geometric surface area of 0.35 cm^2 of the graphite electrode is in contact with the paper. However, the actual contact area will be much smaller after CO_2 bubble formation, and therefore the cell impedance will be smaller than that of the value calculated using the visible contact area. Since in the configuration used here, the paper strip is placed above the anode, it is not possible to observe the bubble formation. For a similar set up, Arun et al. [47] observed the forma-

tion of CO_2 bubbles at the anode. Therefore, the only reasoning here for the increase in cell resistance with formic acid concentration is the formation of tiny CO_2 bubbles, which reduces the contact area.
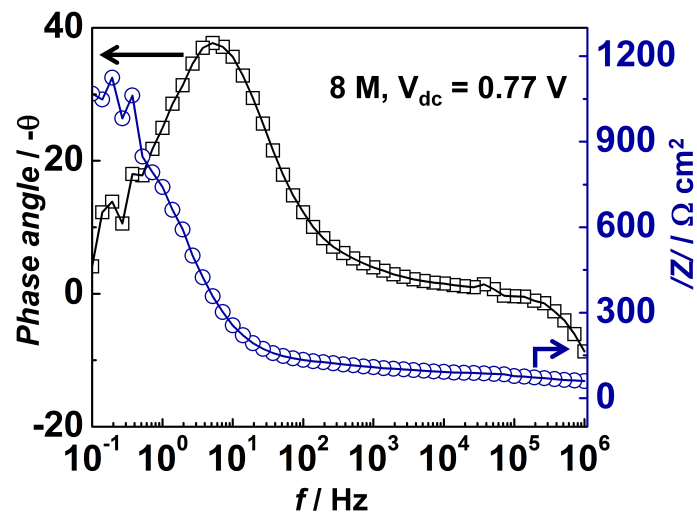
Figure 3.15: Bode diagram corresponding to the impedance curve given in Fig. 3.12.

The Bode diagrams corresponding to the impedance plots presented in Fig. 3.11 are shown in Fig. 3.14. In all cases, the phase angle, defined as $\theta = \tan^{-1}(Z_i/Z_r)$ is well below -45 degree indicating that the process can not be represented using a RC circuit. For a pure RC circuit, the phase angle reaches -45 degree at the characteristic frequency. For the concentration range of 8 M-12 M, at the characteristic frequency the phase angle varies between -25 to -35 degrees. For the cell with 6 M formic acid concentration, two relaxation frequencies are observed. In Fig. 3.11(b)- Fig. 3.11(d), it is observed that at high frequencies an inductance contribution is present over a small range, probably because of the lead, which makes the phase angle positive at the high frequency limit. The Bode diagram corresponding to Fig. 3.12 (8 M cell supported on Whatman filter paper) is shown in Fig. 3.15. The variation of phase angle (at 0.77 V, corresponding to maximum power density) with frequency is similar to the trand observed for the same cell at OCV. The phase angle is -28 degree at the characteristic frequency and an inductance component is present in the high frequency limit.

The equivalent circuit for each impedance plot is shown in Fig 3.16. One of the major drawback with equivalent circuits fitting is that more than one circuits can lead to the same impedance response and indirect inferences need to be drawn between different circuit elements used and the physico-chemical prcesses in the system. The simplest circuit that can fit the responce of a fuel cell is the Randles circuit. The impedance response of the systems studied in this thesis are studied using either full or half Randles circuit. Since the

43

Randles circuit provides reasonable re-production of experimental measurements, more complex circuits are not attempted.
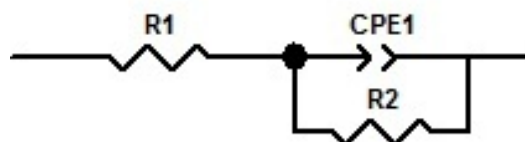
Figure 3.16: Equivalent circuit model representing half Randles circuit.

The equivalent circuit shown in Fig 3.16 has three elements, namely - R_1, R_2 and CPE_1 (constant phase element). R_1 corresponds to ohmic resistance, which in turn is composed of ionic (Rionic) and electronic resistance (Relec). The electronic resistance originates from the carbon/graphite based electrodes and other conducting parts of the cell. However, since graphite is a good electronic good conductor, R_{elec} can be ignored. R_{ionic} is due to the resistance offerred by the electrolyte phase for the transport of ions, known as the solution resistance. Therefore, R_1 mainly corresponds to the solution resistance. CPE_1 is the constant phase element which is the capacitance of the double layer formed at the electrode/electrolyte interface. CPE denotes the capacitance of a non-ideal capacitor which leads to a depressed semicircle. Parallel to CPE_1 is R_2 which is the charge transfer resistance for electrochemical reactions taking place at the electrode. Warburg impedance and inductance have been ignored in all the equivalent circuits due to their relatively small contribution as compared to R_1 and R_2.

The comparison between the experimental and simulated data, for formic acid are shown in Fig. 3.17 (a)-(d) The simulated values show good agreement with the experimental ones. In reproducing the data, the impedance response at the low frequency region is ignored due to the scattering of the data, which is a result of unsteady behaviour of the cell performance. Since only one semicircle is observed in the experiments, a half Randles circuit is used to fit these data. In the experiments, the catholyte concentration is kept constant, and changes in the fuel concentration lead to changes in the high and low frequency intercepts. Therefore, it is assumed that the semicircle observed is due to the relaxation frequencies of the anodic processes. It could also be possible that the relaxation frequencies of the anodic and cathodic processes are very close to each other or one process is masking the other.

44
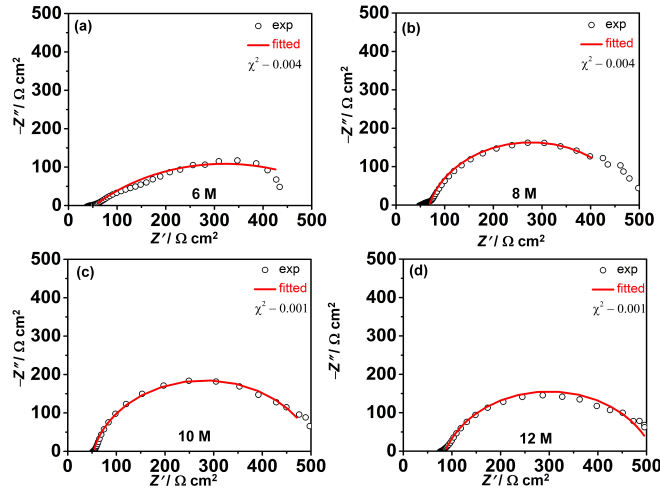
Figure 3.17: Nyquist plots of the cells with different formic acid concentrations. The relaxation frequencies observed for 6 M, 8 M, 10 M, and 12 M are 37.27 Hz and 0.372 Hz, 7.94 Hz, 10 Hz, 13.89 Hz, respectively. Note that two relaxation frequencies are observed for 6 M formic acid concentration. Experimental data is represented by open symbols. Lines represent fitted/simulated results

3.4 Concluding remarks

In this work, a low cost, environmentally friendly porous paper based fuel cell operating on formic acid (HCOOH) as the fuel and potassium permanganate (KMnO$_4$) as the oxidant is presented. The oxidation of formic acid at the anode is achieved using a graphite sheet electrode without the use of any metal catalysts. Although the paper based fuel cell functions according to the principles of laminar flow fuel cells, fuel-oxidant mixing can still occur due to the anisotropy associated with the cellulose fibres and hence the cell performance is strongly dependent on the micro-structure of the filter paper. In order to delay the fuel and oxidant cross over a slit is provided at the center of the paper strip. Although the slit delays the cross over effects, it also increases the Ohmic resistance of the cell due to the longer diffusion path for the ions to reach the cathode. In addition to the slit width the position of electrodes from the end of the slit also plays a major role in deciding the cell performance. Based on the slit width and the electrode position studies, for cell characterization the slit width is maintained at 4 mm the electrodes are placed at 1 cm away from the end of the slit. The best cell performance is obtained for 8 M formic acid concentration, which is in close agreement with the observations made in other direct formic acid fuel cells. The cell with 8 M formic acid delivers an OCV of 1.3 V, with a maximum power density of 0.57 mW cm^{-2} at 0.77 V. Several factors, such as fuel cross over, fuel and oxidant dilution contribute to the loss in OCV from its' theoretical value. Electrochemical impedance spectroscopic

data analysis reveals that the kinetics of the cell is sluggish due to the slow oxidation kinetics of formic acid. Furthermore, for all formic acid concentrations, at the characteristic frequency the phase angle lies between -25 and -35 degrees indicating that the cells do not follow an ideal Randles circuit. The impedance response of the cell at 0.77 V showed in a higher polarization resistance, however, the phase angle variation s similar to that at OCV. Finally, the power delivered by the cell is sufficient to power MNSs whose power requirements are in the range of milli-watts to nano-watts. The successful implementation of the $HCOOH-H_2SO_4-KMnO_4$ fuel cell at room temperature by using an over simplified paper based architecture opens up many opportunities to apply this configuration to yet unexplored alkali/methanol based fuel cell systems.

Chapter 4

Paper based hydrazine monohydrate-permanganate fuel cells

4.1   Introduction

In Chapter 3, the development and characterization of a paper based formic acid is presented. Under the conditions investigated, the cell produced a maximum power density of 0.57 mW cm^{-2} at a cell potential of 0.77 V. The redox couple chosen for the formic acid cell had a standard cell potential of 1.76 V.

In search for better performance this chapter presents the development and characterization of a paper based fuel cell with hydrazine monohydrate as fuel. Apart from HCOOH, hydrazine monohydrate ($N_2H_4.H_2O$), is another promising candidate for paper based fuel cells. The oxidation of hydrazine monohydrate leads to the formation N_2 and H_2O, both of which are harmless to the environment. Moreover, hydrazine based fuel cells can operate at low temperatures and deliver high power densities [75, 60]. One downside of using hydrazine is that, it is hazardous when handled in pure form. Therefore, it is generally stored in aqueous solutions or in solid form as hydrazone. Although not for laminar flow based systems, the working of hydrazine-hydrogen peroxide fuel cells at low temperatures has also been demonstrated [75, 60]. Typically, Pt has been used as the electro-catalyst in these systems.

The oxidant ($KMnO_4$) used here remains same as the one used for formic acid cell presented in Chapter 3. With hydrazine monohydrate as fuel, the redox couple has a standard potential of 2.72 V. The high standard potential leads to high OCV of 2.0 V, which is almost 0.8 V higher than formic acid fuel cell. With high OCV, the cell still delivers appreciable cell potential after sacrificing for the overpotential losses. Carbon cloth-stainless steel plates were used as the electrodes-current collector, instead of graphite, as they are easy to machine and process. The power density reaches a value of 1.16 mW cm^2 with

the same configuration as that of the formic acid fuel cell. In order to improve the cell performance of the same paper cell, hydrazine monohydrate has been employed as the fuel, along with Cu and functionalized multiwalled carbon nanotubes (f-MWCNTs) based composite catalysts. With the use of metal catalyst, this cell configuration is able to deliver a maximum power density of 3.58 mW cm^2. The reason for employing Cu and carbon-based catalysts is that, these non-noble metal-based catalysts are cheap, available in abundance and can be synthesized easily. Also, Cu has a good electrocatalytic activity towards the oxidation of hydrazine monohydrate, and when combined with MWCNTs, its activity is enhanced further, due to the better electrical conductivity and more active surface area provided by MWCNTs. A mixture of $N_2H_4.H_2O$ and NaOH formed the anolyte and a mixture of $KMnO_4$ and H_2SO_4 formed the catholyte.

The half cell reaction at the anode is given by

$$N_2H_4 + 4OH^- \rightleftharpoons N_2 + 4H_2O + 4e^- \quad (E^0 = -1.21\ V). \tag{4.1}$$

and the half cell reaction at the cathode is given by

$$2Na^+ + SO_4{}^{2-} + MnO_4{}^- + 8H^+ + 5e^- \rightleftharpoons Mn^{2+} + \tag{4.2}$$
$$4H_2O + Na_2SO_4 \quad (E^0 = 1.51\ V).$$

The overall reaction is given by

$$5N_2H_4 + 32H^+ + 4MnO_4{}^- + 8Na^+ + 4SO_4{}^{2-} + 20\ OH^- \rightleftharpoons 5N_2 + \tag{4.3}$$
$$36H_2O + 4Mn^{2+} + 4Na_2SO_4 \quad (E^0 = 2.72\ V).$$
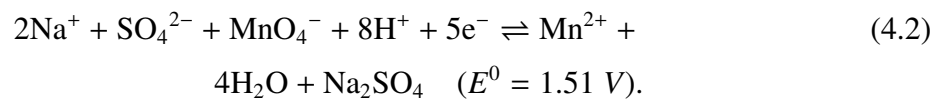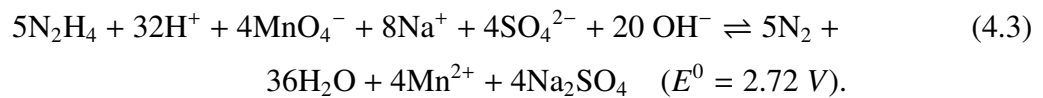
These reactions are very much similar to the N_2H_4 fuel cell reported by Yan et al., [60] where Na^+ (present in the anolyte is the mobile ion, which migrates from the anode to the cathode side. Instead of $KMnO_4$, they used H_2O_2 as the oxidant. However, in this case Na^+ cation comes from the dissociation of NaOH which is the electrolyte at the anode side. Its worth noticing that in these cells, the electrolyte phase also participates in the electrochemical reactions. The oxidation of the fuel and reduction of the oxidant is caused by the electrolyte phase rather than the oxidizing or reducing agent.

4.2 Experimental methods

4.2.1 Chemicals

Hydrazine monohydrate ($N_2H_4.H_2O$, 99%), Cupric sulfate ($CuSO_4 \cdot 5H_2O$, 99 %), potassium permanganate, ($KMnO_4$, 98.5%), polyethylene glycol (PEG-9000), sodium borohy-

dride (NaBH$_4$, 98%) nitric acid (HNO$_3$, 69%) and sodium hydroxide pellets (NaOH, 99 %) were purchased from Merck, while L-ascorbic acid (99.7 %) was purchased from Sisco research labs. Sulfuric acid (H$_2$SO$_4$, 90%) was purchased from Fisher Scientific, and MWCNTs were purchased from Sigma Aldrich. Whatman filter paper (ashless, 40) served as the medium for the transport of anolyte and catholyte.

4.2.2 Preparation of catalysts and electrodes

Cu nanoparticles (Cu-NPs)

Copper nanoparticles (Cu-NPs) were prepared following a procedure described elsewhere [121], which is briefly outlined below. A solution containing 0.01 M of CuSO$_4$.5H$_2$O and 0.02 M polyethylene glycol (PEG) (capping agent) was prepared in deionized water and stirred vigorously. This was followed by drop-wise addition of 0.02 M ascorbic acid (acts as an antioxidant) and 0.1 M NaOH to the above solution under continuous stirring. Finally, 0.1 M NaBH$_4$, the reducing agent, was added to complete the reaction and the solution was stirred for 10 minutes. The final solution containing Cu-NPs was dark green in color, which was centrifuged and washed with distilled water to isolate the final product and was dried in a vacuum oven at 85°C for 12 hours. 5 mg of Cu-NPs were dispersed in 1 mL of tetrahydrofuran (THF), sonicated for 20 minutes and deposited onto the electrodes (carbon cloth) by drop casting using a pipette.

Functionalized multiwalled carbon nanotubes (f-MWCNTs)

Multiwalled carbon nanotubes (MWCNTs) were first functionalized by dispersing and sonicating them in HNO$_3$ and H$_2$SO$_4$ (volume ratio of 1:3). This solution was then refluxed at 80°C, followed by filtering and washing with copious amounts of distilled water till the solution neutralized. The filtrate was then dried in a hot air oven at 60°C for 2 days. The resulting product is referred to as f-MWCNTs. 2 mg of f-MWCNTs in 0.5 mL of toluene was prepared by sonication, and deposited on carbon cloth by drop casting and dried in air prior to use as electrodes.

Cu-NPs@f-MWCNTs composite

For the preparation of the Cu-NPs@f-MWCNTs composite, f-MWCNTs were added in-situ to a solution of 0.01 M of CuSO$_4$.5H$_2$O, 0.02 M PEG, 0.02 M ascorbic acid and 0.1 M NaOH, and this mixture was stirred for a few minutes. A 0.1 M NaBH$_4$ solution was then added to this solution and was stirred for 10 minutes. Once the reaction was complete, the product was isolated from the solution by subsequent washing with distilled water and acetone, followed by drying in a vacuum oven at 85 ^{circ}C for 24 hours. The resulting product

is referred to as Cu-NPs@f-MWCNTs composite. Approximately, 5 mg of the composite catalyst powder was then dispersed in 1 mL toluene, and sonicated for 1 hour and then deposited onto the electrodes (carbon cloth) by drop casting.

4.2.3 Construction of paper based fuel cells

The paper cell was assembled by placing two 7 cm long paper strips, with a width of 0.7 cm each, separated by a 0.4 cm $\times$ 3.5 cm slit in between and connected to each other at a distance of 3.5 cm from point 'B' (see Fig. 4.1). The electrodes were placed on each of the lateral strips and were connected externally by using steel plate as current collectors. The area of the electrode used was 0.35 cm^2 for each one. A schematic of the cell assembly is shown in Fig. 4.1. The anolyte was prepared by mixing $N_2H_4.H_2O$ with NaOH (4 M) and the catholyte was prepared by mixing $KMnO_4$ (1 M) and H_2SO_4 (4 M). An absorbing pad was placed at one end of the assembly to absorb the excess fluids. The anolyte and catholyte were discharged manually using a pipette near the electrodes.
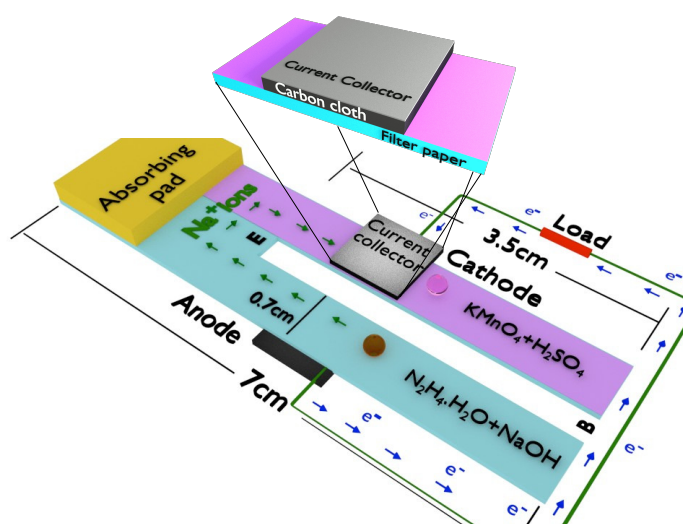
Figure 4.1: Schematic representation of paper cell and the electrode current collector assembly used in the experiments. The green arrows indicate the transport of Na$^+$ ions from the anode to the cathode.

4.2.4 Characterization techniques

Electrochemical measurements, such as chronopotentiometry, chronoamperometry and electrochemical impedance spectroscopy were done using an Autolab PGSTAT 302N with a frequency response analyzer. The measurements were performed using a NOVA 1.6 software. Cu-NPs and Cu-NPs@f-MWCNTs composite were characterised by a UV-Vis-NIR spectrophotometer (Shimadzu UV-3600). The morphology and the structure of Cu-NPs, f-MWCNTs and Cu-NPs@f-MWCNTs composite were investigated by field emission scan-

ning electron microscopy (FE-SEM, Carl Zeiss Supra 40) and X-ray powder diffraction (XRD, PANalytical, X'PertPRO) instrument with Cu-K$_\alpha$ (λ = 1.5406A°). Transmission electron microscope (Philips TEM CM 200), resolution 2.4 A°, was used for characterizing the catalysts by transferring a thin layer of the samples to carbon coated copper grids. The composition of the composite was estimated using thermogravimetric analysis, Pyris 1 TGA, PerkinElmer, under helium atmosphere, at a temperature ramp of 10 °C/min. Raman spectra of functionalized MWCNTs (f-MWCNTs) and Cu-NPs@f-MWCNTs composite were recorded using a Bruker Senterra Raman Spectrometer, at λ = 532nm.

4.3 Results and discussion

4.3.1 Structural features of catalysts

Prior to studying the electrochemical characterization of the paper based fuel cells, the structural characterization of the catalysts is performed. Fig. 4.2(a) shows the absorption spectra for Cu-NPs and the Cu-NPs@f-MWCNTs composite.
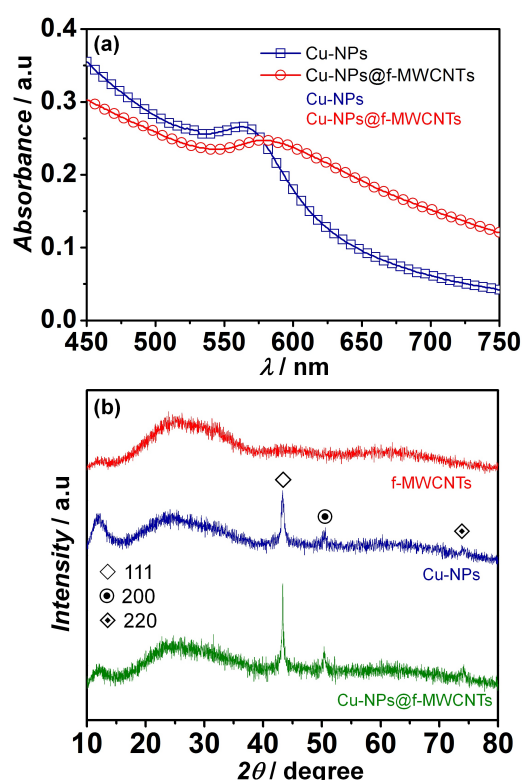
Figure 4.2: (a) Diffuse reflectance UV-Vis spectra of Cu-NPs and Cu-NPs@f-MWCNTs composite. (b) XRD patterns of f- MWCNTs, Cu-NPs and the Cu-NPs@f-MWCNTs composite.

The Cu-NPs show a broad peak in the visible region with a $\lambda_{\max}$ at 573 nm, which is due to the surface plasmon resonance (SPR) effect of the metal NPs. Upon inclusion of the f-MWCNTs, as in the Cu-NPs@f-MWCNTs composite, this peak is red shifted by 6 nm to 579 nm, due to the increased refractive index of the composite, induced by the f-MWCNTs. In Fig. 4.2(b), the XRD patterns of Cu-NPs, Cu-NPs@f-MWCNTs composite and f-MWCNTs are shown. The f-MWCNTs show a featureless diffractogram indicating that the CNTs are amorphous. Cu-NPs show three peaks at $2\theta= 43.3^{\circ}$, 50.44° and 74.125°, which agree well with the (111), (200) and (220) planes of the face centered cubic (fcc) lattice of Cu, in accordance with PDF: 892838. The XRD pattern of the Cu-NPs@f-MWCNTs composite also shows the same three diffraction peaks of Cu with no additional feature, indicating that crystalline Cu-NPs are dispersed in an amorphous f-MWCNTs matrix.
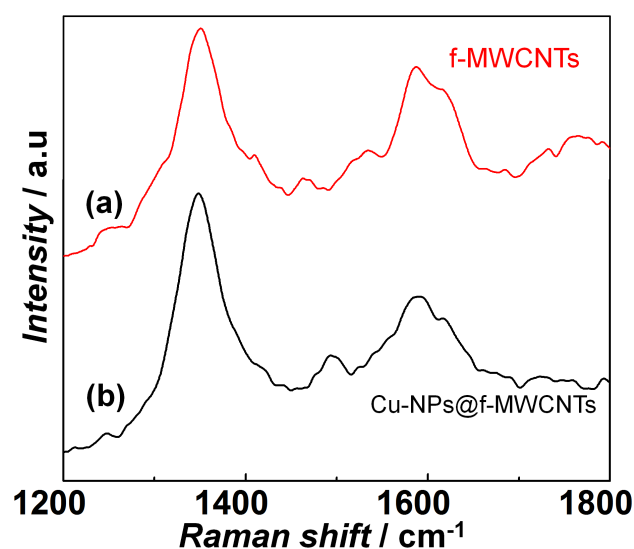
Figure 4.3: Raman spectra of f-MWCNTs and Cu-NPs@f-MWCNTs composite catalysts.

The Raman spectra for f-MWCNTs and Cu-NPs@f-MWCNTs is shown in Fig. 4.3, wherein the peaks for G-band and D-band are formed at 1594 cm^{-1} and 1347 cm^{-1}, respectively. Although, there is no significant peak shift is observed, but the I_D/I_G ratio increases from 0.8 in f-MWCNTs to 1.1 in Cu-NPs@f-MWCNTs composite, which means the extent of defects increased in the latter, due to the bonding of the Cu-NPs (via Van der Waals force between the -OH and -COOH polar groups present on Cu-NPs and f-MWCNTs, respectively) onto the walls of the carbon nanotubes. However, in Fig. 4.3, emergence of a broad peak is seen at around 1630 cm^{-1}. This usually happens because the sp^2 hybridized C-atoms are sensitive towards any strain or abrasion caused by inter or intra-layer interactions, in that case the G-band gets easily modified or distorted and this leads to formation of

multiple peaks or broader peaks in the Raman spectrum. Mildred and co-workers demonstrated the same phenomenon, however in their case this effect was observed for SWCNTs (single walled-CNTs) [122].

The FE-SEM images of Cu-NPs, f-MWCNTs and Cu-NPs@f-MWCNTs composite are shown in Fig 4.4. The images of Cu-NPs, given in Fig 4.4(a) and (b) shows aggregated interlinked particles and the dimensions of the aggregates are of the order of a few hundred nanometers and they have no definite shapes.
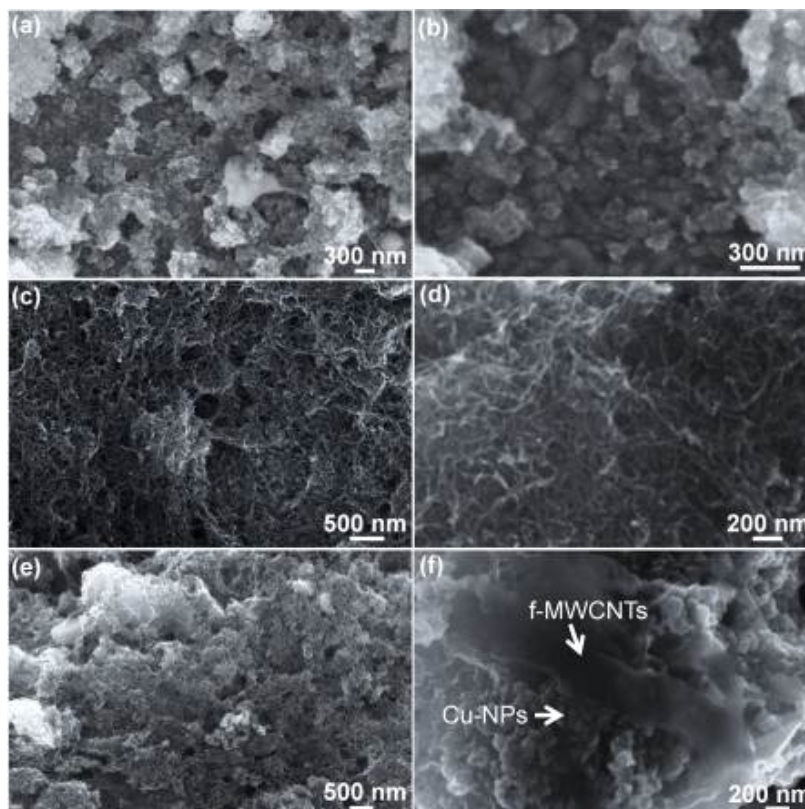
Figure 4.4: FE-SEM images of (a and b) Cu-NPs, (c and d) f-MWCNTs, and (e) and f) the Cu-NPs-MWCNTs composite.

The images of the f-MWCNTs (Fig 4.4 (c) and (d)), show a fibrillar morphology, comprising of a densely packed network of intertwined nanotubes. The nanotubes form bundled clusters. The low magnification image of the Cu-NPs@f-MWCNTs composite (see Fig 4.4 (e)) shows a mixed morphology, wherein the aggregates of Cu-NPs coat the fiber like shapes of f-MWCNTs uniformLy. The discrete but entwined nanotubular structures observed for the f-MWCNTs, are not distinctly visible for the composite. From the undulating contours of the image, it is perceived that the aggregated particles of Cu tend to envelope the f-MWCNTs.
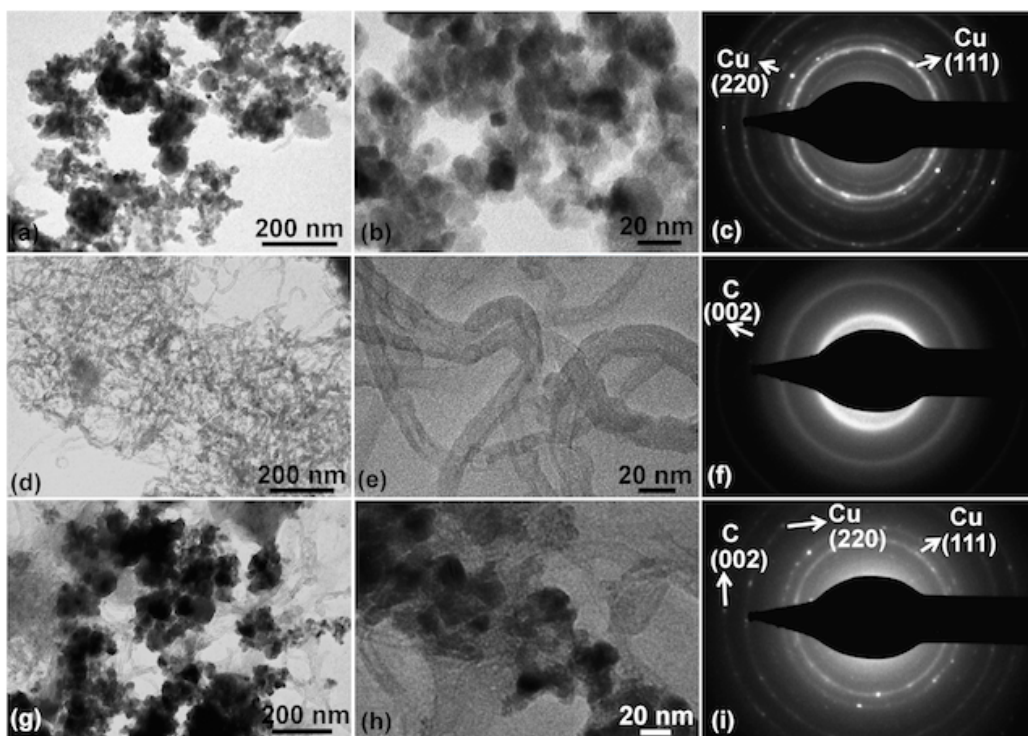
Figure 4.5: TEM images of (a and b) Cu-NPs, (c) SAED pattern of Cu-NPs, TEM images of (d and e) f-MWCNTs, (f) SAED pattern of f-MWCNTs, TEM images of (g and h) the Cu-NPs@f-MWCNTs composite, and (i) SAED pattern of the Cu-NPs@f-MWCNTs composite.

Fig. 4.5 (a) and (b) show the TEM images for Cu-NPs at low and high magnifications, respectively. The particle size varies from 8 to 30 nm (based on a couple of micrographs). The particle dispersion and size distribution are non-uniform, due to the agglomeration among the NPs. Fig. 4.5 (c) shows the selected area electron diffraction (SAED) pattern of Cu-NPs. A spotty concentric ring pattern is observed, and the bright spots are indexed to the (220) and the (111) planes corresponding to inter planar spacing of 0.13 and 0.24 nm of Cu, as per PDF: 892838. The micrographs of f-MWCNTs (Fig. 4.5 (d) and (e)) reveal highly entangled and tubular structures, characteristic of f-MWCNTs. The length of the nanotubes extend to several microns and the outer diameters lie in the range of 14-20 nm. The corresponding SAED pattern shows concentric diffuse rings devoid of spots, thus, re-affirming the almost amorphous nature of the CNTs. One of the rings indexed to the (002) plane of graphitic carbon, corresponding to an inter planar distance of 0.34 nm. The TEM micrographs of the Cu-NPs@f-MWCNTs composite (Fig. 4.5(g) and (h)), show aggregates of Cu-NPs attached to the tangled network of the tubular structures of f-MWCNTs. From the micrographs, it is evident that a reasonably good mixing of Cu-NPs with f-MWCNTs is achieved in the composite. The corresponding SAED pattern shows spots assigned to the (220) and (111) planes of Cu with a fcc lattice and the ring due to the (002) plane of

graphite carbon, thus confirming the formation of the composite.

4.3.2 Effect of fuel concentration

To identify the fuel concentration for the best cell performance, three different $N_2H_4.H_2O$ concentrations (4 M, 6 M and 8 M) are investigated (without using any catalysts). The catholyte concentration is kept constant in all the experiments at 1 M $KMnO_4$ and 4 M H_2SO_4. The voltage-current density and power density-current density curves are shown in Fig. 4.6. A fuel concentration of 6 M delivers better performance compared to 4 M and 8 M. At lower concentrations, the slower oxidation kinetics limits the cell performance, whereas at higher concentrations, the anolyte cross over from the anode to the cathode becomes prominent. Anolyte/Catholyte cross over is a time dependent phenomenon and since a new cell was used for each experiment, the effect of anolyte/catholyte cross over is observed only during the later stages of the experiment, i.e., when the cell becomes more and more polarized. A still image showing the cross diffusion of anolyte and catholyte is show in Fig 4.8, which clearly shows that the diffusion is faster at higher fuel concentration (8 M) as compared to lower concentration (4 M).
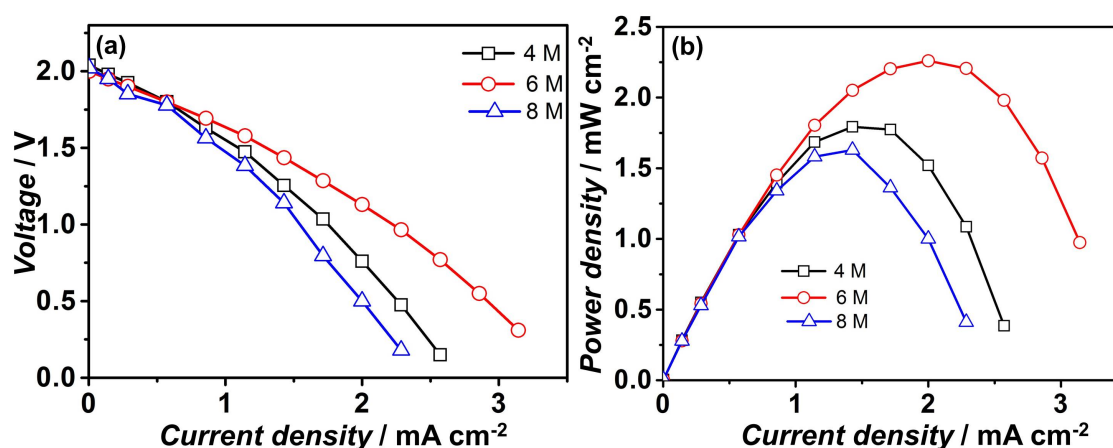
Figure 4.6: (a) Cell voltage versus current density, and (b) power density versus current density at 4 M, 6 M and 8 M concentrations of $N_2H_4.H_2O$ with 4 M NaOH as anolyte. The catholyte is 1 M $KMnO_4$ + 4 M H_2SO_4. These experiments are performed using graphite sheet as electrode.

4.3.3 Effect of electrode position

Besides optimizing the fuel concentration, the position of the electrodes is also varied from the end of the slit 'E', to determine the best electrode position for cell performance. Placing the electrodes too close to the junction 'E' decreases the diffusion path for the ions, but, increases the fuel and catholyte cross over effects. Placing the electrodes too far from

the junction 'E' leads to an increase in the diffusion path and hence the Ohmic resistance increases. After a number of experiments, the electrode position is fixed at 0.5 cm from the junction 'E'. The effect of electrode position on the cell performance is shown in Fig 4.7. For all the results presented in this study the $N_2H_4.H_2O$ concentration is fixed at 6 M and the electrodes were placed at 0.5 cm from the point 'E'.
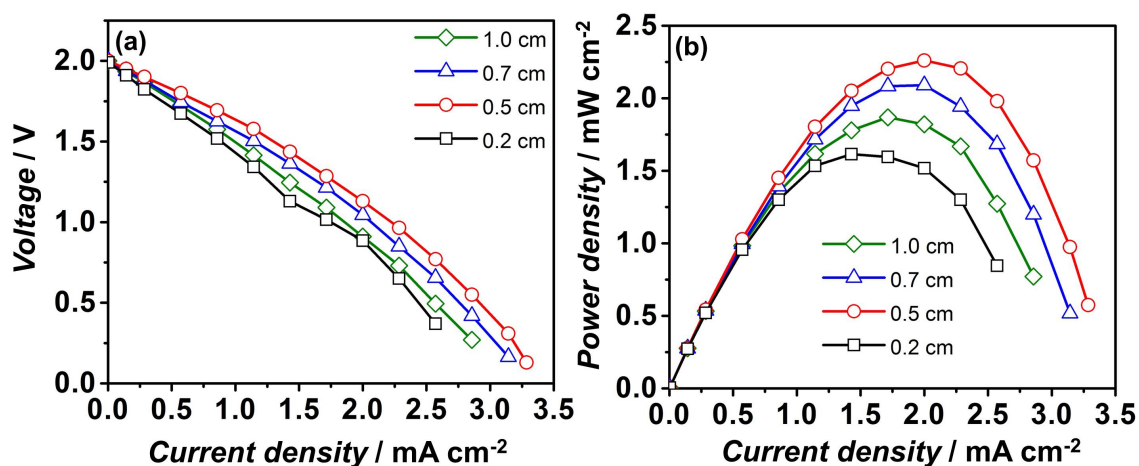
Figure 4.7: Polarization curves: (a) voltage versus current density and (b) power density versus current density for cells with electrodes (cathodes and anodes) placed at different positions (in cm) from point E (shown in Fig. 1). The anolyte is 6 M $N_2H_4.H_2O$ + 4 M NaOH, the catholyte is 1 M $KMnO_4$ + 4 M H_2SO_4. These experiments are performed using graphite sheet as electrode.

(a) Anolyte and catholyte diffusion at the beginning of the experiment

(b) Anolyte and catholyte diffusion after 7 min

(c) Anolyte and catholyte diffusion after 15 min
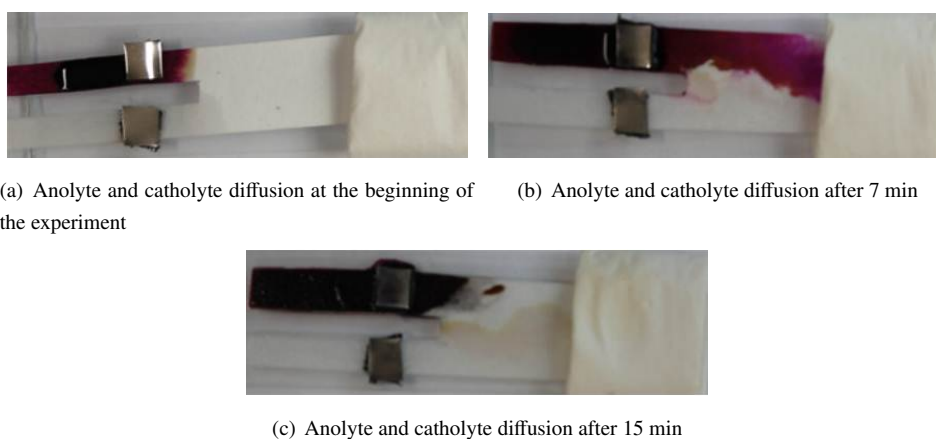
Figure 4.8: Diffusion of anolyte and catholyte at different times after the beginning pf the experiment.

4.3.4 Effect of various catalyst on cell performance

To further augment the cell performance, Cu-NPs, f-MWCNTs, and Cu-NPs@f-MWCNTs composites are used as catalysts. Depending upon the activity of the catalysts used, oxi-

dation is expected to be either a charge transfer limited process or a mass transport limited process [84]. Metallic catalysts promote the oxidation process by forming complexes with hydrazine. The stability of the complexes is determined by the charge transfer between the catalyst (metal) surface and the species in the solution (anolyte). For example, in an alkaline medium, Cu undergoes oxidation to form $Cu(OH)_2$ [84].

$$Cu + 2OH^- \rightarrow Cu(OH)_2 + 2e^-, \tag{4.4}$$
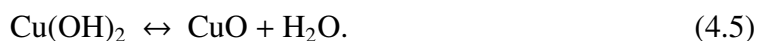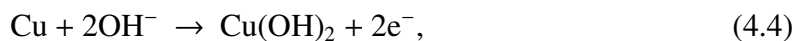
$$Cu(OH)_2 \leftrightarrow CuO + H_2O. \tag{4.5}$$

These species such as $Cu(OH)_2$, CuO are capable of bonding with N_2H_4 to form intermediates via electron/charge transfer and these reactions influence the overall oxidation process. Compared to other metal catalysts, such as Ag and Au, Cu has a lower onset potential of -0.75 V, for hydrazine oxidation [86].
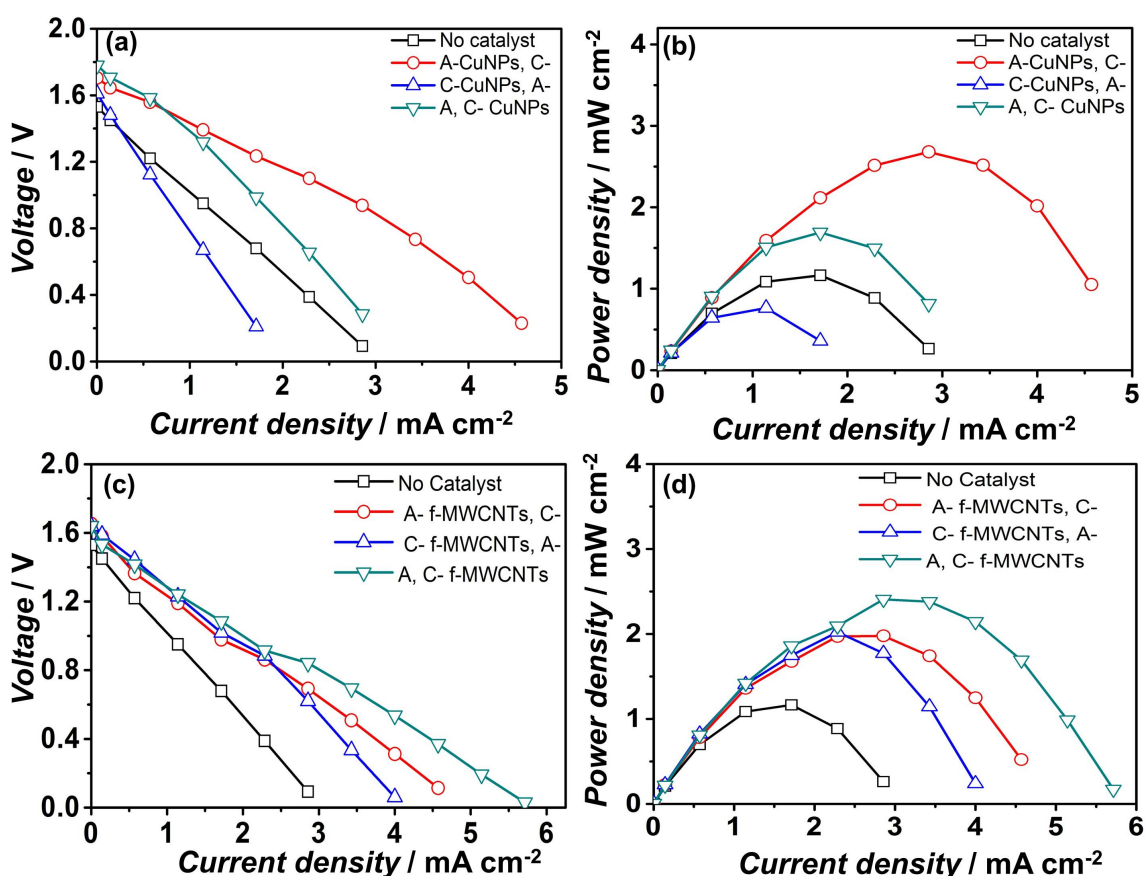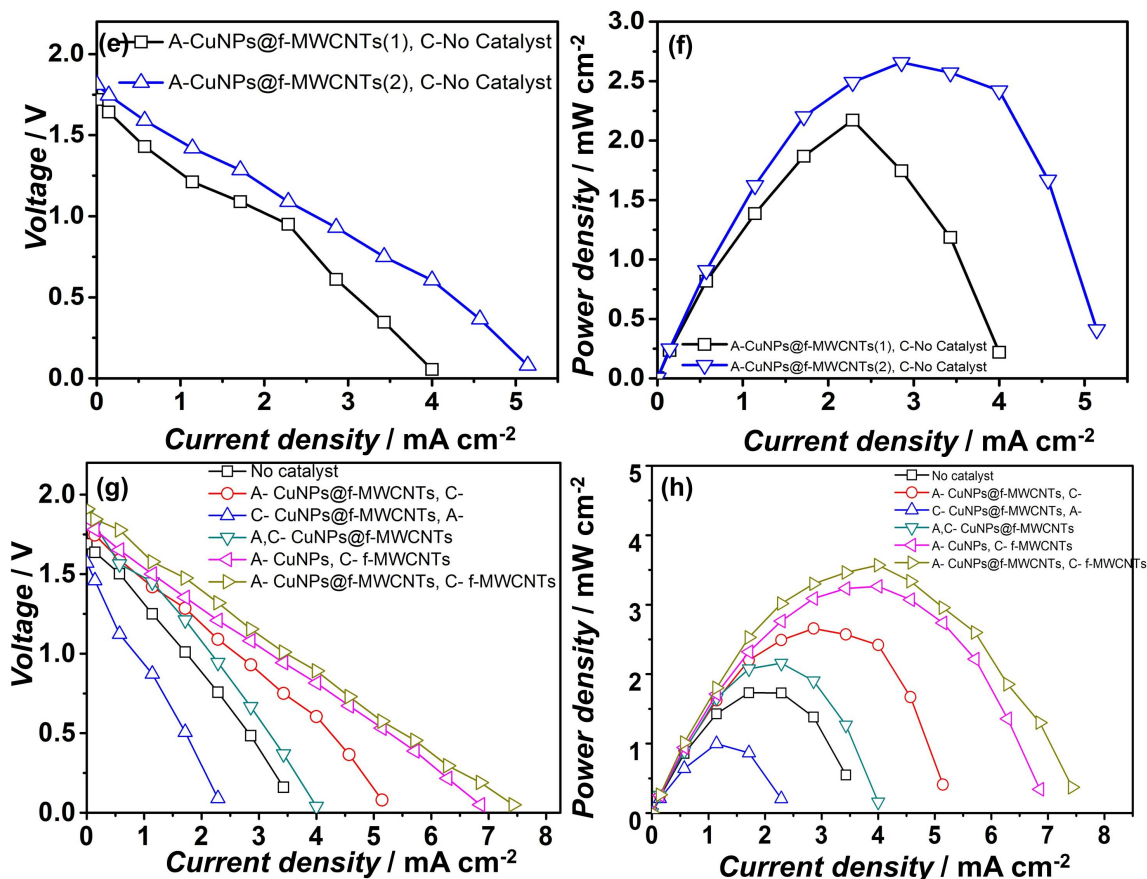
Figure 4.9: Cell performances using (a,b) Cu-NPs, (c,d) f-MWCNTs, (e,f) Cu-NPs@f-MWCNTs at different wt% of Cu-NPs and f-MWCNTs, and (g,h) Cu-NPs@f-MWCNTs composite, f-MWCNTs and Cu-NPs as catalysts in different electrode combinations at 6 M $N_2H_4.H_2O$ + 4 M NaOH as the anolyte. The catholyte is 1 M $KMnO_4$ + 4 M H_2SO_4. (a,c,e,g) show voltage versus current density and (b,d,f,h) show power density versus current density curves. A- Anode is plain carbon cloth, C- Cathode is plain carbon cloth and no catalyst implies that anode and cathode are plain carbon cloths. In (e,f) the wt% of Cu-NPs to f-MWCNTs is 1.2:1 in (1) and 3:1 in (2).

Fig. 4.9(a) and (b) show the cell performance using Cu-NPs. The role of the Cu-NPs is investigated by loading it at both and at either of the two electrodes. Since H_2SO_4 is used in the catholyte, the cell under-performs whenever the catalyst is used at the cathode. Cu reacts easily with H_2SO_4, leading to unwanted reactions and this decreases the cell performance. Using Cu-NPs only at the anode gave a maximum power density of 2.68 mW cm^{-2} at an operating voltage of 0.93 V, implying that Cu-NPs favor the oxidation of hydrazine at the anode more than the reduction of $KMnO_4$ at the cathode. The electrochemical activity of f-MWCNTs is also investigated in a similar way. Functionalization of MWCNTs is important because non-functionalized MWCNTs are hydrophobic and secondly, they tend to

aggregate by the virtue of van der Waals forces, which leads to interaction of the particles in the vicinity of each other. This reduces the effective surface area and limits their activity. Functional groups such as -COOH or -OH limits the interaction between the particles and makes the MWCNT hydrophilic. Moreover, MWCNTs are inert towards H_2SO_4 and can be considered as a continuous chain of carbon atoms linked together; thus giving rise to a 1-D structure. In this case it is easier for a mobile electron to jump from one atom to the neighboring atom, thereby facilitating the electron transport. When f-MWCNTs are used at both the electrodes, it leads to a relative increase of 42% in peak power density compared to the use of Cu-NPs at both the electrodes. The use of Cu-NPs at the anode alone gives better performance as compared to its use at both the electrodes.

Table 4.1: Performance comparison of different anode and cathode combinations studied.

Sl. No	Anode	Cathode	Peak P (mW/cm^2)
1	No catalyst	No catalyst	1.16
2	CuNPs	No catalyst	2.67
3	f-MWCNTs	No catalyst	1.98
4	Cu-NPs@f-MWCNTs	No catalyst	2.63
5	No catalyst	CuNPs	0.76
6	CuNPs	CuNPs	1.69
7	No catalyst	f-MWCNTs	2.02
8	f-MWCNTs	f-MWCNTs	2.40
9	CuNPs	f-MWCNTs	3.25
10	Cu-NPs@f-MWCNTs	f-MWCNTs	3.58
11	No catalyst	Cu-NPs@f-MWCNTs	0.99
12	Cu-NPs@f-MWCNTs	Cu-NPs@f-MWCNTs	2.16

The use of f-MWCNTs in all cases leads to similar performance, although slightly better when used at both the electrodes. Its use at the cathode alone leads to much better performance compared to the use of Cu-NPs at the cathode alone (refer Fig. 4.9 (c) and 4.9 (d)). This leads to the conclusion that Cu-NPs act as good electro-catalyst for hydrazine oxidation and f-MWCNTs act as good electro-catalyst for $KMnO_4$ reduction. Therefore, an even better performance can be achieved by using Cu-NPs at the anode and f-MWCNTs at the cathode. A combination of Cu-NPs at the anode and f-MWCNTs at the cathode leads to 92% and 35% increase in the power densities compared to the sole use of Cu-NPs (Fig. 4.9(b)) and sole f-MWCNTs (Fig. 4.9 (d)) respectively, at both electrodes. The Cu-NPs@f-MWCNTs composite also offers promising cell performance. The structure of the composite shows a mixed morphology of aggregates of Cu-NPs attached to the f-MWCNTs. To decide on the wt% of Cu-NPs and f-MWCNTs in the composite, experiments are performed using two different compositions on the anode and the results are

shown in Fig. 4.9(e) and Fig. 4.9(f). Blank carbon cloth is used as the cathode. The wt% of Cu and f-MWCNTs in the composites is estimated by TGA, and it is deduced that in one case the composite is composed of 75% of Cu and in the other case 45%. The composite having higher Cu content lead to slightly better performance compared to the one with lower Cu content. The synergistic effect between the two increases the effective surface area for the electrochemical reactions and also assists in better conductivity of electrons.

Fig. 4.9(g) and (h) shows the performance of the cell using Cu-NPs@f-MWCNTs composite. Using the composite catalyst at both electrodes resulted in a cell performance, which is lower than that of the cell with only Cu-NPs at the anode (Fig. 4.9(a) and (b)). However, when the composite at the cathode is replaced with only f-MWCNTs, the cell delivered the best performance, of all combinations studied. This cell produces a power density 3.58 mW cm^{-2} at 0.89 V. Table 4.1 shows a performance comparison of different anode and cathode combinations studied in the present work.

4.3.5 Cyclic voltametry studies of catalysts

To understand the electrochemical oxidation of hydrazine at the anode, cyclic voltammograms are recorded with electrodes based on f-MWCNTs, Cu-NPs, and Cu-NPs@f-MWCNTs as working electrodes in an alkaline solutions of $N_2H_4 \cdot H_2O$, with Pt as counter electrode and Ag/AgCl/KCl as the reference electrode. The results are shown in Fig. 4.10.
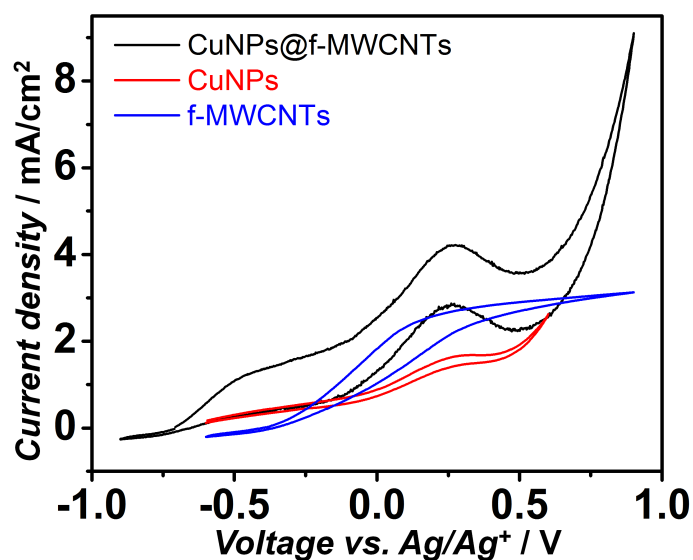
Figure 4.10: Cyclic voltammograms showing oxidation of a solution of 6 M $N_2H_4.H_2O$ in 4 M NaOH using Cu-NPs, f-MWCNTs, and Cu-NPs@f-MWCNTs composite, as the working electrodes, Ag/AgCl/KCl as the reference electrode and a Pt rod as the counter electrode.

For the f-MWCNTs there is no well-defined oxidation peak at any voltage. However, a

very broad peak is visible around 0.2 - 0.3 V (vs Ag/Ag$^+$). This indicates that f-MWCNTs have a mild catalytic activity towards hydrazine. This can also be justified from the polarization curves (Fig. 4.9d), where the peak power density increases from 1.16 (without any catalyst) to 1.98 mW cm^{-2}. For Cu-NPs, the oxidation peak at $\approx$ 0.32 V is relatively well-defined as compared to f-MWCNTs and hence they have a better catalytic activity towards hydrazine oxidation. The oxidation peak position matches well with a previously reported value of 0.26 V (versus Ag/Ag$^+$) for hydrazine oxidation at a Cu electrode [84]. With Cu-NPs, the peak power density increases to 2.67 mW cm^{-2}. In the case of Cu-NPs@f-MWCNTs, two peaks appearing in the voltammograms of hydrazine oxidation can be attributed to two different charge/electron transfer processes comprising of (i) oxidation of Cu to Cu(OH)$_2$ (further to CuO) in alkaline medium and (ii) oxidation of hydrazine in the presence of these intermediates. The pre-peak is more prominent in case of the Cu-NPs@f-MWCNTs composite, possibly because of the better morphology of Cu-NPs on the f-MWCNTs (less aggregation). Another possibility for the emergence of the pre-peak could be due to the capacitive current arising as a result of the capacitive nature of the f-MWCNTs. The oxidation peak is observed at 0.27 V (versus Ag/Ag$^+$), which is prominent and sharp as compared to f-MWCNTs and Cu-NPs. The peak power density for this case is 2.63 mW cm^{-2} and it is comparable to that of Cu-NPs. The above results indicate that Cu-NPs and Cu-NPs@f-MWCNTs show good electrocatalytic activity towards hydrazine oxidation at the anode.

The cyclic voltammogram of Cu-NPs in 4 M NaOH is shown below in Fig. 4.11. The figure shows a featureless voltammogram with no specific oxidation/reduction peak in the absence of hydrazine.
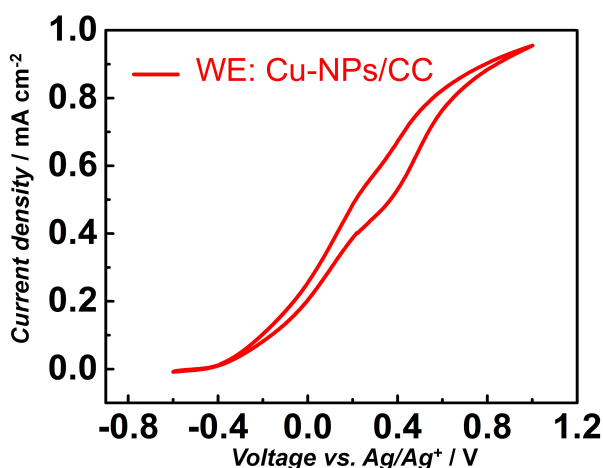
Figure 4.11: Cyclic voltammograms showing response of Cu-NPs as the working electrodes in 4 M NaOH. Ag/AgCl/KCl is the reference electrode and a Pt rod is the counter electrode. Scan rate is 20 mV/s.

4.3.6 Electrochemical impedance spectra measurements

The electrochemical impedance spectra recorded at 0.9 V are shown in Fig. 4.13. The frequency is scanned from 1 MHz to 0.1 Hz with an amplitude of 10 mV. The only variable in the experiments is the concentration of $N_2H_4.H_2O$ (fuel) in the anolyte, and for each anolyte concentration, the experiment is repeated four times, each time using a newly constructed cell.
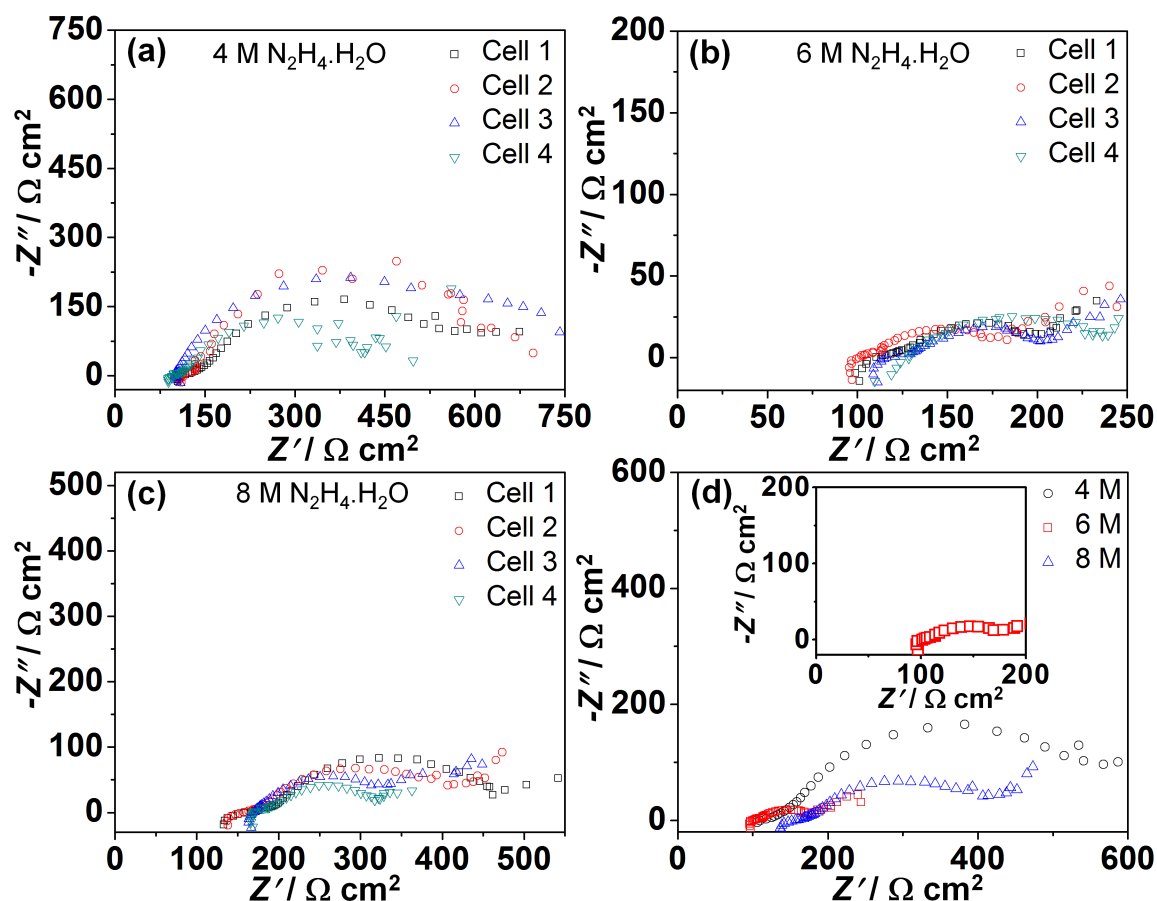
Figure 4.12: Electrochemical impedance spectra (EIS) recorded at 0.9 V with an ac voltage amplitude of 10 mV for 4 fresh cells at (a) 4 M (b) 6 M (c) 8 M $N_2H_4.H_2O$ concentrations with 4 M NaOH in each case, and (d) comparison of Nyquist plots for different fuel concentrations (inset image for cell at 6 M $N_2H_4.H_2O$). Cu-NPs@f-MWCNTs-carbon cloth is used at the anode and f-MWCNTs-carbon cloth is used at the cathode. The catholyte is a mixture of 1 M $KMnO_4$ and 4 M H_2SO_4.

Fig. 4.13 shows that even under the same experimental conditions, there is a significant variation in the spectra, particularly at 4 M concentration. Ideally, the impedance spectra must be recorded at steady state conditions. However, performance degradation of the cell (discussed in the later section) does not allow recording of the spectra at steady state conditions, and the data at low frequency becomes scattered. There are also other uncer-

tainties associated with the experiment such as the anisotropy of the paper, which may lead to different diffusion rates from cell to cell. Nevertheless, the high frequency intercept of the Nyquist plots give some indication about the Ohmic resistance offered by the system. Nothing much can be concluded on the polarization resistance because of the distortion of data at low frequency. It appears from the trend of Nyquist plot that the polarization resistance is lower at 6 M compared to 4 M and 8 M fuel concentrations in the anolyte. Although the electrolyte concentration (NaOH and H_2SO_4) are maintained constant at the anode and the cathode, the Ohmic resistance increases with increase in $N_2H_4.H_2O$ concentration. The complete data set is shown in Table 4.2 along with the standard error (defined as $\sigma/\sqrt{n}$, where σ is the standard deviation in the Ohmic resistance obtained for $n = 4$).

Table 4.2: Ohmic resistance and its standard error for different cells obtained from the impedance analysis.

Fuel concentration in anolyte	$R_{ohm}(\Omega\text{-cm}^2)$					Standard Error %
	Cell-1	Cell-2	Cell-3	Cell-4	Average	
4 M	117.8	111.2	101.3	97.8	107.1	4.57
6 M	110.6	101.1	116.3	128.8	114.2	5.78
8 M	165.8	157.1	170.2	169.4	165.6	3.0

To cross-verify the trend in the Ohmic resistance observed in the Nyquist plots, we have performed, current interruption method. The current interruption method also resulted in the same trend in Ohmic resistance, i.e., resistance increases with increase in the fuel ($N_2H_4.H_2O$) concentration in the anolyte and the results are shown in Table 4.3.

Table 4.3: Ohmic resistance and its standard error for different cells obtained form the current interrupt method.

Fuel concentration in anolyte	$R_{ohm}(\Omega\text{-cm}^2)$					Standard Error %
	Cell-1	Cell-2	Cell-3	Cell-4	Average	
4 M	102.5	123.2	80.8	79.4	96.5	10.3
6 M	124.3	120.8	133.3	144.5	130.7	5.2
8 M	152.6	157.5	137.5	147.0	148.6	4.2

These two methods give the Ohmic resistance of the working cell, however they do not aid in identifying the source of increase in resistance. Since the only variable is the concentration of $N_2H_4.H_2O$, it should be anticipated that the increase in resistance is due to the decrease in conductivity of the anolyte with increase in concentration of $N_2H_4.H_2O$. To verify this hypothesis, we have measured the resistance of the anolyte and catholyte by using three electrode configuration. Ag/AgCl/KCl is is used as the reference electrode, Pt is used as the counter electrode and FTO plate as the working electrode. The three electrode system is placed in the solution of the anolyte or catholyte, and impedance anaysis is performed to obtain the Ohmic resistance. The results obtained are shown in Table 4.4.

Table 4.4: Ohmic resistance of the anolyte and the catholyte.

Medium	R_{ohm} (Ω-cm^2)
NaOH (4 M)	104.4
NaOH (4 M) + $N_2H_4.H_2O$ (4 M)	340.3
NaOH (4 M) + $N_2H_4.H_2O$ (6 M)	354.2
NaOH (4 M) + $N_2H_4.H_2O$ (8 M)	377.2
$KMnO_4$ (1 M) + H_2SO_4 (4 M)	99.0

Clearly, the resistance of the anolyte increases with increase in the concentration of $N_2H_4.H_2O$. This indicates that the increase in Ohmic resistance observed in the Nyquist plot (Fig. 4.13) is due to the decrease in the ionic conductivity of the anolyte on increasing the $N_2H_4.H_2O$ concentration.

The equivalent circuit for all the impedance plots shown in this chapter is same as shown in Fig. 3.16. The hydrazine monohydrate paper cell system discussed in this chapter is also represented by the half Randles circuit, because of the reasons as discussed in section 3.3.3. The comparison between the experimental and simulated data, for the hydrazine monohydrate paper cells, are shown in Fig. 4.13. The simulated values show good agreement with the experimental ones.
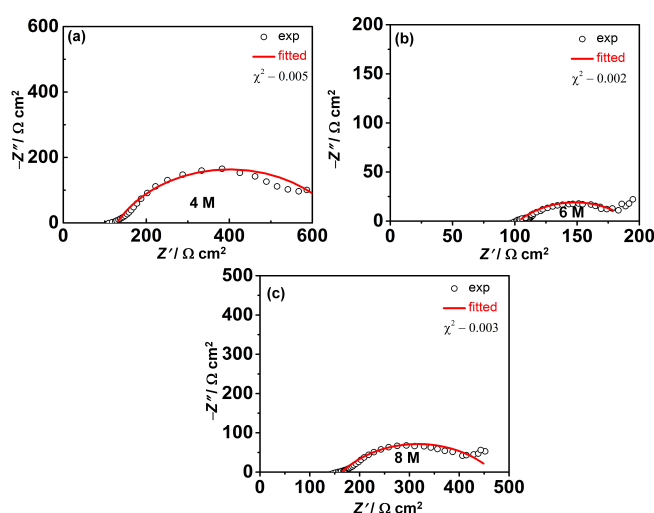
Figure 4.13: Electrochemical impedance spectra (EIS) recorded at 0.9 V with an ac voltage amplitude of 10 mV (a) 4 M (b) 6 M (c) 8 M $N_2H_4.H_2O$ concentrations with 4 M NaOH in each case. Cu-NPs@f-MWCNTs-carbon cloth is used at the anode and f-MWCNTs-carbon cloth is used at the cathode. The catholyte is a mixture of 1 M $KMnO_4$ and 4 M H_2SO_4. Experimental data is represented by open symbols. Lines represent fitted/simulated results.

4.3.7 Stability of cell performance

Although the filter paper can self transport the anolyte and catholyte from their reservoirs, in our experiments, the reaction is initiated by discharging 3-4 drops each of the anolyte and the catholyte near the respective electrodes. While a large portion of the fuel and the oxidant is absorbed by the filter paper, a relatively small portion participates in the electrochemical reactions. Once these are consumed, the cell current density declines. However, as shown in Fig. 4.14(a), the current density can be recovered nearly to its initial value by replenishing the cell with fresh drops of the anolyte and the catholyte. There are several reasons for the drop in cell current with time, such as anolyte and catholyte cross over, dilution effect due to the reaction products etc. Fig. 4.14(b) shows the decay of open circuit voltage as a function of time. The aforementioned effects are also responsible for the decrease in OCV over time. Since the decrease in OCV observed over a period of nearly 11 minutes occurs by only 0.1 V (Fig. 4.14(b)) and since the current density after decay, is restored to its original value upon fuel and oxidant replenishment, it is obvious that this cell is suitable for providing stable electrical power input for a short duration of time for low power consuming devices.
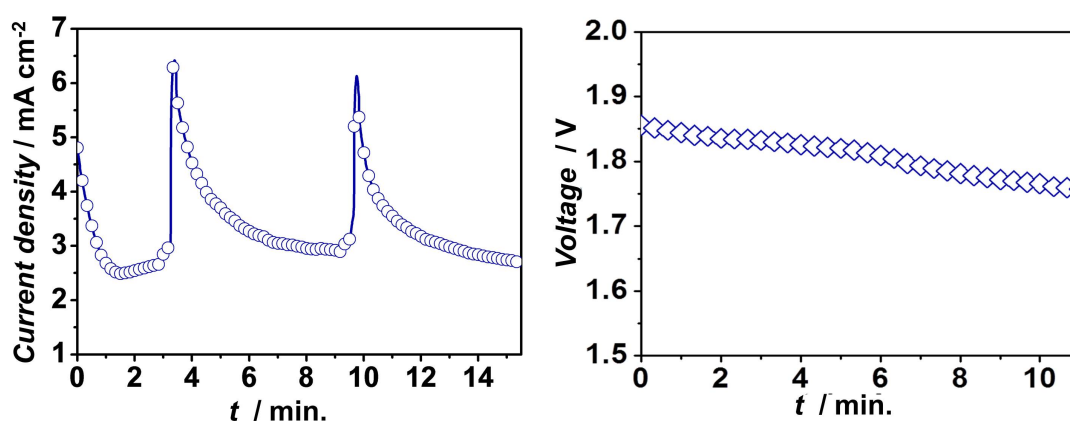
Figure 4.14: Stability of cell performance: (a) regeneration of current density (at ~ 0.9 V), and (b) chronopotentiometry (at 1 μA). Cu-NPs@f-MWCNTs on carbon cloth is used at the anode and f-MWCNTs is used at the cathode. The anolyte is a mixture of 6 M $N_2H_4.H_2O$ and 4 M NaOH, and the catholyte is a mixture of 1 M $KMnO_4$ and 4 M H_2SO_4.

4.4 Concluding remarks

Paper based fuel cells operating at room temperature are developed with $N_2H_4 \cdot H_2O$ as the fuel and $KMnO_4$ as the oxidant. Carbon cloth and carbon cloth loaded with the following catalysts: Cu-NPs, f-MWCNTs and a Cu-NPs@f-MWCNTs composite are used as the

electrodes. Cu-NPs are having particle sizes in the range of 8-30 nm and the Cu-NPs@f-MWCNTs composite consists of Cu-NPs tethered to the fibrillar structures of f-MWCNTs. Among all the cells studied by varying catalyst combinations at the cathode and the anode, the best cell performance is obtained with Cu-NPs@f-MWCNTs at the anode and with f-MWCNTs at the cathode. The cell delivered a maximum power density of 3.58 mW/cm^2 at 0.89 V. In this configuration, the synergistic effects of the two materials, (i) the high electrocatalytic activity of Cu-NPs towards hydrazine monohydrate, and their stability in an alkaline medium (at the anode), and (ii) the high effective surface area (that allows high loading of electrochemically accessible Cu-NPs) and the good electronic conductivity of f-MWCNTs, and their stability in both alkaline and acidic media (at anode and cathode), came to the fore, manifesting in the best fuel cell performance. Electrochemical impedance analysis of the cells also showed the least Ohmic resistances for the 4 M case, compared to other fuel concentrations. This cell with Cu-NPs@f-MWCNTs at the anode and f-MWCNTs at the cathode, delivered (i) an almost invariant OCV, for over 10 minutes of operation, and (ii) a current density that restored to its original magnitude of c.a. 4.5 mA/cm^2 from a decayed value, upon replenishing the fuel and oxidant (at 0.9 V). The combination of low cost Cu and carbon nanotubes based catalysts, filter paper based scaffolds for the flow of fluids, and carbon cloth as the electrodes applied to this cell, clearly demonstrates the potential of this fuel cell for applications in systems that require power for short duration.

Chapter 5

Methanol-based fuel cell on paper support with N-doped graphene/nickel cobaltite composite catalyst

5.1   Introduction

Chapter 3 presented a formic acid fuel cell and Chapter 4 presented a hydrazine fuel cell. Compared to formic acid fuel cell, a power density increment of 3 mW cm^{-2} is achieved by switching to a redox couple that uses hydrazine. Furthermore, Cu based catalysts are used in the case of hydrazine to achieve significant improvement in cell performance. One of the objectives of the present work is the development of paper base fuel cell that can deliver power densities sufficient enough for practical applications. Therefore, this Chapter describes the development of methanol based fuel cell and the redox couple chosen has a standard cell potential of 2.32 V, which is higher than the formic acid based redox couple presented in Chapter 3 and lower than hydrazine based redox couple presented in Chapter 4.

In this chapter, we have also observed the strong dependence of the cell performance on the cell architecture. In the last two chapters, the cell performances have been investigated with a membraneless U-shaped cell configuration. Similarly, the cell performance with methanol as the fuel in the same configuration is studied. However, the performance obtained in this cell was not promising. This lead us towards the development of a T-shaped cell architecture architecture, as shown in Fig. 5.1. The motivation behind this is to limit the methanol cross over by separating the paper strips and placing a gel in between, which conjoins the paper strips. As a result of this, the same redox couple could deliver a power a density ≈ 3 times higher than the membraneless cell, under the same operating conditions. Based on these findings, the T-shaped cell is used throughout all the studies in this and the

next chapter.

The OCV obtained in this cell is comparable to that of formic acid cell. Although the OCV is lower than hydrazine, the catalysts employed and the electrode kinetics led to a performance, which is better than hydrazine cell. Thus a higher OCV does not guarantee better cell performance. Similar to the case of formic acid and hydrazine $KMnO_4$ is used as the oxidant.

Methanol has a volumteric energy density of $4.69\,kWh\,l^{-1}$ [63], which is higher than that of liquid hydrogen and are good sources of hydrogen. Also methanol is cheap, easy to handle and store, available in plenty and can be renewed from wood alcohol [70]. With methanol-permanganate fuel oxidant pair and appropriate electrocatalyst, the power density of the cell further increases to $4.67\,mW\,cm^{-2}$. In addition the experimental characterization, the cell performance is simulated by using a Butler-Volmer type kinetics. The usability of the cell for practical applications is demonstrated by lighting a 3mm LED. The performance of the paper supported methanol fuel cell is studied by various electrochemical methods, such as chronoamperometry, chronopotentiometry and electrochemical impedance spectroscopy (EIS). The oxidation of methanol occurs at anode according to the following reaction

$$CH_3OH + 6\,OH^- \rightleftharpoons CO_2 + 5\,H_2O + 6\,e^-, \quad E^0 = -0.81\ V, \tag{5.1}$$
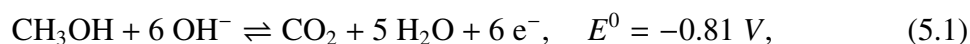
and the reduction of $KMnO_4$ takes place at the cathode according to the following reaction

$$MnO_4{}^- + 8\,H^+ + 5\,e^- \rightleftharpoons Mn^{2+} + 4\,H_2O, \quad E^0 = 1.51\ V. \tag{5.2}$$

The overall cell reaction is given by

$$5\,CH_3OH + 6\,MnO_4{}^- + 18\,H^+ \rightleftharpoons 5\,CO_2 + 19\,H_2O + 6\,Mn^{2+}. \tag{5.3}$$
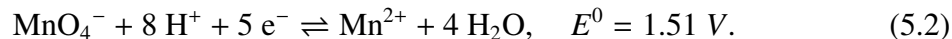
The standard potential for the overall cell reaction is 2.32 V.

5.2 Experimental

5.2.1 Chemicals

Methanol (CH_3OH), graphite powder, toluene ($C_6H_5CH_3$), nickel nitrate hexahydrate ($Ni(NO_3)_2.6H_2O$), cobalt nitrate hexahydrate ($Co(NO_3)_2.6H_2O$), isopropyl alcohol (IPA) and ammonium persulphate (($NH_4)_2S_2O_8$) were purchased from Sigma Aldrich. Potassium permanganate ($KMnO_4$), melamine ($C_3H_6N_6$), acrylamide and sodium hydroxide (NaOH) were purchased from Merck. Sulfuric acid (H_2SO_4) was purchased from Fischer Scientific. Whatman filter paper (ashless 40) was used as the paper support. Ultrapure water of resis-

tivity 18.2 MΩ cm, was acquired from a Millipore direct Q3UV system. All the reagents used in this study were of analytical grade and were used as received.

5.2.2 Characterization techniques

The electrochemical measurements of the cells, i.e., chronoamperometry (I vs t), chronopotentiometry (V vs t), electrochemical impedance spectroscopy and cyclic voltametry, were done using Autolab PGSTAT 302N with a frequency response analyzer and NOVA 1.11 software integrated with it. The structure and morphology of the as-prepared $NiCo_2O_4$ catalysts were studied using a Zeiss scanning electron microscope (SEM) by obtaining the micrographs for the catalysts. The X-ray powder diffraction is carried out using PANalytical XPertPRO instrument with Cu-K$_\alpha$(λ= 1.5406 Å). The composition of the composite was estimated using thermogravimetric analysis, Pyris1 TGA, PerkinElmer, under helium atmosphere, at a temperature ramp of 10 °C/min.

5.2.3 Cell assembly

The cell was assembled by placing two L-shaped paper strips at a distance of 0.2 cm with polyacryl amide (PAM) gel impregnated with H_2SO_4 placed in between the strips. The gel acts as a proton exchange membrane for transport of ions. The anolyte and catholyte were discharged on the short arm, each measuring 0.5 cm × 2.5 cm, as indicated in schematic shown in Fig. 5.1.
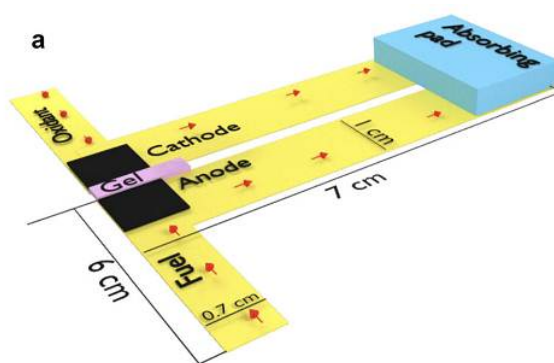
Figure 5.1: Schematic of T-shaped methanol fuel cell supported on paper.

The short arm serves as the inlet, while long arm measuring, 8 cm × 0.5 cm, serves as the outlet for the products and excess and leftover reactants. The concentration of CH_3OH was varied from 2 M to 4 M to 6 M, in the anolyte containing 4 M NaOH (electrolyte). The concentration of the catholyte was kept constant at 1 M $KMnO_4$ and 4 M H_2SO_4. Carbon cloth was cut into 0.5 cm × 0.5 cm and served as the electrodes, and steel plates were used

as the current collectors. The PAM gel was placed between the electrodes, such that it is in contact with both anode and cathode. An absorbent pad was placed at the end of the long strip to absorb the downstream flow which contains the unreacted fuel, oxidant and the reaction products. The whole cell assembly was placed on a glass slide.

5.2.4 Preparation of PAM/H$^+$ gel

2 grams of acrylamide were dissolved in 10 mL of DI water and the resulting solution was stirred at 500 rpm at 90 °C for 10 minutes, until the solution became completely homogeneous. 6 mg of ammonium persulphate was added to the above solution and continuously stirred for 30 minutes. Ammonium persulphate provides the free radicals for the preparation of the polyelectrolyte and initiates the polymerization reaction. Once the solution was sufficiently viscous, the stirring was stopped and it was left to cool to room temperature. 2M H_2SO_4 was added to the viscous solution, which was then left at room temperature for 4-5 hours. The H_2SO_4 gets attached to the polymer chain of acrylamide by hydrogen bonding and H^+ ion acts as the mobile ion within the polymeric network, giving rise to a combination of ions and polymer chain, known as polyelectroyte membrane/gel. This final product was PAM gel and serves as the medium of transport for the ions between the electrodes.

5.2.5 NiCo$_2$O$_4$ (NCo) microspheres

The hydrothermal synthesis of ultrathin nano-sheet flower like micro-spheres of $NiCo_2O_4$ was done according to the procedure described elsewhere [106]. The experimental procedure for the same is briefly described here. First, 2.62 g of $Co(NO_3)_2.6H_2O$ and 1.31 g of $Ni(NO_3)_2.6H_2O$, were dissolved in 4 mL of water followed by 5 minutes of ultra-sonication. Once the aqueous solution of salts was completely homogeneous, 68 mL of isopropyl alcohol (IPA) was added to it and this was kept under continuous stirring for 1 hour using magnetic stirrer at room temperature. Afterwards, 11 mL of methanol was further added to the above solution, and the stirring was continued for another 30 minutes. Once the stirring was completed, the resulting solution was transferred into a 100 mL Teflon lined stainless steel autoclave, which was heated in a vacuum oven at 120 °C for 24 hours. The product thus obtained was a green precipitate of microspheres NiCo, which is a precursor for $NiCo_2O_4$. This precipitate was then washed with copious amounts of distilled water and ethanol, and was dried overnight at 80 °C in a hot air oven, to get rid off the excess water/moisture content. The NiCo precursor was then heated at 350 °C (for calcination) with a temperature ramp rate of 1 °C/min in a muffle furnace for two hours. The resultant product was a black colored powder of $NiCo_2O_4$ microspheres.

5.2.6 NCo@N-rGO composite

The preparations of nitrogen doped graphene oxide (N-GO) and nitrogen doped reduced graphene oxide (N-rGO) were done according to the procedure described elsewhere [108]. In this method the oxidation of graphene and its doping by nitrogen are done simultaneously. The procedure is briefly explained below. 1 g of pristine graphite powder and 0.5 g of $NaNO_3$ were added to 50 mL of H_2SO_4 (98 wt%). This acidic solution was stirred using a magnetic stirrer in an ice-bath at 0 °C. 3 g of $KMnO_4$ was added very slowly in batches of 1 g, into the above solution. $KMnO_4$ and $NaNO_3$ are the oxidizing agents, which leads to the oxidation of graphite (graphene). In order to dope nitrogen into the layers of oxidized graphene, melamine was chosen as the the source of nitrogen. 0.5 g of melamine was added in the above solution, and the mixture was stirred continuously for 12 hours at 30°C. 46 mL of hot deionized water at 90 °C was then added drop-wise into the suspended solution and the temperature was maintained at 90 °C for another 1 hour. Later, 20 mL of H_2O_2 (30 %) was added to this, followed by ultrsonication for 30 minutes. Once this procedure was completed, the suspension was centrifuged to obtain a mud-like material, which was further washed with distilled water and ethanol, to remove the impurities. Finally this was dried in an oven at 60 °C for 2 days, to obtain the final product N-GO. In order to obtain N-rGO, 400 mg of the as-prepared N-GO were dissolved in 80 mL deionized water and the resulting solution was transferred into 100 mg Teflon lined stainless steel autoclave. This was then heated at 180 °C for 6 hours in a vacuum oven. The solution thus obtained, was first centrifuged and then washed with ethanol and distilled water several times. The material thus obtained was kept for drying at 60 °C overnight. The resultant product was N-rGO.

For the synthesis of NCo@N-rGO composite, three different weights % of N-rGO (i.e., 25 mg, 75 mg and 100 mg) were taken, and added to the solution containing 1.31 g $Ni(NO_3)_2.6H_2O$ and 2.62 g $Co(NO_3)_2.6H_2O)$ in 4 mL deionized water prior to the hydrothermal synthesis, as reported by Chen et al. [106]. Thus, three different composites with varying wt% of N-rGO were obtained. These composites with increasing amount N-rGO is referred to as Composite-1, Composite-2, and Composite-3, in the discussions to follow.

5.3 Results and discussion

5.3.1 Characterization of $NiCo_2O_4$, N-GO, N-rGO, NCo@N-rGO

The structural features and morphologies of hydro-thermally synthesized $NiCo_2O_4$ (NCo) micro-spheres, N-rGO and NCo@N-rGO are studied by scanning electron microscopy

(SEM), and the relevant micro-graphs for NCo are presented in Fig. 5.2 (a)-(b). The images obtained at a lower magnification (Fig. 5.2 (a)) depict the random distribution of the flower like micro-spheres which are non-uniform in size but with fairly good dispersion. However, agglomeration of these is also observed, which could be because of increased Van-der-Waals interaction as a result of increased surface energy. At higher magnification (Fig. 5.2 (b)) the individual micro-spheres can be seen. The surface appears to be of flower like structure consisting of ultra-thin nano-sheets that are interconnected and have multiple open spaces between them, thus giving rise to a porous structure. The average size of the micro-spheres is ≈ 5 μm and the nanosheets have an average thickness of ≈ 80 nm. The micrograph of N-rGO (Fig. 5.2 (c), shows wrinkled and sheet like structure. The micrographs of NCo@N-rGO are presented in Fig. 5.2 and NCo microspeheres can be seen adhered to the surface of the N-rGO sheets. To confirm the nitrogen doping in the NCo@N-rGO composite, energy dispersive X-ray (EDX) analysis is done, as shown in Fig. 5.2(f), which reveals the presence of nitrogen along with nickel, cobalt, carbon.
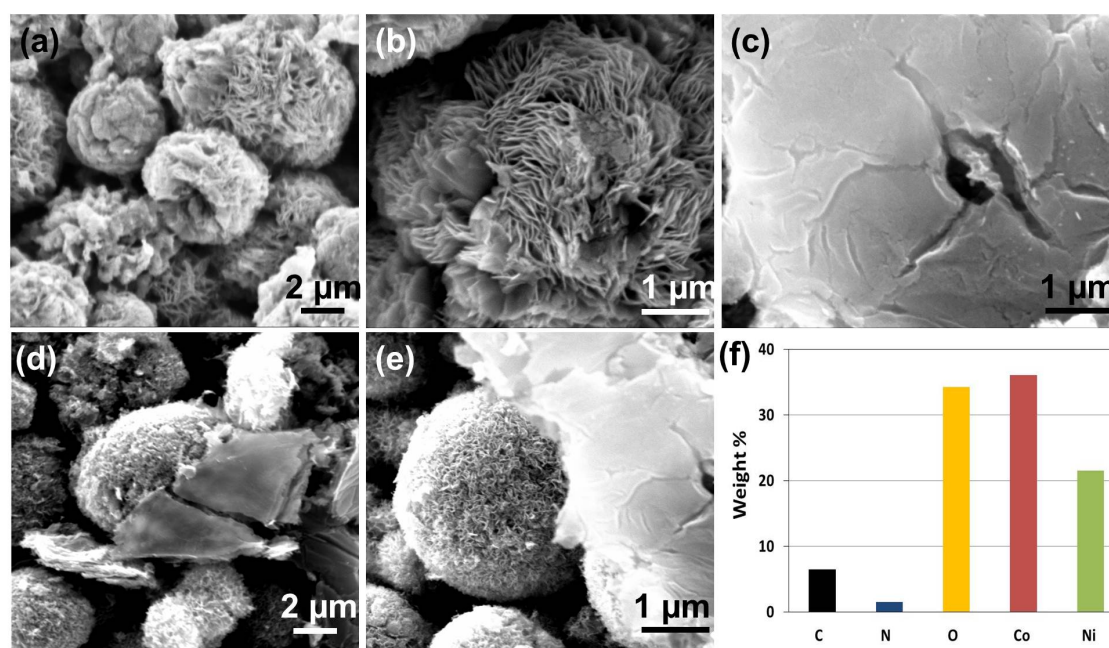
Figure 5.2: Scanning electron micrographs of (a)-(b) NiCo$_2$O$_4$ microspheres, (c) N-rGO (d) and (e) NiCo$_2$O$_4$@N-rGO (f) EDAX measurement of NiCo$_2$O$_4$@N-rGO

The HRTEM micrographs for NiCo$_2$O$_4$ (NCo) micro-spheres, N-rGO and NCo@N-rGO are shown in Fig. 5.3.
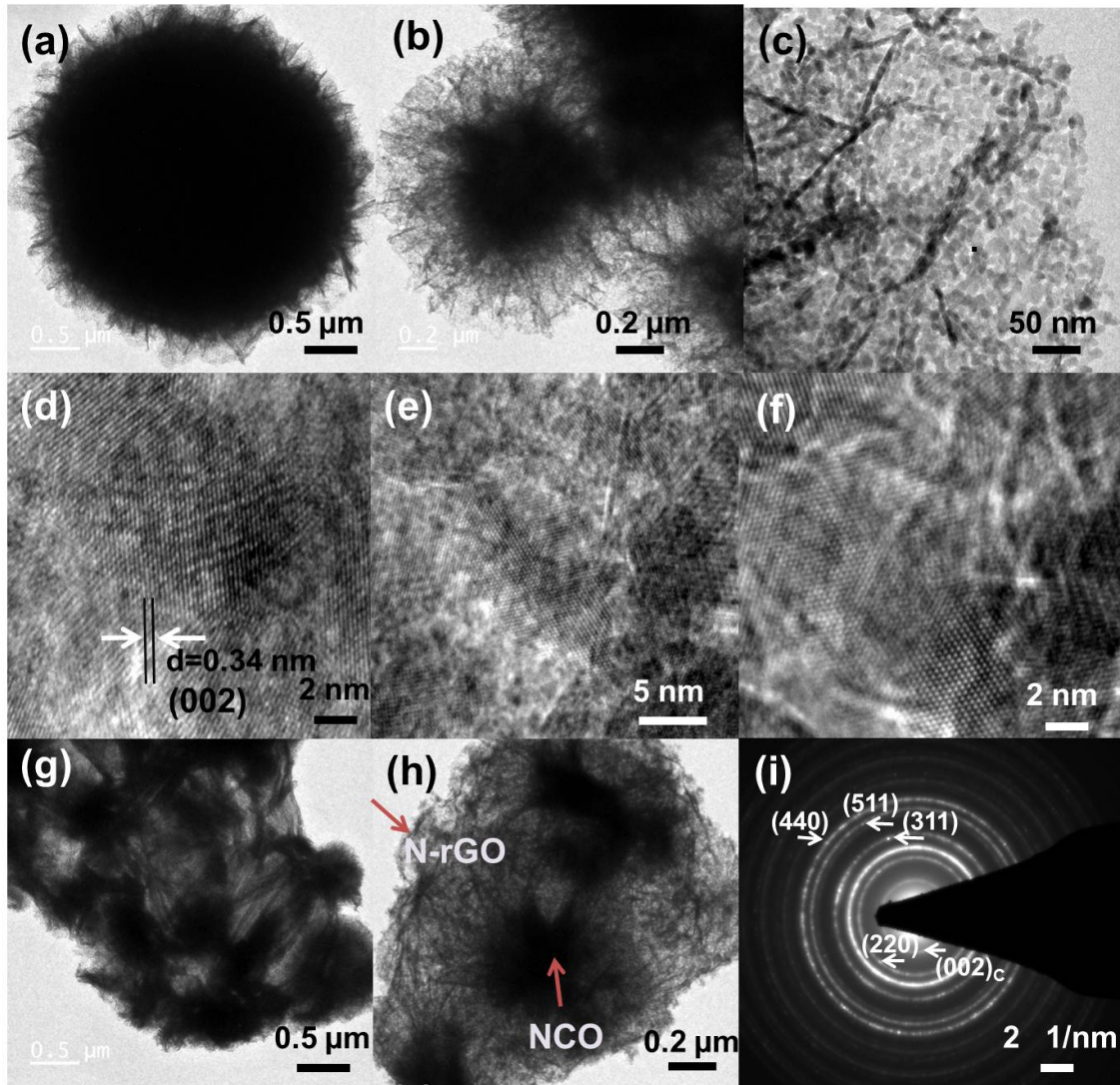
Figure 5.3: High resolution transmission electron microscopy images of (a)-(c) NiCo$_2$O$_4$ microspheres, (d)-(f) N-rGO and (g)-(i) NiCo$_2$O$_4$@N-rGO.

The micrographs of NCo (Fig. 5.3(a)-(c) show micro-spherical flower-like structure with porous surface. The surface of the NCo micro-spheres is composed of fine nanoparticles of $\approx$10.3 nm, which are interconnected with each other leading to the formation of numerous nanopores of $\approx$5-6 nm on the surface of the microspheres. The porous structure provides a better surface area. The HRTEM micrographs of N-rGO (Fig. 5.3(d)-(f)) shows a wrinkled morphology and a fringe spacing of d=0.34 nm which corresponds to the (002) plane of carbon. The micrographs of the NCo@N-rGO composite (Fig. 5.3 depict that the NCo are embedded onto the N-rGO sheets giving rise to an enhanced surface area.The selected area electron diffraction (SAED) pattern for the NCo@N-rGO composite shows well-defined bright-spotted rings, exhibiting the polycrystalline property of NCo. The bright spots in

73

the rings are indexed to (440), (511), (311) and (220) corresponding to the interplanar spacing of 0.2, 0.15, 0.24 and 0.28 nm of the NCo spinel (JCPDS no.731702). Diffuse rings are also observed in the SAED pattern of the composite, and one of these is indexed to (002), which corresponds to the interplanar spacing of 0.34 nm of graphitic carbon (JCPDS no.751621). The diffused rings of the graphitic carbon indicate its amorphous nature. Thus, the composite is a mixture of polycrytalline NCo and amorphous N-rGO.

The XRD patterns of N-rGO, N-GO, $NiCo_2O_4$ and NGO@N-rGO are presented in Fig. 5.4. It is observed that N-rGO doesn't have any well defined characteristic peak, rather a broad peak is obtained at $\theta=24.5°$, which is typical for carbon-containing materials. The XRD spectra of N-GO shows one distinct and sharp peak at $\theta=10.7°$, indicating the presence of graphene oxide. The broad peak observed at $\theta=24.5°$ is probably due to the remnant graphite which did not undergo complete oxidation during the synthesis of N-GO. The XRD pattern of $NiCo_2O_4$ exhibits six diffraction peaks at $\theta=18.9°$, $31.1°$, $36.7°$, $44.6°$, $59.1°$, and $64.9°$. These respectively correspond with the (111), (220), (311), (400), (511) and (400) planes of the 'fcc' lattice, according to the PDF no. 731702. Similar XRD spectrum is obtained for NCo@N-rGO, with no other distinct peaks possibly because of the dispersion of the crystalline $NiCo_2O_4$ on the surface of N-rGO, which may interfere with the incident X-ray beam.
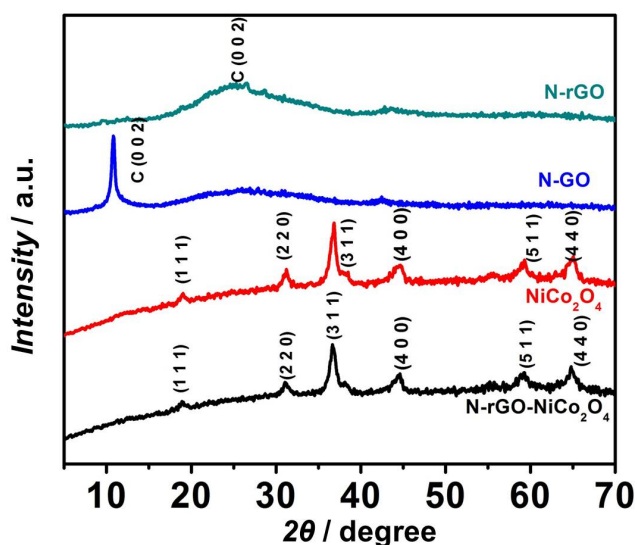
Figure 5.4: XRD-diffractograms for N-rGO, N-GO, $NiCo_2O_4$, NCo@N-rGO

The thermogravimetric analysis of the composite catalyst, NCo@N-rGO is done for varying composition of N-rGO in NCo@N-rGO. The relevant TGA traces are presented in

Fig. 5.5. As mentioned in Section. 5.2.6, three different amounts of N-rGO i.e., 25 mg, 75 mg and 100 mg, were taken for the preparation of the composite catalysts *viz* composite-1, 2 and 3. The TGA results indicate that composite 1, 2 and 3 respectively contain 6, 8 and 10 wt% of N-rGO, while rest of the catalyst contains $NiCo_2O_4$. The initial gradual weight loss is due to the removal of moisture and the drop after 600 °C corresponds to the oxidation of carbonaceous compound present in the samples.
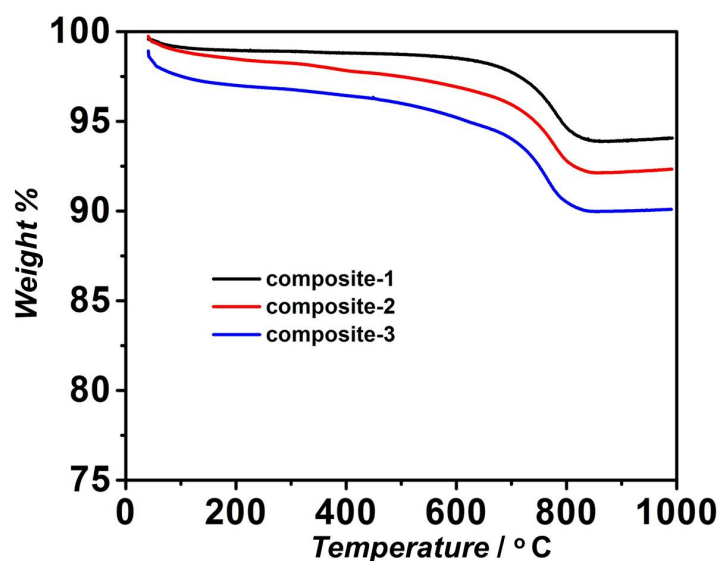
Figure 5.5: TGA curves for catalysts

Cyclic voltametry studies are carried for NCo, N-rGO and NCo@N-rGO loaded carbon cloth as the working electrode, Pt rod as the counter electrode and Hg/HgO as the reference electrode, at a scan rate of 20 mV s^{-1}. The voltage was swept back and forth. The catalyst inks were prepared by dispersing 5 mg of each catalyst in isoproponal (IPA) and drop casting them on to the electrodes. The electrodes were then left for drying until the IPA has completely evaporated. A solution of 4 M CH_3OH and 4 M NaOH serves as the working solution. The cyclic voltammograms of the catalysts are shown in Fig. 5.6. A broad shoulder emerging around 0.25 V vs Hg/HgO for N-rGO and NCo@N-rGO is due to the capacitive nature of N-rGO (carbon), while a sharp increase in the peak current for NCo at 0.25 V vs Hg/HgO could be due to the redox reactions involving Ni. Also, the NCo@N-rGO composite catalyst has maximum enclosed area across all the catalysts. Apart from this, no other relevant information can be inferred from the voltammograms about the electro-oxidation process.
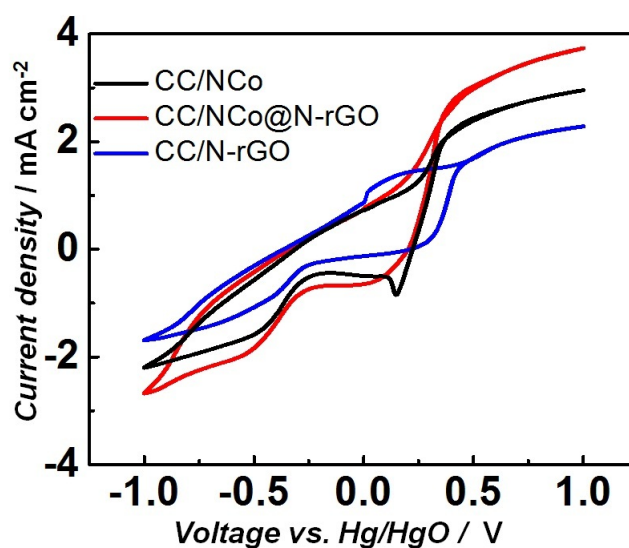
Figure 5.6: Cyclic voltammograms showing the response of NCo, N-rGO and NCo@N-rGO loaded over C-cloth as the working electrode in 4 M CH$_3$OH + 4 M NaOH. Counter electrode is Pt rod and the reference electrode is Hg/HgO and the scan rate is 20 mV/s.

5.3.2 Effect of fuel concentration on cell performance

In order to arrive at the best fuel concentration to work with U-shaped membraneless and T-shaped cells, the concentration of CH$_3$OH is varied from 2 M, 4 M, and 6 M while keeping the NaOH concentration at 4 M. The concentration of the catholyte is kept constant (1 M KMnO$_4$ and 4 M H$_2$SO$_4$). Figs. 5.7 and 5.8 show the dc-polarization curves obtained for different fuel concentrations using blank carbon cloth as electrodes at room temperature, for U-shaped and T-shaped cell, respectively. It can be seen in the Fig. 5.7, that a maximum power density of 0.35 mW cm^{-2} is obtained which is lower than the power densities attained in cells with formic acid and hydrazine hydrate, as the fuel. This drop in the cell performance is possibly because of the methanol crossover (a very well known phenomenon in direct methanol fuel cells), across all concentrations.

However, in the T-shaped cell, the best cell performance leading to a maximum power density of 0.9 mW cm^{-2} is obtained with 4 M CH$_3$OH . Whereas at 2 M and 6 M concentration of CH$_3$OH, the cell lead to inferior performance. At low concentrations, the kinetics limits the performance of the cell and at high concentration, its probably the cross over of anolyte to the cathode side that compromises the cell performance. The cross over effects are prominent in paper based fuel cells having membraneless configuration.

76
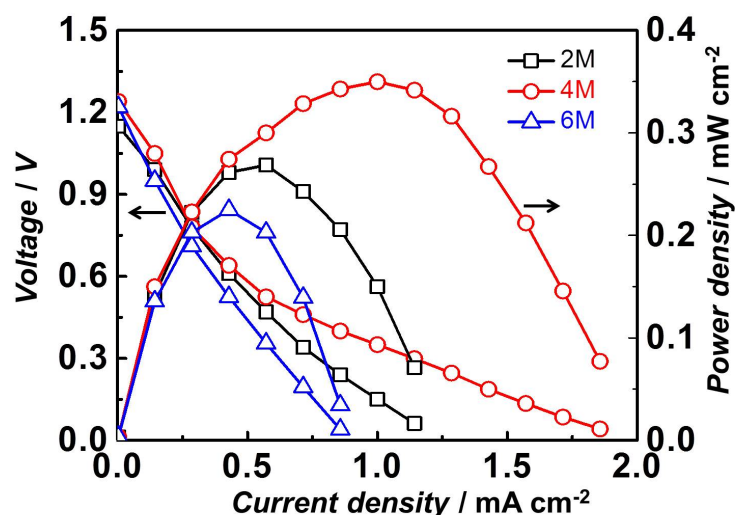
Figure 5.7: Cell performance of U-shaped cell at different fuel concentration using carbon cloth as electrodes.
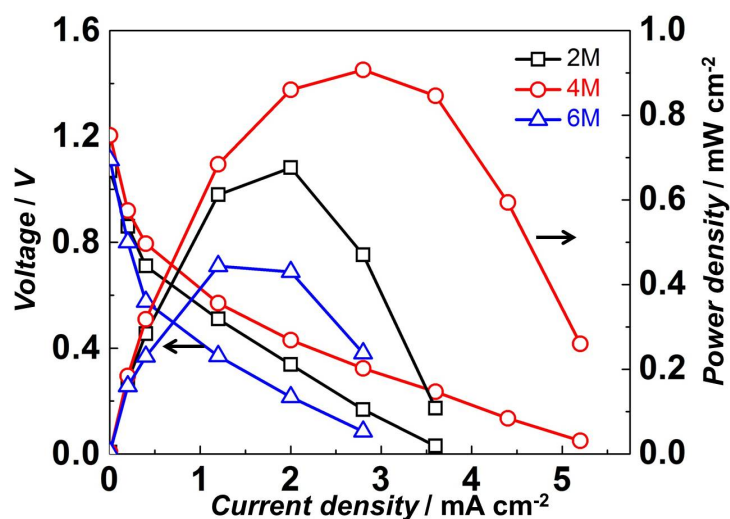
Figure 5.8: Cell performance of T-shaped cell at different fuel concentration using carbon cloth as electrodes.

The presence of PAM gel membrane in the current set up limits the diffusive transport of anolyte/catholyte to the opposite electrodes. However, even with the presence of the membrane, the cross over can not be eliminated completely. Figure 5.8 also shows the presence of significant activation losses. The cell voltage precipitously drops from the OCV of 1.2 V on polarizing the cell and this effect is present for all the concentrations studied. The high activation losses due to the slow electrochemical oxidation of CH_3OH is also reported

by several direct methanol fuel cells (DMFC) works [123, 124]. The cell is operated discontinuously by discharging a few drops of anolyte and catholyte near the electrodes. The capability of the cell to deliver power with the initial supply of the anolyte and catholyte is shown in Fig. 5.9. At an operating potential of 0.2 V, the cell current density drops from 8 mA cm^{-2} to 2.5 mA cm^{-2} over a time period of 15 mins. The cell fails to deliver any current when it is completely dried of the anolyte and/or catholyte. A completely dried out cell could still deliver a current density of 1 mA cm^{-2} on replenishing with fresh supply of anolyte and catholyte. Thus the cell will be able to deliver sustainable power on continuous supply of fuel and oxidant. Based on these studies, the anolyte concentration is fixed at 4 M CH$_3$OH in 4 M NaOH for further investigations.
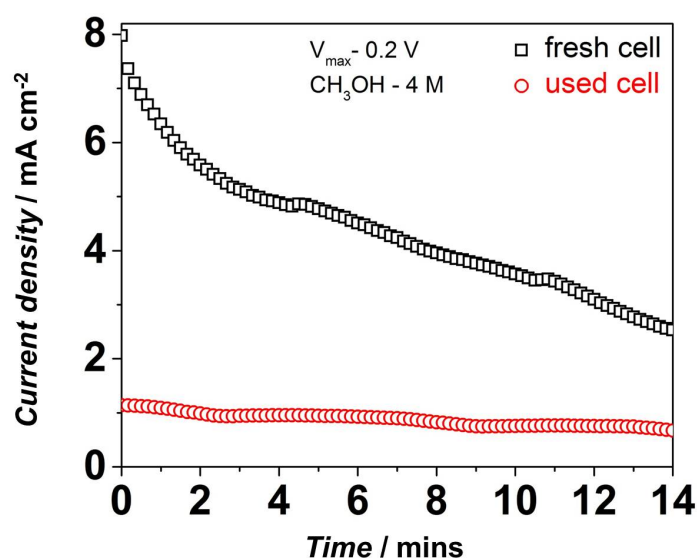
Figure 5.9: Performance of a new cell and completely dried out cell as a function of time using 4M CH$_3$OH at cell potential of 0.2 V. The dried out cell is regenerated by supplying anolyte and catholyte.

5.3.3 Effect of various catalysts on cell performance

The aforementioned cell performances obtained using plain carbon cloth as electrode material is referred to as *base case* in the discussions to follow, which focus on improving the cell performance.

Recently, the catalytic activity of different morphologies of nickel cobaltite (NiCo$_2$O$_4$, a binary metal oxide of Ni and Co) for CH$_3$OH oxidation has been studied extensively [107, 106] NiCo$_2$O$_4$ is a mixed valance oxide and in alkaline medium, it undergoes redox reactions to form NiOOH and CoOOH, and the redox couples of Ni^{2+}/ Ni^{3+} and Co^{2+}/ Co^{3+} provides rich electroactive sites, and minimizes the activation over-potentials [106]. Apart

78

from this, various carbon based supports doped with nitrogen, such as N-rGO and N-GO have been combined with $NiCo_2O_4$ to further improve its catalytic activity. Figure. 5.10 shows the cell performance with a $NiCo_2O_4$ loading of 16 mg/cm^2 either on anode, cathode or both the electrodes, and the cell leads to best performance when the catalyst is only present at the anode. The presence of $NiCo_2O_4$ only at the cathode leads to performance that is very close to the base case with significant activation losses. With the catalyst present only at the anode, the cell delivers maximum power density of 2.33 mW cm^{-2}, which is 2.5 times higher than the base case and the activation losses (as sen from the dc-polarization curve) almost disappear. This implies that $NiCo_2O_4$ can effectively enhance the methanol electro-oxidation but not the reduction of $KMnO_4$ present at the cathode (catholyte).
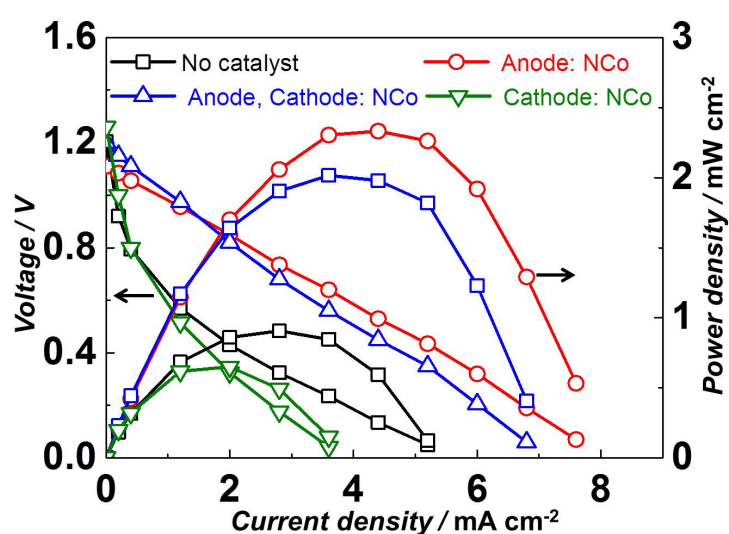
Figure 5.10: Cell performance with $NiCo_2O_4$ micro-spheres as catalyst in different electrode combinations.

At the anode $NiCo_2O_4$ undergoes redox reactions to form NiOOH and CoOOH in an alkaline medium. The corresponding redox reactions are mentioned below (5.4 and 5.5).

$$NiCo_2O_4 + OH^- + H_2O \rightleftharpoons NiOOH + 2CoOOH + 2e^- \qquad (5.4)$$

$$CoOOH + OH^- \rightleftharpoons CoO_2 + 2CoOOH + H_2O + e^- \qquad (5.5)$$
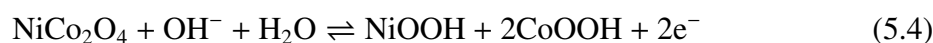
CH_3OH further reacts with NiOOH and CoOOH oxides to form the corresponding metal hydroxides $Ni(OH)_2$ and $Co(OH)_2$ in alkaline medium and liberates CO_2 [106]. The metal redox couples of Ni^{2+}/Ni^{3+} and Co^{2+}/Co^{3+} provide more active sites for the charge transfer, while the micro spheres with flower like structure enhance the catalytic surface area, thus, enhancing the methanol electro-oxidation rates. Since the presence of $NiCo_2O_4$ at the

cathode leads to low cell performance, this case is not considered for further investigation. The catalyst loading is optimized by loading different amounts of $NiCo_2O_4$ at the anode. The dc-polarization curves for different $NiCo_2O_4$ loading are shown in Fig. 5.11.
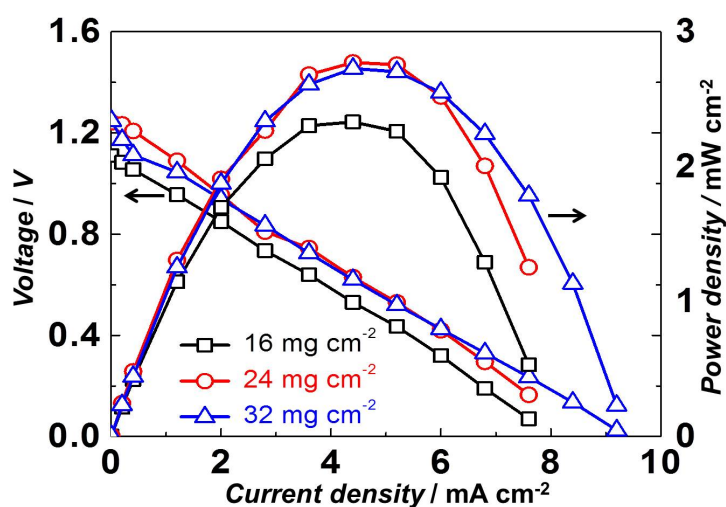
Figure 5.11: Cell performance with $NiCo_2O_4$ micro-spheres as catalyst with different loadings at the anode.

It can be seen that the cell performance increases slightly from 2.3 mW cm^{-2} to 2.77 mW m^{-2} on increasing the loading from 16 mg cm^{-2} to 24 mg cm^{-2}. With 32 mg cm^{-2} loading, no further improvement in the power density is observed. Generally, the cell performance is expected to improve with higher catalyst loading. However, an increase in catalyst loading does not lead to increased performance when the reactions become transport limited or when the products such as H_2O and CO_2 start to dilute the reactant stream as a result of slow diffusion transport away from the reaction sites or due to the agglomeration of particles at high loading. Also, at higher loading the catalytic activity of the catalysts is enhanced due to increase in the electrochemical active area. This can increase the cell performance as well as the rate of formation of products, which in turn can block the surface of the catalysts and the incoming stream of fresh solution of the anolyte/catholyte. Hence, beyond a certain loading of the catalysts no significant improvement in the cell performance is observed.

The cell performance with 24 mg cm^{-2} of N-rGO is shown in Fig. 5.12. The behavior of the cell is similar to that of $NiCo_2O_4$. The cell gives better performance with N-rGO compared to the base case, however, significant activation losses are still observed when N-rGO is present only at the cathode. $KMnO_4$ is a much stronger oxidizing agent than air, and our previous studies on other redox couples does not show the presence of significant activation losses [80, 79, 4]. Therefore, it must be inferred that the activation losses are due to the slow oxidation kinetics of CH_3OH and not because of the inability of $NiCo_2O_4$

or N-rGO to catalyse the KMnO$_4$ reduction reactions. Since both NiCo$_2$O$_3$ and N-rGO improves the cell performance when present at the anode and on both the electrodes, the cell performance is further studied by using a composite of NiCo$_2$O$_4$ and N-rGO (referred as NCo@N-rGO).
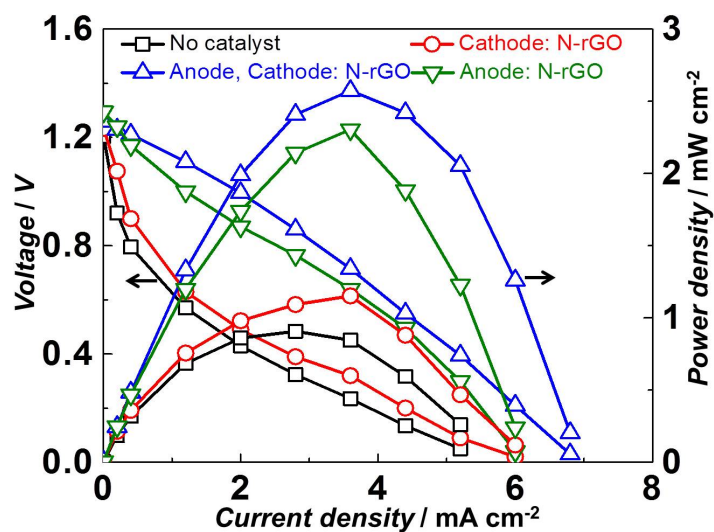
Figure 5.12: Cell performance with N-rGO as the catalyst. The anolyte contains 4M CH$_3$OH and the catholyte contains 4 M KMnO$_4$.
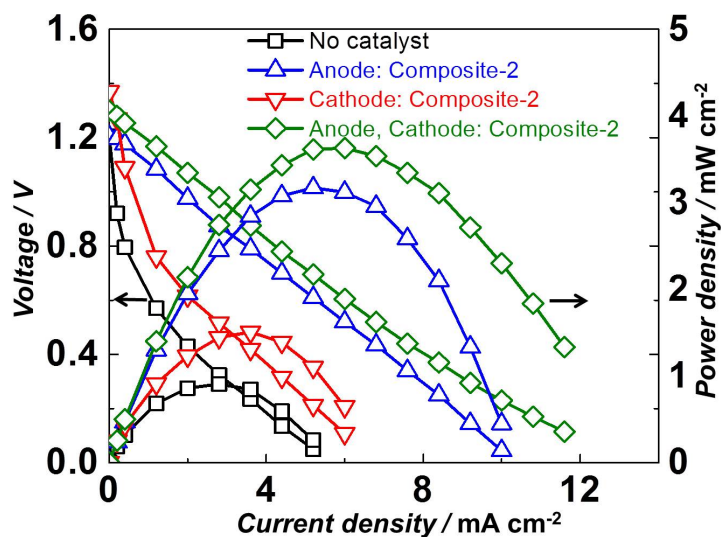
Figure 5.13: Cell performance with NCo@N-rGO (a) in different electrode combinations with composite-2.

The initial set of experiments are performed using composite-2 with loading of 16 mg cm^{-2} on the anode, cathode and then on both the electrodes. Figure 5.13 shows that similar to the case of NiCo$_2$O$_4$ and N-rGO, significant activation losses are present when the composite catalyst is not present at the anode. Since the cell gives best performance with the composite catalyst present at both the electrodes, further investigations with other wt% of N-rGO in the composite are carried out with the catalyst present on both the electrodes.
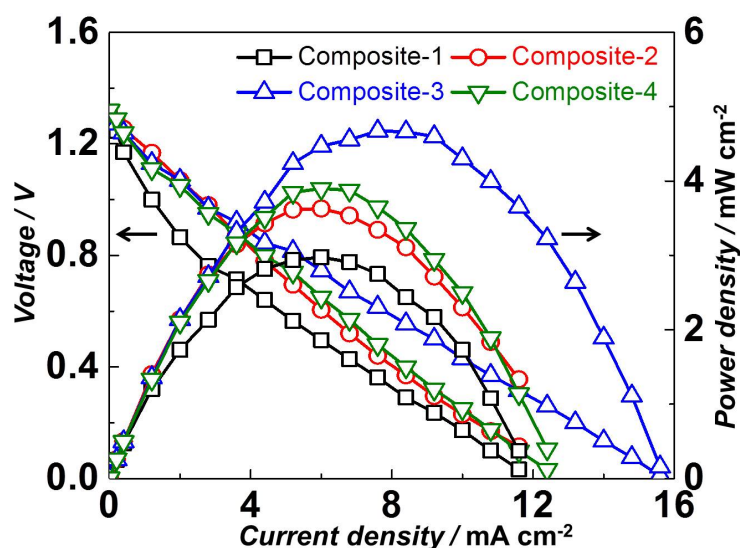
Figure 5.14: Cell performance with NCo@N-rGO containing variable wt% of N-rGO.

The wt% of N-rGO in NCo@N-rGO is varied from 6 wt%, 8 wt%, 10 wt% and 12 wt% and the results are shown in Fig. 5.14. The resulting dc-polarization curves reveal that the cell performance increases with increased loading of N-rGO upto composite-3. The cell power density increases by a factor of 1.57 compared to the base case. At loading of 12 wt% N-rGO loading in the composite, the cell performance decreases which may be due to the reduction in the available active surface area of the porous NCo microspheres by N-rGO at higher loadings.

5.3.4   Practical utility of the paper cell

A demonstration of the practical utility of the cell is shown in Fig. 5.15.

Here two cells are connected in series and a 3 mm LED bulb serves as the load. Once the anolyte and catholyte are discharged and reaches the electrodes, the LED starts glowing and continues to glow for nearly 30 minutes without the supply of fresh anolyte and catholyte. Once the cell is dry and the LED goes off, the cell can be revived by supplying fresh anolyte

and catholyte. This clearly proves that the cell can deliver sufficient power density for the required time, to power diagnostic devices that require milli-nano watt power.

Figure 5.15: Paper cell illuminating LED

5.3.5 Electrochemical impedance spectroscopy studies

The electrochemical impedance spectra of the cell is recorded for a frequency range of 1MHz to 0.1Hz with an amplitude of 10 mV voltage perturbation. Figure 5.16(a) shows the Nyquist plot for different concentrations of CH_3OH in the anolyte using plain carbon cloth as the electrode at an operating potential of 0.32 V, because the cell delivers maximum power density at $V_{cell} = 0.32\ V$.
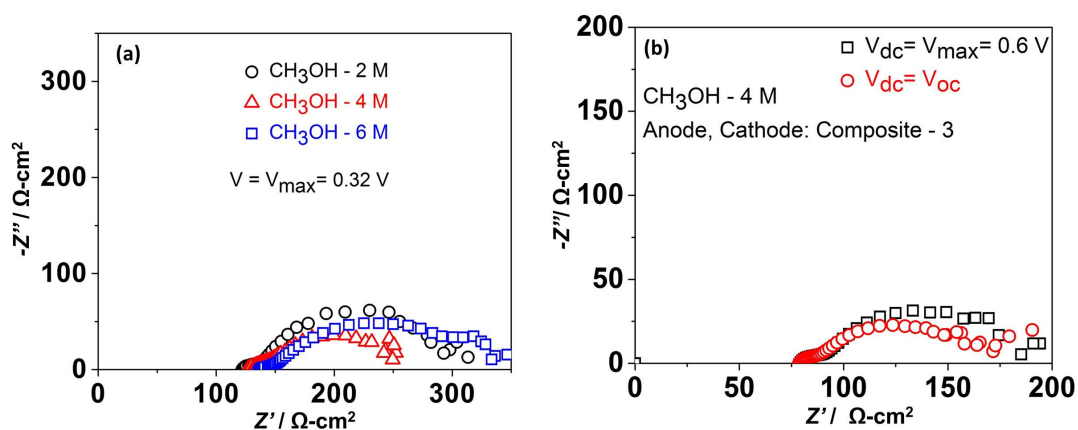
Figure 5.16: Electrochemical impedance spectra recorded at a frequency scan range of 1 MHz-0.1 Hz with sinusoidal voltage pertubation of 10 mV at (a) different CH_3OH in 4 M NaOH, at part load condition, V_{max}=0.32 V and (b) OCV and V_{max}=0.6 V. A,C- NCo@N-rGO composite-3 with 4 M CH_3OH + 4 M NaOH anolyte. The catholyte is 1 M $KMnO_4$ + 4 M H_2SO_4.

Slight variation in the Ohmic resistance (R_Ω), of the cell is observed, which is due to the variation in the ionic conductivity of the anolyte as a result of varying CH_3OH concen-

tration. On the other hand, the polarization resistance (R_p) vary significantly with the fuel concentration, with minimum R_p of 124 Ω-cm^2 observed for 4 M CH$_3$OH and maximum R_p of 222 Ω-cm^2 for 6 M methanol. This is in commensurate with the performance of the cell shown in Fig. 5.8. The increase in R_p at 6M and 2M CH$_3$OH concentration is due to the reasons cited for the decrease in performance of the cell with increasing and decreasing concentration for the base case reported in Fig. 5.8.

Figure 5.16(b) shows the EIS spectra recorded for 4 M methanol in the presence of composite-3 as catalyst on both the electrodes. The EIS is recorded at OCV as well as at the voltage that corresponds to the peak power density of the cell reported in Fig. 5.14. In all the EIS measurements, the scattering of data is observed at low frequency, which is due to the degradation in the cell performance. Ideally EIS must be measured at steady state conditions, however, at low frequencies the variation in the state of the system w.r.t to the starting and end of the cycle begins to have significant influence and leads to uncertainties in the data collected. Therefore, the low frequency intercepts reported here is only qualitative in nature. The presence of the catalyst brings down the R$_p$ to approximately 100 Ω-cm^2, which is in good agreement with the slops of the dc polarization data reported in Fig.5.14. At frequencies that are lower than the relaxation frequencies of the system, the impedance approaches the differential resistance obtained from the dc-polarization data. i.e, $Z(\omega \rightarrow 0) = V/I$.

The equivalent circuit for this T-shaped cell methanol paper cell is shown in Fig. 5.17. Here, R$_1$, R$_2$ and CPE$_1$ represent the same elements as explained above in Section 3.3.3, for one electrochemical process, while R$_3$ and CPE$_2$ are the charge transfer resistance and the capacitance of the double-layer for the other, respectively.
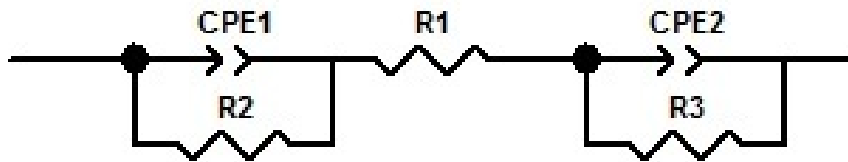
Figure 5.17: Equivalent circuit model representing half Randles circuit.

The relevant Nyquist plots are shown in Fig. 5.18 (a)-(c) and Fig. 5.19 (a)-(b). The simulated values are in good agreement with the experimental ones. The two semi-circles as seen across all the plots, represent two different processes occurring at the anode as the cathode side concentration is fixed.
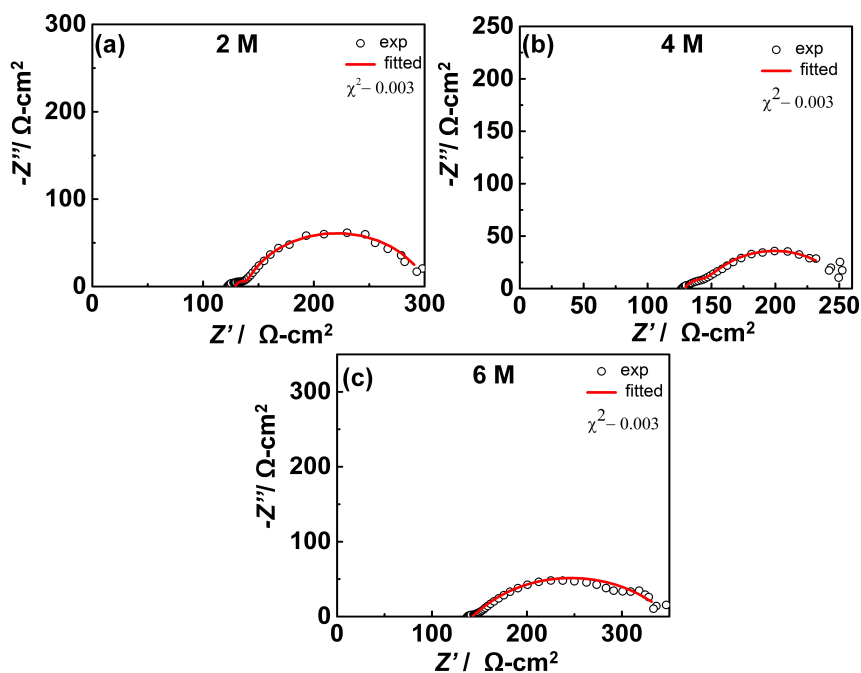
Figure 5.18: Electrochemical impedance spectra recorded at a frequency scan range of 1 MHz-0.1 Hz with sinusoidal voltage pertubation of 10 mV at different CH_3OH in 4 M NaOH, at part load condition, V_{max}=0.32 V. The catholyte is 1 M $KMnO_4$ + 4 M H_2SO_4. Experimental data is represented by open symbols. Lines represent fitted/simulated results.
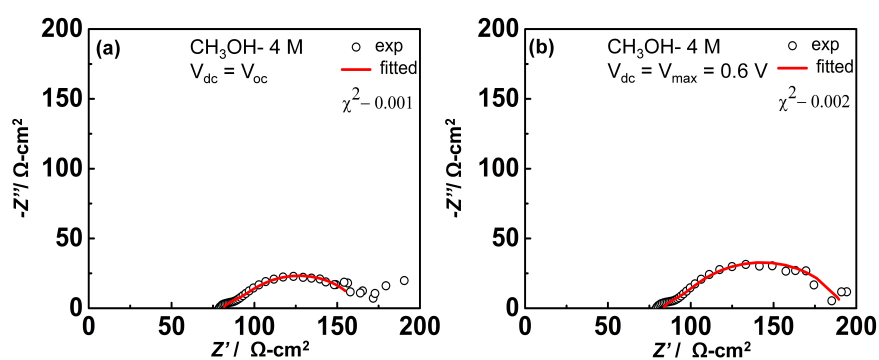
Figure 5.19: Electrochemical impedance spectra recorded at a frequency scan range of 1 MHz-0.1 Hz with sinusoidal voltage pertubation of 10 mV at 4 M CH_3OH in 4 M NaOH, at (a) OCV and(b) V_{max}=0.6 V. A,C-NCo@N-rGO composite-3 with 4 M CH_3OH + 4 M NaOH anolyte. The catholyte is 1 M $KMnO_4$ + 4 M H_2SO_4. Experimental data is represented by open symbols. Lines represent fitted/simulated results.

5.3.6 Modeling

The experimental dc-polarization data is fitted by assuming Butler-Volmer kinetics. Typically the exchange current density is a function of concentration of reactant and product concentration. The following set of equations are solved simultaneously to reproduce the experimental observations.

$$V_{\text{cell}} = E_{\text{rev}} - \eta_{\text{a}} - |\eta_{\text{c}}| - \eta_{\text{ohm}} - \eta_{\text{leak}} \tag{5.6}$$

$$i_{\text{a}} = i_{\text{a}}^0 \left(\exp\left(\frac{\alpha_{\text{a}} F \eta_{\text{a}}}{RT} \right) - \exp\left(\frac{-(1 - \alpha_{\text{a}}) F \eta_{\text{a}}}{RT} \right) \right) \tag{5.7}$$

$$i_{\text{c}} = i_{\text{c}}^0 \left(\exp\left(\frac{\alpha_{\text{a}} F \eta_{\text{c}}}{RT} \right) - \exp\left(\frac{-(1 - \alpha_{\text{a}}) F \eta_{\text{c}}}{RT} \right) \right) \tag{5.8}$$

In the above equations, V_{cell} is the operating cell voltage, η_{a} is the activation losses at the anode, η_{c}, is the activation losses at the cathode, η_{ohm} is the Ohmic losses, η_{leak} is the leakage overpotential, F is the Faraday constant, R is the gas constant, T is the temperature, α_{a} is the charge transfer coefficient, i_{a}^0 is the exchange current density at the anode, and i_{c}^0 is the exchange current density at the cathode. The exchange current densities are further expressed as function of concentrations according to

$$i_{\text{a}}^0 = i_{\text{a}}^* C_{\text{CH}_3\text{OH}} C_{\text{NaOH}}, \tag{5.9}$$

and

$$i_{\text{c}}^0 = i_{\text{c}}^* \frac{C_{\text{KMnO}_4} C_{\text{H}_2\text{SO}_4}}{1 + C_{\text{CH}_3\text{OH}}^{\text{x}} C_{\text{NaOH}}^{\text{y}}}. \tag{5.10}$$

In the above equations, i_{a}^* and i_{c}^* are fitting parameters. The cathode exchange current density is expressed as a function of the concentration of the anolyte to account for the cross diffusion. The set of equations are solved simultaneously using *fsolve* in MATLAB. The estimation of the fitting parameters x, y, i_{a}^*, and i_{c}^* is done using *lsqnonlin* solver, which applies Levenberg Marquradt algorithm. The values of the fitted parameters are given in Table 5.1.

Table 5.1: Parameters used to reproduce experimental observation

Parameter	i_{a}^* (mA cm^{-2})	i_{c}^* (mA cm^{-2})	x	y
Value	1.6×10^{-4}	0.055	0.05	0.1

A comparison of model predictions with experimental observation is shown in Fig. 5.20. From the experiments it is observed that the activation losses are due to the slow electrochemical oxidation of CH_3OH. Therefore, compared to the anode a low exchange current density value is used at the anode.
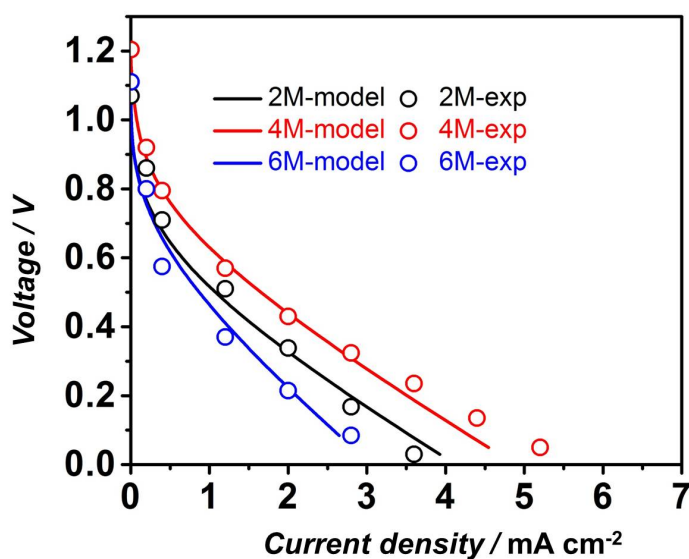
Figure 5.20: Dc-polarization curves at different CH_3OH concentration predicted by the mathematical model

5.4   Concluding remarks

In this work, we have presented the development, working and characterization of a paper supported methanol fuel cell with $KMnO_4$ as the oxidant. Varying concentrations of (2 M, 4 M and 6M) CH_3OH in 4M NaOH is used as the anolyte. A solution of 1M $KMnO_4$ and 4M H_2SO_4 is used as the catholyte, and its concentration is kept constant for all the experiments. The PAM gel serves as the medium for the transport of ions between the electrodes, and prevents the cross-over of the fuel and oxidant between the two paper strips to certain extend. The cell with plain carbon cloth as electrode delivers the maximum power at 4M CH_3OH compared to other concentrations studied. Therefore all further experiments are carried out using 4M CH_3OH in 4M H_2SO_4. In order to improve the cell performance hydrothermally synthesized flower like micro-spheres of $NiCo_2O_4$ and composite of $NiCo_2O_4$ and N-rGO, namely, NCo@N-rGO, have been employed as catalysts, in various loadings and electrode combinations. In all cases the cell gave the best performance when the electrocatalyst is present at both the electrodes and significant activation losses are observed when the electrocatalyst is not present at the anode. This leads to the conclusion that the cell performance is limited by the oxidation of CH_3OH and not due to the cathodic processes. The usefulness of the cell for practical applications is demonstrated by illuminating a 3mm LED bulb by stacking two cells in series. With the initial supply of 2 to 3 drops of anolyte and catholyte the LED bulb continued to glow for about 30 mins. Thus the cell

presented in this study can be used as a source of energy for applications in micro-nano systems that require power in nano to milli watts range. Finally the experimentally measured performance of the cell using plain carbon cloth is simulated using Butler-Volmer type kinetics, where the exchange current densities are formulated as function of concentration of the reactants.

Chapter 6

Ethanol-dichromate based fuel cells on a paper substrate

6.1 Introduction

This Chapter, final in the series of different redox couples studied to achieve better cell performance presents the development of an ethanol based cell. Unlike the studies presented in chapter 3,4 and 5, dichromate is used as the oxidant in this study. This redox couple has a standard cell potential of 1.7 V. The cell delivered an OCV, which is better than methanol based cell and formic acid cell presented respectively in Chapter 5 and Chapter 3. The cell architecture is same as the ones presented in the previous chapters. However, for this study, MoO_3 nano rods are used as the catalyst to enhance the cell performance. Molybdenum oxide (MoO_3) is an inexpensive alternative to the noble metal catalysts. MoO_3 has a good ethanol sensing property [71], and by preparing the same in nanostructured form, the catalytic surface area can be enhanced which can lead to high oxidation currents. While a composite of MoO_3 with poly(pyrrole) has been used as a support for PtPd nanoparticles for ethanol electro-oxidation in DEFC [72], MoO_3 as a stand-alone catalyst in paper based ethanol fuel cell has not been reported so far. The cell delivers a power density of 6.28 mW cm^{-2}, which is 10.8 times higher than formic acid cell (Chapter 3), 1.75 times higher than hydrazine cell (Chapter 4) and 1.35 times higher than methanol cell (Chapter 5). As a fuel, ethanol has several advantages. It has a high volumetric energy density (as compared to methanol and formic acid) of 6.28 kWh l^{-2}, and is considered as renewable fuel [73] and is less toxic. Again as in the case of methanol fuel cell, the practical utility of the cell is demonstrated by lighting a 3 mm LED. With a few drops of the anolyte and catholyte, the cell could light the bulb for 40 mins without replenishing with fresh anolyte and catholyte. The cell relies on the oxidation of ethanol at the anode for the production of electrons and protons. The electrons reach the cathode via the external circuit, and simultaneously the

protons migrate to the cathode though the Na-PSS/PVA/H$^+$ gel electrolyte. Dichromate ions (oxidant) undergo reduction at the cathode by accepting the electrons from the anode. These reactions can ideally occur at any location where the carbon cloth (with or without MoO$_3$ NRs) comes in contact with the anolyte/catholyte. The oxidation of ethanol follows complex pathways leading to the formation of acetaldehyde and acetic acid as by-products. The formation of CO is also reported previously [110]. The reduction of dichromate at the cathode is given by

$$Cr_2O_7{}^{2-} + 14H^+ + 6e^- \rightleftharpoons 2Cr^{3+} + 7H_2O, \tag{6.1}$$
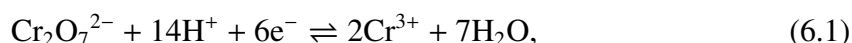
It can be seen in the reaction that, Cr^{6+} in Cr$_2$O$_7{}^{2-}$ reduces to Cr^{3+}. Being a transition metal ion, Cr^{3+} can exist as an aquo-complex, [Cr(H$_2$O)$_6$]$^{3+}$ in solution. The oxidation reaction at the anode is given by

$$C_2H_5OH + H_2O \rightarrow 2CO_2 + 12H^+ + 12e^-. \tag{6.2}$$

The overall cell reaction is given by

$$16H^+ + 2Cr_2O_7{}^{2-} + C_2H_5OH \rightarrow 4Cr^{3+} + 11H_2O + 2CO_2. \tag{6.3}$$
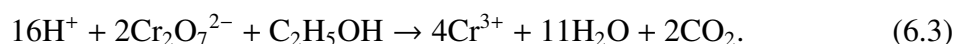
6.2 Experimental

6.2.1 Chemicals

Ethanol (C$_2$H$_5$OH), nitric acid (HNO$_3$), toluene(C$_6$H$_5$CH$_3$) and sodium polystyrene sulphonate (NaPSS) were purchased from sigma aldrich. Potassium dichromate (K$_2$Cr$_2$O$_7$) polyvinyl alcohol(PVA), ammonium heptamolybdate tetrahydrate ((NH$_4$)6Mo$_7$O$_{24}$.4H$_2$O) were purchased from merck. Sulfuric acid (H$_2$SO$_4$) was purchased from Fischer Scientific. Whatman filter (ashless 40) was used as the medium of transport. Ultrapure water of resistivity 18.2 MΩ cm, was acquired from a Millipore direct Q3UV system. All the reagents used in this study were of analytical grade, and were used as received.

6.2.2 Cell assembly

The cell was assembled by placing two L-shaped paper strips 0.2 cm apart, and the sodium poly(4-styrenesulfo-nate) (Na-PSS) gel was placed in between the strips as shown in the inset of Fig. 6.1(a). The thickness of the gel membrane is 0.5 mm. The gel acts as a proton exchange membrane for the transport of ions. The Na-PSS/PVA/H$^+$ gel was placed using a spatula in the space between the two L-joints of the two paper strips. Fig. 6.1(b) shows the schematic of the cross sectional view of the electrodes with a description of the

electrochemically active thickness over which the reactions takes place. It is not possible to determine the actual thickness of the electrochemically active layer, which is denoted by δ in Fig. 6.1(b). The electrons, which are released in the electrochemically active layer, are conducted by the carbon cloth and collected by the SS current collectors. Fig. 6.1(b) also shows the electron transfer path.

Aqueous solutions containing varying concentrations of C_2H_5OH (2 M, 3 M, 4 M, 5 M, and 6 M) along with 4 M H_2SO_4 (electrolyte) are used as the anolytes. Aqueous solutions of 0.3 M $K_2Cr_2O_7$ (oxidant) along with 4 M H_2SO_4 are used as the catholytes and 0.2 mL each of anolyte and catholyte are used. The short arm (0.5 cm × 2.5 cm) of each L-shaped paper strip serves as the inlet for the anolyte/catholyte, and the longer arm (0.5 cm × 8 cm) serves as the outlet for the products and unused reactants, as shown in Fig. 6.1(a).
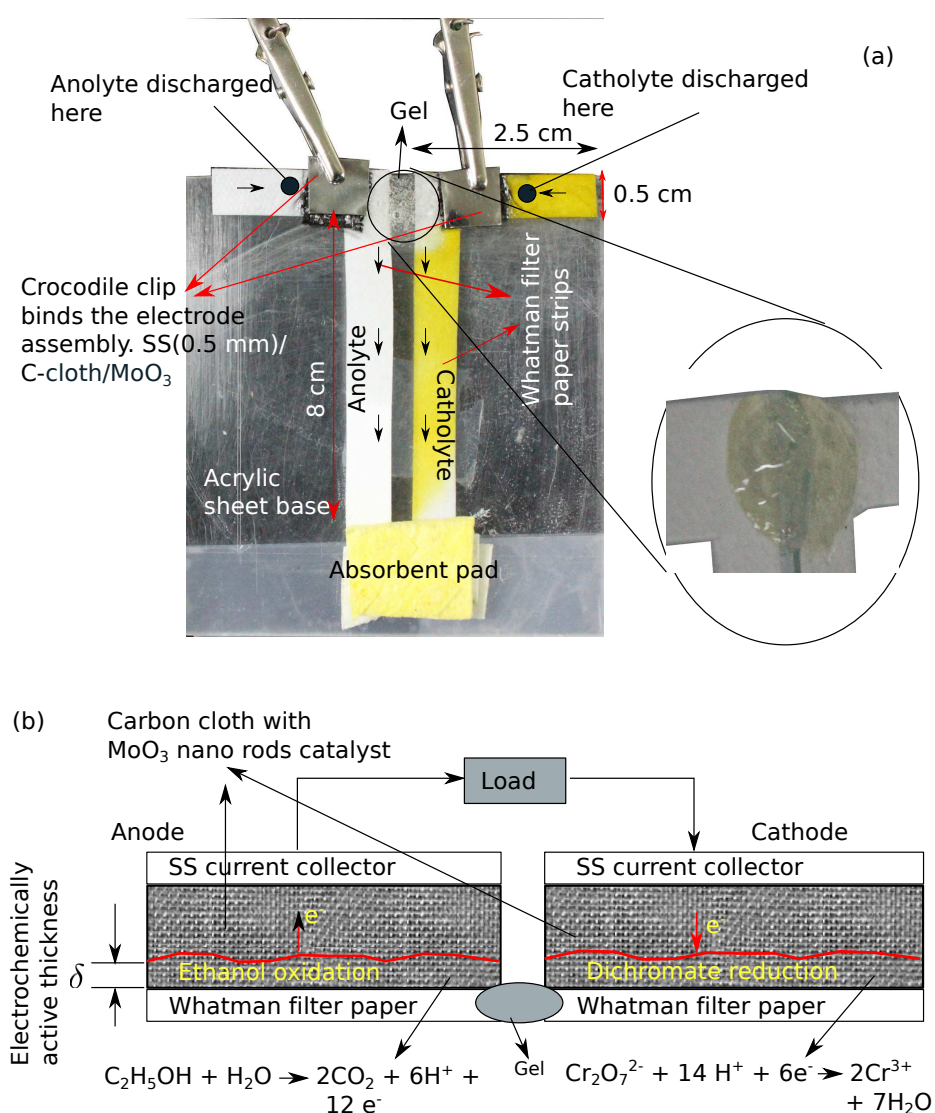
Figure 6.1: (a) Photograph of the cell assembly and (b) Schematic of the cross sectional view

Carbon cloth of size 0.5 cm × 0.7 cm is placed on the inlet arm of the L-shaped paper strip, which serve as the electrodes. Since the electrodes are in contact with the electrolyte phase present in the fuel and oxidant, the geometric area (0.35 cm^2) of the electrodes is used to calculate the current density. Steel plates of dimensions equal to the electrode are used as the current collectors. The by-products and unreacted species flow by the capillary action towards the outlets, i.e. the longer arms. The objective of keeping the outlet strip long is to avoid the back flow of the by-products to the electrodes and the gel, which can otherwise interfere with the cell reactions by diluting anolyte and catholyte. Since ethanol is volatile, the length of the inlet arm is kept short so that once the anolyte/catholyte containing the fuel/oxidant are discharged near the electrodes, they are immediately utilized. An absorbent pad is placed at the bottom of the cell to absorb the products and the unused reactants. The absorbent pad used in the cell is basically a spongy material (similar to kitchen wipe) having 3 mm thickness. The paper used is a Whatman filter paper (ashless 42) of thickness 0.13 mm. The anolyte and catholyte are discharged near electrodes using a pipette. The whole assembly is placed on an acrylic sheet.

6.2.3 Preparation of Na-PSS/PVA/H$^+$ gel/membrane

A solution was prepared by dissolving 2 g of Na-PSS/H$^+$ in 10 mL of deionized water. The resulting solution was stirred at 500 rpm and heated at a temperature of 75 °C for 10 minutes. Once the solution was completely homogeneous, 0.8 g of poly(vinyl acetate) (PVA) was added and stirring was continued for another 45 minutes to make the solution sufficiently viscous. PVA acts as a gelatinizing agent and imparts mechanical strength to the gel. After the stirring was complete, the viscous gel was cooled at room temperature. The final yellow coloured substance was referred to as Na-PSS/PVA/H$^+$ gel or membrane. The proton exchange in Na-PSS/PVA/H$^+$ gel occurs at the sulfonate moiety ($-SO_3Na$ to $-SO_3H$). The pH of the gel was 5-6 as measured by a pH paper.

6.2.4 Synthesis of MoO$_3$ NRs and electrode preparation

MoO$_3$ NRs were synthesized hydrothermally according to the procedure described else-where [125]. 1 g of ammonium heptamolybdate ($(NH_4)_6Mo_7O_{24}\cdot4H_2O$) was dissolved in 40 mL solution containing 65% HNO$_3$ and deionized water (HNO$_3$:H$_2$O, v/v 1:5). After complete dissolution of $(NH_4)_6$ Mo$_7$O$_{24}\cdot4H_2$O, the above solution was transferred to a 50 mL teflon cup and placed in a stainless steel (ss) autoclave. This was then placed in an electric oven and heated at a temperature of 180 °C for 12 hours. Then the solution was cooled to the room temperature and centrifuged to extract the MoO$_3$ NRs. These were then washed with copious amounts of ultra-pure water and the black precipitate was dried overnight in

a hot-air-oven at 60 °C. Carbon cloth of size 0.5 cm × 0.7 cm was used as electrodes. 10 mg of the MoO_3 powder was dissolved in 10 mL of toluene and drop cast onto the carbon cloth electrodes by a pipette. Electrodes with variable catalyst loadings were prepared to study the effect of catalyst content.

6.2.5 Synthesis of Ag nanoparticles (Ag NPs)

For the synthesis of Ag NPs 0.101 g of silver nitrate ($AgNO_3$) and 0.12 g of poly(N-vinyl-2-pyrrolidone) (PVP) were dissolved in 8 mL dimethyl formamide (DMF) in a 10 mL glass bottle. This was then placed in a microwave oven, which was subjected to irradiation for 5 seconds, resulting in a brownish colored homogeneous solution, which indicates the formation of the Ag NPs.
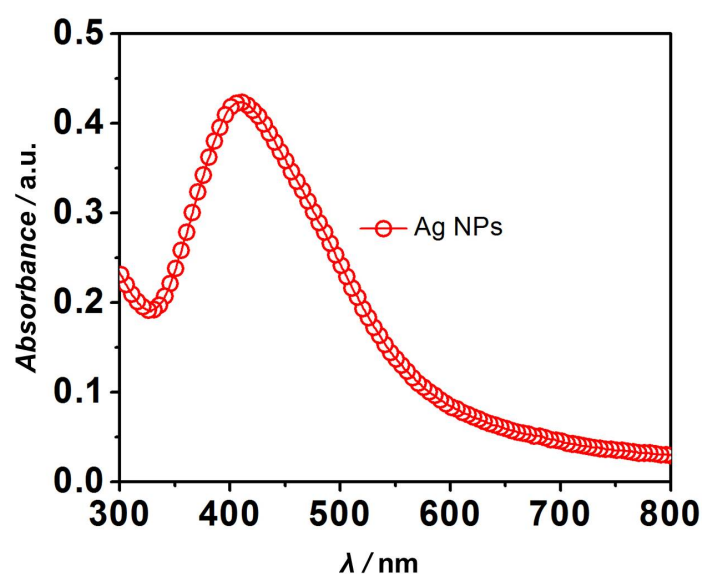
Figure 6.2: UV-vis spectrum of Ag NPs

6.2.6 Instrumentation

The electrochemical measurements of the cells, i.e., chronoamperometry (I *vs* t), chronopotentiometry (V *vs* t), electrochemical impedance spectroscopy (EIS) and cyclic voltammetry (CV) were done by an Autolab PGSTAT 302N with a frequency response analyzer and integrated NOVA 1.11 software. The structure and morphology of the prepared MoO_3 NRs catalyst were studied using a Zeiss field emission scanning electron microscope (FE-SEM) by obtaining the micrographs for the catalysts. Transmission electron microscope (JEOL JEM2100) with a resolution of 2.3Å was used for characterizing the catalyst. The powder

sample (MoO_3) was dispersed in isopropanol, and a thin layer of the solution was placed onto carbon coated copper grids. The samples were then analyzed after isopropanol was evaporated from the deposited layers.

6.3 Results and discussion

6.3.1 Characterization of Ag NPs

The formation of the Ag NPs was confirmed by UV/vis spectroscopy and the relevant UV absorption spectrum is shown in Fig. 6.2. The surface plasmon band observed at λ_{max} = 412 nm confirms the formation of the Ag NPs.
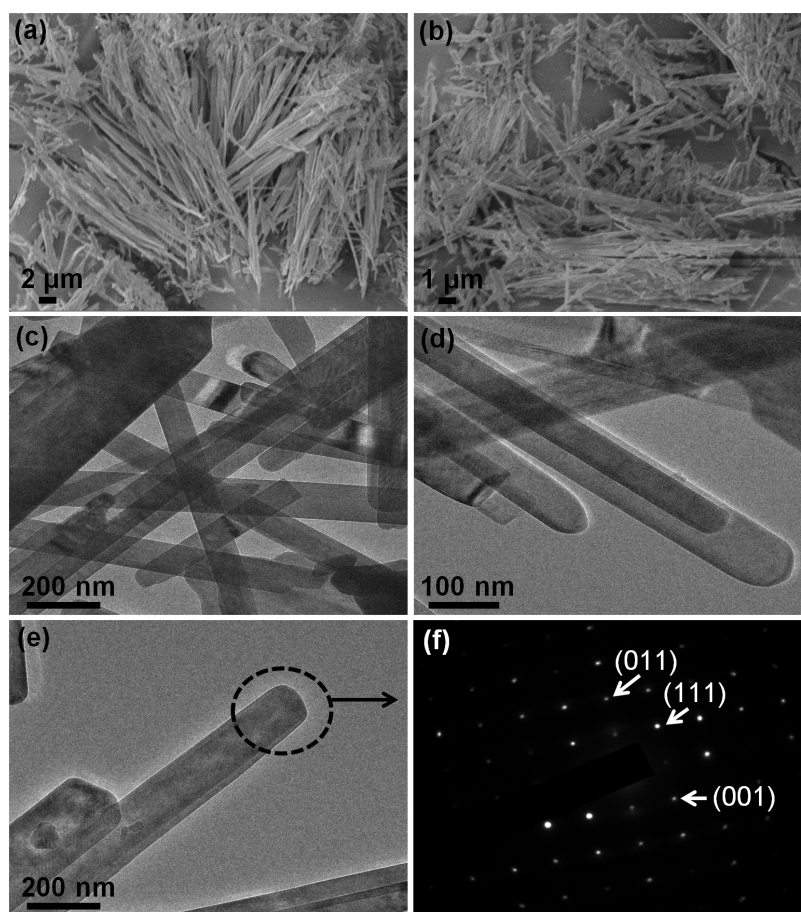
Figure 6.3: (a) and (b) FE-SEM images of MoO_3 NRs. (c)-(e) TEM images MoO_3 NRs and (f) the corresponding SAED pattern of a MoO_3 NR.

6.3.2 Structural features of MoO₃ NRs

Prior to studying the fuel cell performances, the structure and morphology of the prepared MoO_3 NRs are studied by FE-SEM and TEM. The FE-SEM images of MoO_3 NRs are shown in Fig. 6.3(a) and (b). Both the images are obtained at low magnification and they show bundles of misaligned and monodispere nanorods. The corressponding TEM images are shown in Fig. 6.3(c)-(e). At low resolution, the nanorods overlap with each other, but at high resolution (Fig. 6.3(d)) distinct formation of nanorods with uniform width along the length are observed. The surfaces appear to be smooth. The diameter and length of the nanorods vary from 50 nm to 125 nm and from 800 nm to 2 μm, respectively. The aspect ratio (L/D) for these nanorods ranges from 6 to 22. The selected area electron diffraction (SAED) pattern, for MoO_3 NRs is shown in Fig. 6.3(f). The bright single spots are due to the beam diffraction by a single crystal, which confirms the crystallinity of the synthesized MoO_3 NRs. The spots are indexed to the (011), (111) and (101) planes of the orthorhombic crystal structure of MoO_3. Similar SAED patterns for MoO_3 NRs have been reported by other researchers as well [126, 125].

6.3.3 Electrochemical performance and gel characterization

It is generally accepted that multiple electron transfer reactions are rare in reality and therefore, the actual mechanism of oxidation of ethanol can be expected to be multi-step, eventually culminating with the formation of either CO or CO_2. At the cathode, dichromate reduction is accompanied by the conversion of Cr (VI) to Cr (III) species. Cyclic voltammetery (CV) plots were recorded to study ethanol oxidation (4 M ethanol in 4 M H_2SO_4) in an aqueous acidic medium with Ag/AgCl/KCl as a reference electrode and a Pt rod as a counter electrode.

CV plots of carbon cloth loaded with MoO_3 NRs and blank carbon cloth (as working electrodes) are shown in Fig. 6.4. The voltage is swept back and forth from -0.5 to 2.0 V (versus Ag/Ag^+) at a scan rate of 20 mV s^{-1}.

To understand the influence of MoO_3 NRs in the electro-oxidation of ethanol, experiments are initially performed without MoO_3 on the carbon cloth. The nonappearance of peaks in the forward and reverse sweeps indicates the absence of diffusion layer formation or depletion effects. The presence of two broad shoulders clearly indicates that the oxidation of ethanol is governed by multi-step charge transfer reactions involving different species that are electrochemically active. The first shoulder is observed at approximately 0.48 V. The two different shoulders in the forward sweep correspond to two different rate limiting charge transfer reactions. On reversing the potential, the curve traces back the forward sweep until the first shoulder, indicating that there is an abundance of surface adsorbed

species responsible for electron transfer at the electrode. i.e., on reversing the potential, the current is still anodic, until the first shoulder. The reduction current starts flowing on reducing the potential further. The behavior is same with and without MoO_3 NRs, except that the presence of MoO_3 NRs increases the area enclosed in the voltammogram, implying that MoO_3 NRs show good electrocatalytic activity for ethanol oxidation.
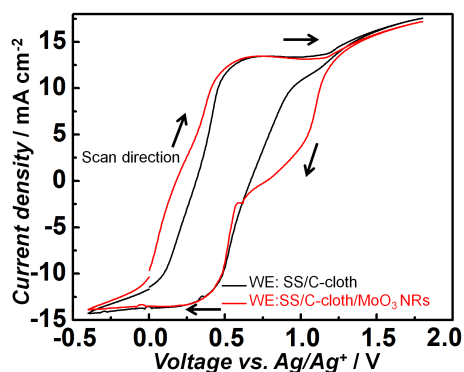
Figure 6.4: Cyclic voltammograms for ethanol-oxidation with MoO_3 NRs loaded carbon cloth and blank carbon cloth as working electrodes.

Cyclic voltammetry (CV) plot showing response of MoO_3 NRs loaded carbon cloth as working electrode in 4 M H_2SO_4 in an aqueous acidic medium, with Ag/AgCl/KCl as a reference electrode and a Pt rod as a counter electrode. The voltage is swept back and forth from -0.5 to 2.0 V (versus Ag/Ag$^+$) at a scan rate of 20 mV s^{-1}. The voltammogram shows a similar profile without ethanol, except that the enclosed area is enhanced. This could be due to the fact that, in the absence of ethanol the response of MoO_3/CC is mostly capacitive and no faradaic reactions are occurring in the system.
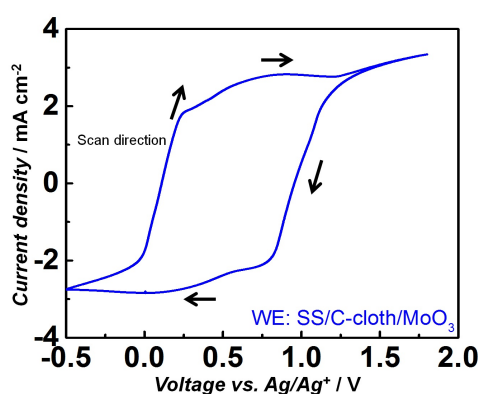
Figure 6.5: Cyclic voltammograms showing response of MoO_3 NRs loaded carbon cloth and blank carbon cloth as working electrode in 4 M H_2SO_4. The counter electrode is Pt rod, reference electrode is Ag/AgCl and scan rate is 20 mV s^{-1}.

Since the Na-PSS/PVA/H$^+$ gel electrolyte is used as membrane to facilitate the transport of ions (primarily protons or H$^+$) between the electrodes, the conductivity of gel is measured by performing EIS. Na-PSS/PVA/H$^+$ is a polyelectrolyte and SO$_3^-$ Na$^+$ groups present along the backbone of the polymer chain, serve as the active sites for the transport of protons. The SO$_3^-$ groups are attached to the backbone of the polymer poly(styrene) and are immobile. The Na$^+$ ions are replaced by H$^+$ ions which are released from the dissociation of H$_2$SO$_4$ in the gel. The charge transfer mechanism is believed to be the same as the one that prevails in a Nafion membrane.

The conductivity of the gel is measured by placing the gel electrolyte between two steel plates under an ac-amplitude of 10 mV without any dc bias over a frequency range of 1 MHz-1 kHz. The resulting Nyquist plot (Fig. 6.6(a)) shows an inclined line. The high frequency intercept on the abscissa corresponds to the resistance (R) offered by the gel for H$^+$ movement. The conductivity of the gel (σ) is calculated using $\sigma = (1/R) \times (l/a)$, where l (cm) is the thickness of the gel layer and a (cm^2) is the area of the SS plates in contact with the gel. At room temperature this resulted in 0.063 S cm^{-1}. The conductivity of the gel as a function of temperature is shown in Fig. 6.6(b). The conductivity of the gel increases with temperature due to enhanced mobility of H$^+$ ions at high temperatures. At room temperature, the gel is transparent, homogeneous and yellow in color. At temperatures above 55 ^{o}C, it becomes opaque. The Na-PSS/PVA/H$^+$ gel can therefore be used upto 50 ^{o}C.
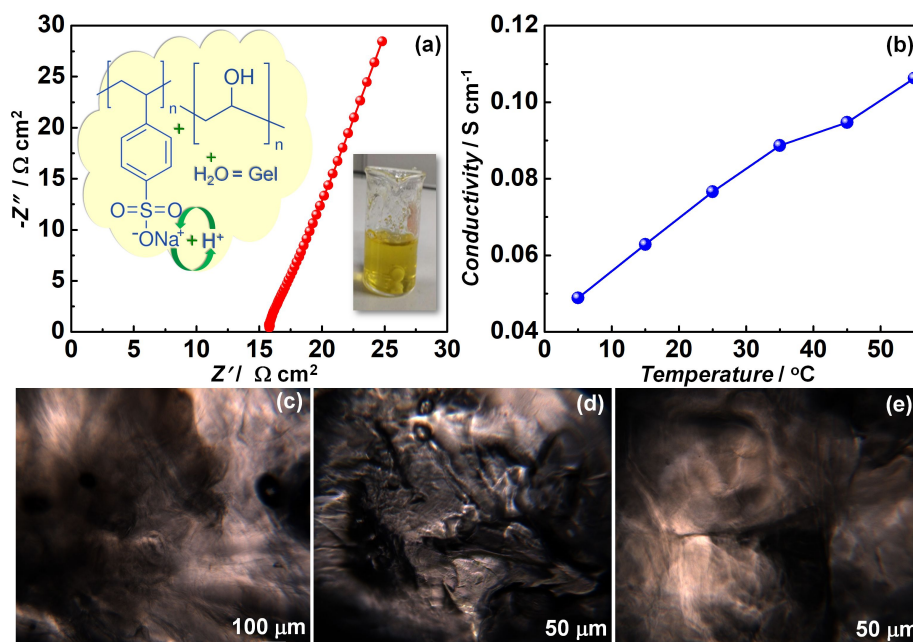
Figure 6.6: (a) Nyquist plot of the Na-PSS/PVA/H$^+$ gel and (b) variation of conductivity versus temperature for the same gel. Insets of (a) show the composition and a photograph of the gel.

In the present study, all the cells are assembled and studied at room temperature. For the electrochemical charge transfer reaction to occur, a three phase interface between ion conducting phase, electron conducting phase and the fuel/oxidant is required. In the present study, ion transport occurs due to the presence of H_2SO_4, which is added to the fuel and the oxidant in order to form the anolyte and the catholyte, respectively. Carbon cloth is used as the electron conducting phase. Due to the presence of H_2SO_4 throughout the system, a physical contact of the gel membrane with the electrodes is strictly not required for the progress of the charge transfer reaction. Thus in this work, the two paper strips are completely disconnected when the gel is not placed between them. The gel acts as a bridge for the transport of ions from the anode to the cathode, and without the presence of gel between the electrodes, the cell will not be able to generate power.

Cells are assembled on paper supports with SS/carbon-cloth as the electrodes and a Na-PSS/PVA/H^+ gel. The electrochemical performance of the cell is studied by varying the fuel or ethanol concentration from 2 to 6 M, in 4 M H_2SO_4, while keeping the concentration of catholyte constant (0.3 M $K_2Cr_2O_7$ + 4 M H_2SO_4). Carbon cloth without any catalyst loading is used as the electrode. A new cell is prepared and used every time the fuel concentration is changed. The dc-polarization curves for different fuel concentrations are shown in Fig. 6.7(a) and (b).
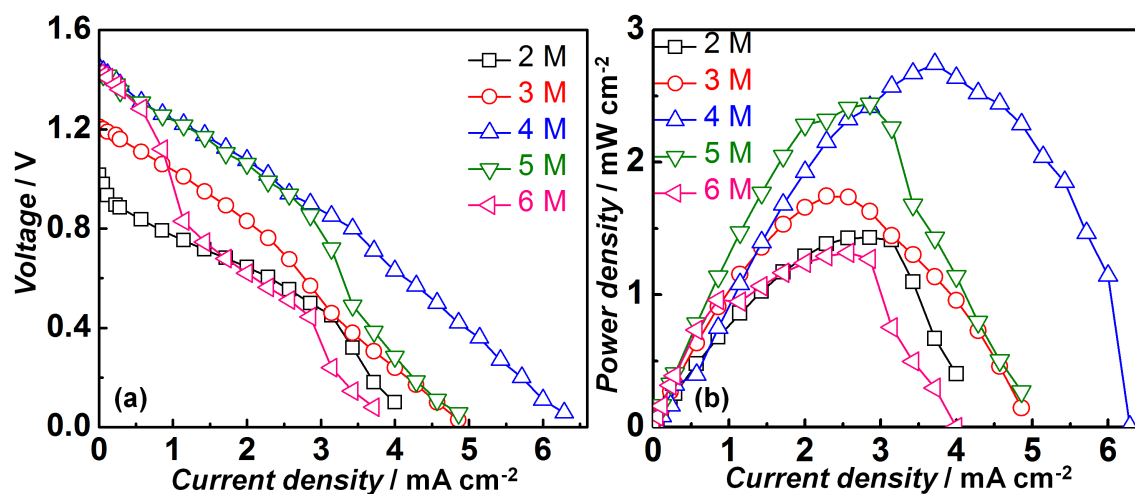
Figure 6.7: Cell performance at various ethanol concentrations in 4 M H_2SO_4. The catholyte is an aqueous solution of 0.3 M $K_2Cr_2O_7$ + 4 M H_2SO_4. SS/carbon cloth are used as the electrodes.

The cell delivers low open circuit voltage (OCV) at low concentrations of 2 and 3 M, and higher OCVs at 4 M, 5 M and 6 M ethanol, which is due to the dependence of reversible voltage on concentration according to Nernst equation. The standard potential term in the Nernst equation is independent of concentration and the concentration dependent term is $-(RT/nF)\ln(\prod a_p^{\gamma_i} / \prod a_r^{\gamma_i})$. The absolute value of this term increases with the increase in

the activity of the reactants for a given activity of the products. The overall cell performance is poor at low and high concentrations of ethanol (Fig. 6.7(b)). At low concentrations, the poor cell performance is due to the low Faradaic reaction rates because of the concentration dependency of exchange current density.

It is well known that the ethanol oxidation kinetics is slow, and hence higher concentrations are required for higher reaction rates and better cell performance. However, at higher concentrations of ethanol, cross-over to the cathode through the Na-PSS/PVA/H$^+$ gel is high, which again leads to a poor cell performance. In order to verify this, a control experiment or a paper wetness test is performed. The Na-PSS/PVA/H$^+$ gel is placed between two paper strips and ethanol is discharged near the anode. Ethanol starts to diffuse across the gel membrane to the cathode side of the paper and makes it wet. The length traversed by ethanol on the cathode side of the strip in a given time is measured for different concentrations. It is found that higher concentrations led to faster cross over. The fuel utilization is generally low for these cells, and hence only a small fraction of the fuel participates in the reactions. Since the cell delivers the maximum power density (MPD) of 2.74 mW cm^{-2} and current density of 6.28 mA cm^{-2} at 4 M ethanol, in this study it is chosen as the best fuel concentration to work with. The rest of the experiments reported in this work are performed at 4 M ethanol + 4 M H$_2$SO$_4$, (anolyte) and 0.3 M K$_2$Cr$_2$O$_7$ + 4 M H$_2$SO$_4$ (catholyte).

In addition to this, it is also observed that the stability of the cell does not significantly depend on the length of the arm. In fact for these type of cells, the flow rates and the fuel utilization are very low. If the products accumulate around the electrode, then it will start affecting the OCV and stability of the cell. This will happen if the length of the arm is small. A comparison of the cell performance for different arm lengths is shown in Fig. 6.8. It can be clearly observed that the case with short arm length leads to much lower performance as compared to other cases. Hence the length of the longer arm is kept at 8 cm.

In order to improve the cell performance, MoO$_3$ NRs are used as the catalyst at the anode for accelerating the ethanol oxidation reaction. Cell performances at various loadings of MoO$_3$ NRs at the anode are shown in Fig. 6.9. Catalyst free carbon cloth is used as the cathode. MoO$_3$ NRs are prepared by hydrothermal routes and then dispersed in toluene and drop-cast at the anode. The catalyst loading is optimized on the basis of the maximum power density delivered by the cell. The maximum power density increases from 4.67 mW cm^{-2} to 5.32 mW cm^{-2} as the MoO$_3$ NRs loading is increased from 0.09 to 0.18 mg cm^{-2}. This is an expected result because of the increase in active sites with higher catalyst loading. As ethanol oxidation rate is generally slow, availability of large amounts of three phase boundary (TPB) area can lead to higher rates for the electrochemical reactions. Higher catalyst loading usually leads to increase in the TPB and hence increase in the ex-
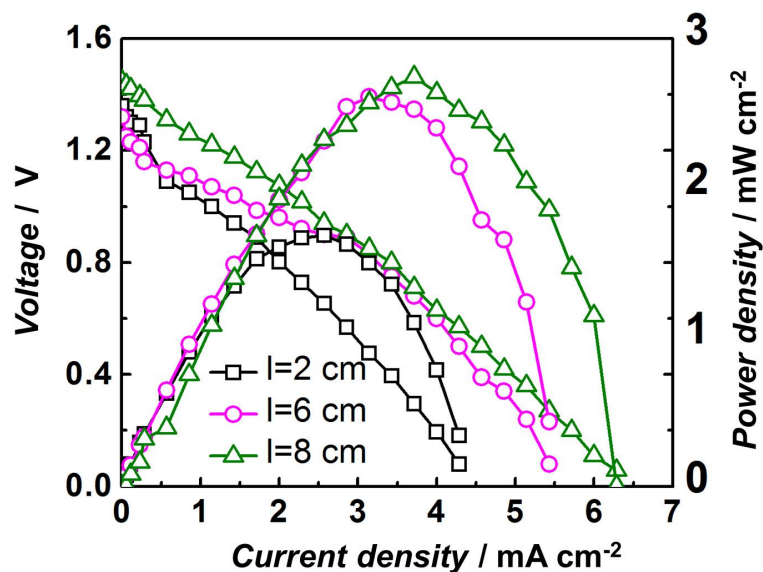
Figure 6.8: Cell performance at different channel lengths (l=longer arm of the cell). The anolyte is 4 M ethanol + 4 M H_2SO_4. The catholyte is 0.3 M $K_2Cr_2O_7$ + 4 M H_2SO_4. Carbon cloth is used as anode and cathode.

change current density. No significant improvement in the cell performance is observed by increasing the oxide loading further, probably due to the agglomeration of particles. Therefore, the loading of MoO_3 NRs is maintained at 0.18 mg cm^{-2} for the rest of the experiments.
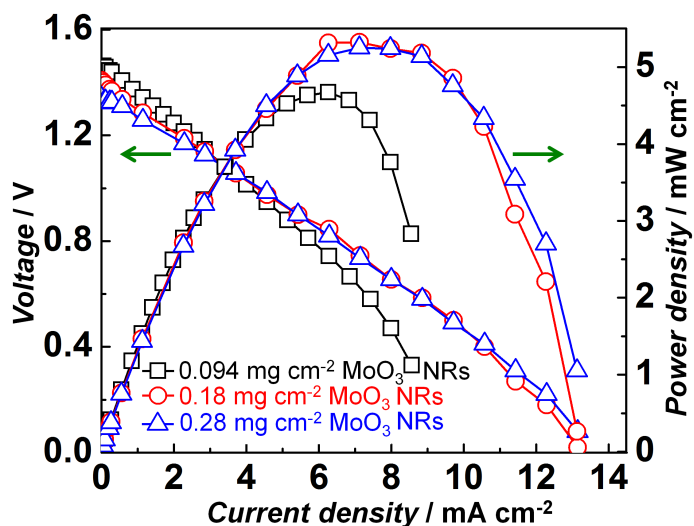
Figure 6.9: Cell performance at various catalyst (MoO_3 NRs) loadings. Anode is SS/carbon cloth/MoO_3 NRs and cathode is SS/carbon cloth. Anolyte is 4 M ethanol + 4 M H_2SO_4 and catholyte is 0.3 M $K_2Cr_2O_7$ + 4 M H_2SO_4.
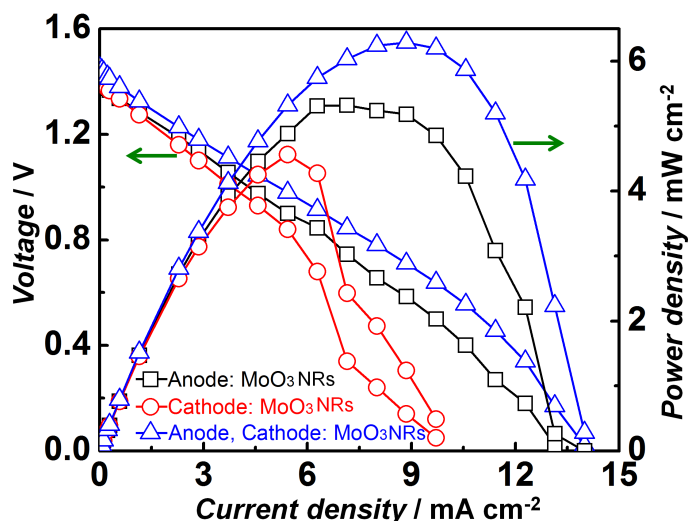
Figure 6.10: Cell performance for different electrode combinations with 0.18 mg cm^{-2} MoO$_3$ NRs loading. Anolyte is 4 M ethanol + 4 M H$_2$SO$_4$. Catholyte is 0.3 M K$_2$Cr$_2$O$_7$ + 4 M H$_2$SO$_4$.

The electrocatalytic effect of MoO$_3$ NRs for ethanol oxidation and dichromate reduction is studied by loading them individually on the anode, cathode and then on both the electrodes. In all cases, the loading is maintained at 0.18 mg cm^{-2}. Figure 6.10 shows that the cell performance with MoO$_3$ NRs is better than cell performance obtained using blank carbon cloth as electrode.With MoO$_3$ NRs as the anode electrocatalyst, the cell delivers a maximum power density of 5.32 mW cm^{-2}, which is higher than the maximum power density obtained using blank carbon cloth by almost 200%. With MoO$_3$ NRs as the cathode electrocatalyst, the maximum power density improves by 166% compared to blank carbon cloth. The best cell performance with 230% improvement (6.28 mW cm^{-2}) over blank carbon cloth electrodes is achieved when MoO$_3$ NRs are present at both the electrodes. This confirms that MoO$_3$ NRs catalyze both ethanol oxidation and dichromate reduction and therefore are suitable as low cost ecofriendly catalysts for these cells.

6.3.4 Comparison of MoO$_3$ NRs versus Ag nanoparticles (Ag NPs) as catalyst

In order to benchmark the performance of MoO$_3$ NRs, it is compared against Ag nanoparticles, which is reported to have good electro-oxidation kinetics for ethanol. For instance, Ag NPs supported on TiO$_2$ nanotubes [127] and bimetallic alloys containing Ag, such as, Pd/Ag [128] have shown high electro-catalytic activity towards ethanol electro-oxidation. Since MoO$_3$ NRs have been employed as stand-alone catalysts in this work, Ag NPs were synthesized and incorporated as catalysts by drop casting onto the carbon cloth for comparing the performance of MoO$_3$ NRs against Ag NPs.
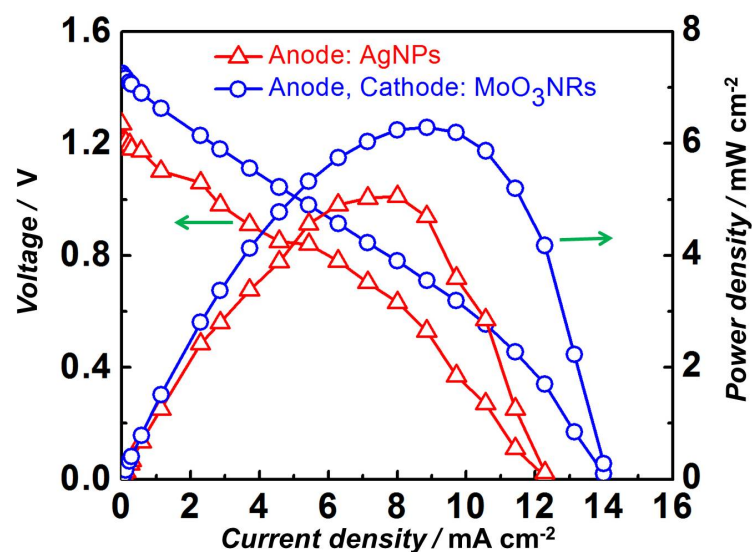
Figure 6.11: Comparison of cell performances using Ag NPs and MoO_3 NRs as the catalysts. Anolyte is 4 M ethanol + 4 M H_2SO_4. Catholyte is 0.3 M $K_2Cr_2O_7$ + 4 M H_2SO_4.

The presence of Ag NPs on both the electrodes leads to very low OCV of 0.66 V, possibly because of the following reasons: (i) The reaction between Ag and $K_2Cr_2O_7$ present at the cathode in an acidic medium, resulting in the formation of by-products, such as K_2SO_4 and $Ag_2Cr_2O_7$. (ii) The dilution effect caused by the formation of by-products. Therefore, this study was not considered for comparing the cell performance with MoO_3 NRs. The cell gave a better performance when Ag NPs were only present at the anode, and it was compared with the performance obtained with MoO_3 NRs. The corresponding I-V plots are presented in Fig. 6.11. It can be seen that the maximum power density obtained using Ag NPs (5.06 mW cm^{-2}) results in an increment of 87% compared to the base case (no catalyst), where the maximum power density attained was nearly 2.7 mW cm^{-2}. However, the performance of Ag NPs as an electrocatalyst for the redox couple considered in this study is inferior compared to the performance of MoO_3 NRs, which lead to a peak power density of 6.28 mW cm^{-2}. Thus, MoO_3 NRs prove to be better catalysts for both ethanol oxidation and dichromate reduction, unlike Ag NPs, which can favor the oxidation of only ethanol. Additionally, the use of Ag NPs or any noble metal catalyts, is not justified where the main aim is to develop cheap and cost-effective energy devices.

6.3.5 Cell performance at an elevated temperature

The cell performance is measured at 50 °C by placing the fully assembled cell with MoO_3 NRs present at anode and cathode, on a hot plate where the temperature was maintained at

50 °C. The corresponding I-V plot for the cell performance is shown in Fig. 6.12.
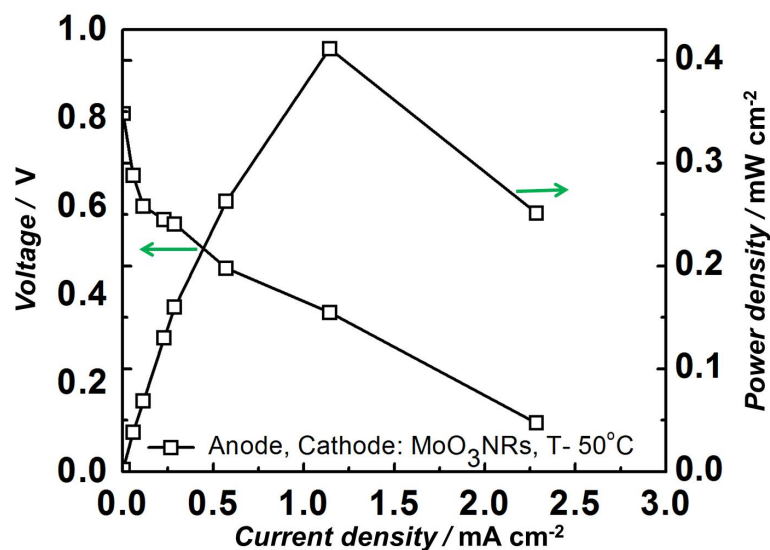
Figure 6.12: Cell performance at 50 °C. Anolyte is 4 M ethanol + 4 M H_2SO_4. Catholyte is 0.3 M $K_2Cr_2O_7$ + 4 M H_2SO_4. Anode, Cathode: MoO_3 NRs.

The OCV obtained at this temperature is 0.8 V, which is much lower than the OCV achieved at room temperature (1.44 V). Ethanol is volatile and tends to evaporate at 50 °C, resulting in a low fuel concentration in the anolyte. The change in Gibb's free energy at higher temperature may also lead to drop in OCV. Hence, lower OCV and power density of 0.4 mWcm^{-2} are obtained at this temperature. Therefore, the cell performance is likely to deteriorate beyond 50 °C. Nevertheless, even at elevated temperatures, the cell is capable of delivering power and the performance is comparable to that of a paper based microbial fuel cell [53].

6.3.6 Electrochemical impedance spectra studies

The electrochemical impedance spectra (EIS) for the paper cells are recorded at various anolyte concentrations and constant catholyte concentration (0.3 M $K_2Cr_2O_7$ + 4 M H_2SO_4) with 0.18 mg cm^{-2} of MoO_3 NRs loading on both the electrodes. The Nyquist plots at open circuit conditions (OCV) are shown in Fig. 6.13(a) and at part load conditions (V_{cell} = 0.8 V) are shown in Fig. 6.13(b). The measurements are done in the frequency range of 1 MHz - 0.1 Hz, with a sinusoidal voltage perturbation of amplitude 10 mV.
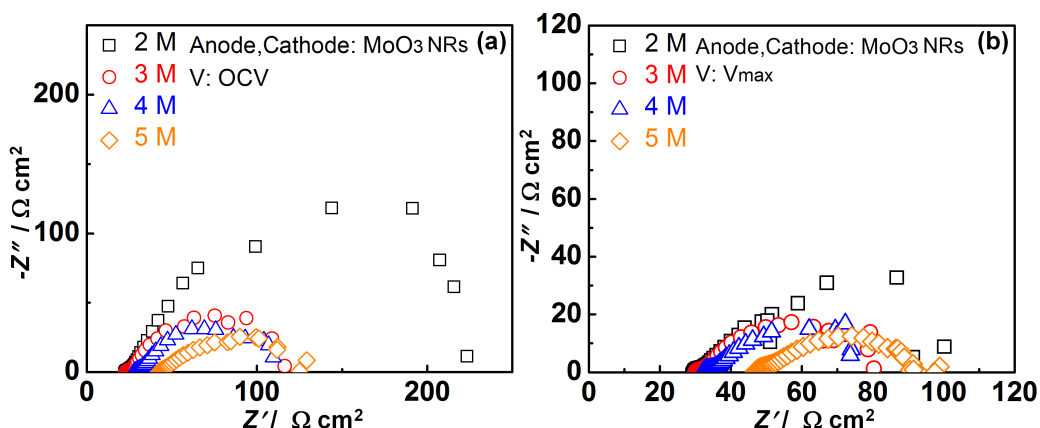
Figure 6.13: Electrochemical impedance spectra (EIS) of ethanol-dichromate fuel cell at (a) OCV and (b) $V_{cell} = V_{max} = 0.8$ V over a frequency scan range between 1 MHz-0.1 Hz at different fuel concentrations in 4 M H_2SO_4. MoO$_3$ NRs loading is 0.18 mg cm^{-2} at both the electrodes.

In both Fig. 6.13(a) and Fig. 6.13(b), only a single arc is observed in the EIS data, indicating that the relaxation frequencies of the anodic and the cathodic processes are of the same time scale. Slight scattering of data is observed in the low frequency regions. Ideally the EIS has to be recorded at steady state conditions, however, due to the eventual cross-over of the anolyte and catholyte over time, the cell voltage (or current in the case of potentiostatic mode) drops and does not allow the recording of EIS data under steady state conditions. The slight variations in the high frequency intercept is because of the variations in the fuel concentration, which leads to a change in the ohmic resistance of the cell.
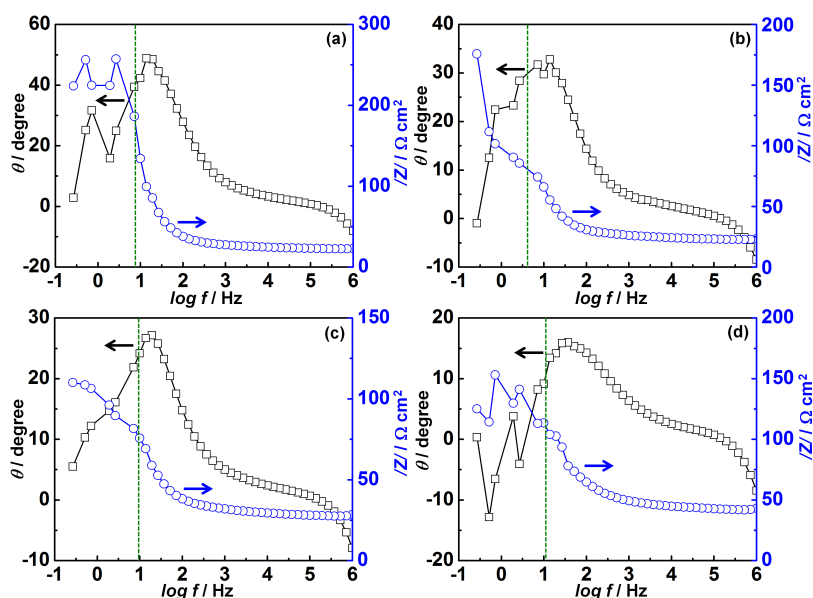
Figure 6.14: Bode phase plots of ethanol-dichromate fuel cell at OCV over a frequency range of 1 MHz-0.1 Hz at different fuel concentrations in 4 M H_2SO_4. Catalyst loading is 0.18 mg cm^{-2} at both the electrodes.

As explained earlier, the rate of cross-over of ethanol through the gel increases with increasing concentration, which alters the ionic conductivity of the Na-PSS/PVA/H$^+$ gel. The charge transfer resistance (R$_{ct}$) decreases with increase in concentration. For the measurements done at OCV, R$_{ct}$ is maximum at 2 M ethanol with 200.6 Ω-cm^2 due to sluggish kinetics at low concentrations and at 4 M ethanol the cell produces a minimum R$_{ct}$ of 81.7 Ω-cm^2, due to relatively faster kinetics. The trend is similar at V$_{cell}$=0.8 V; 2 M ethanol results in R$_{ct}$ of 70.63 Ω-cm^2 and 4 M ethanol leads to 41.37 Ω-cm^2. Ideally during fuel cell operation R$_{ct}$ decreases with increasing cell polarization [4, 129]. Thus the decrease in R$_{ct}$ observed here at V$_{cell}$=0.8 V is in accordance with typical fuel cell operation. The lower R$_{ct}$ at 4 M ethanol leads to better performance of the cell compared to other concentrations as observed in the dc-polarization measurements (Fig. 6.7). The internal resistance of the cell is the total resistance (R$_{total}$=R$_{ohm}$+R$_{ct}$), observed in the EIS spectra recorded at different fuel concentrations. Since the R$_{ohm}$ and R$_{ct}$ vary with the fuel concentration, R$_{total}$ varies from 80.3 Ω cm^2 to 100.4 Ω cm^2, as the ethanol concentration is varied from 2 M to 5 M. The Bode plots corresponding to Fig. 6.13(a) and Fig. 6.13(b) are shown in Fig. 6.14 and 6.15, respectively.
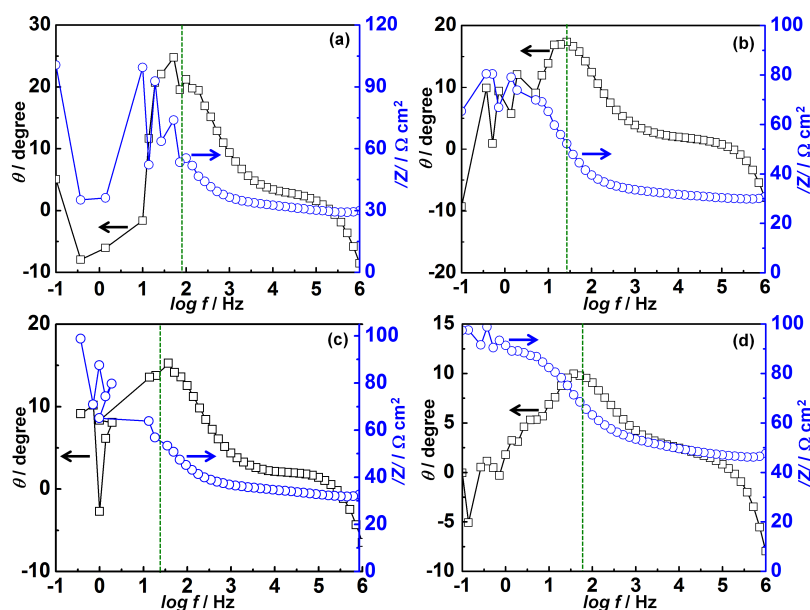
Figure 6.15: Bode phase plots of ethanol-dichromate fuel cell at V$_{cell}$=0.8 V over a frequency range of 1 MHz-0.1 Hz at different fuel concentrations in 4 M H$_2$SO$_4$. Catalyst loading is 0.18 mg cm^{-2} at both the electrodes.

The scattering of the data due to unsteady cell operation at low frequency is clearly evident in the Bode plots. The characteristic frequencies are marked in all the plots. In all cases, the phase angle corresponding to the characteristic frequency is below 45 degree, indicating that process can not be presented using a pure RC circuit. For pure RC circuits,

the phase angle reaches to 45 degree at the characteristic frequency. A small inductance component is observed at the high frequency limit, probably due to the wiring and contact, which becomes effective at frequencies around 100 kHz to 1 MHz. Although the inductance part is not shown in the Nyquist plot, the Bode representations, clearly show the presence of inductance.

The equivalent circuit for the T-shaped cell ethanol paper cell is also represented by the full Randles circuit as shown in Fig. 5.17. The circuit elements and the rationale for choosing them remains the same as explanied in Section 5.3.5. The relevant Nyquist plots are shown in Fig. 6.16 (a)-(d) and Fig. 6.17 (a)-(d). The simulated values are in good agreement with the experimental ones. The two semi-circles as seen across all the plots, represent two different processes occurring at the anode as the cathode side concentration is fixed
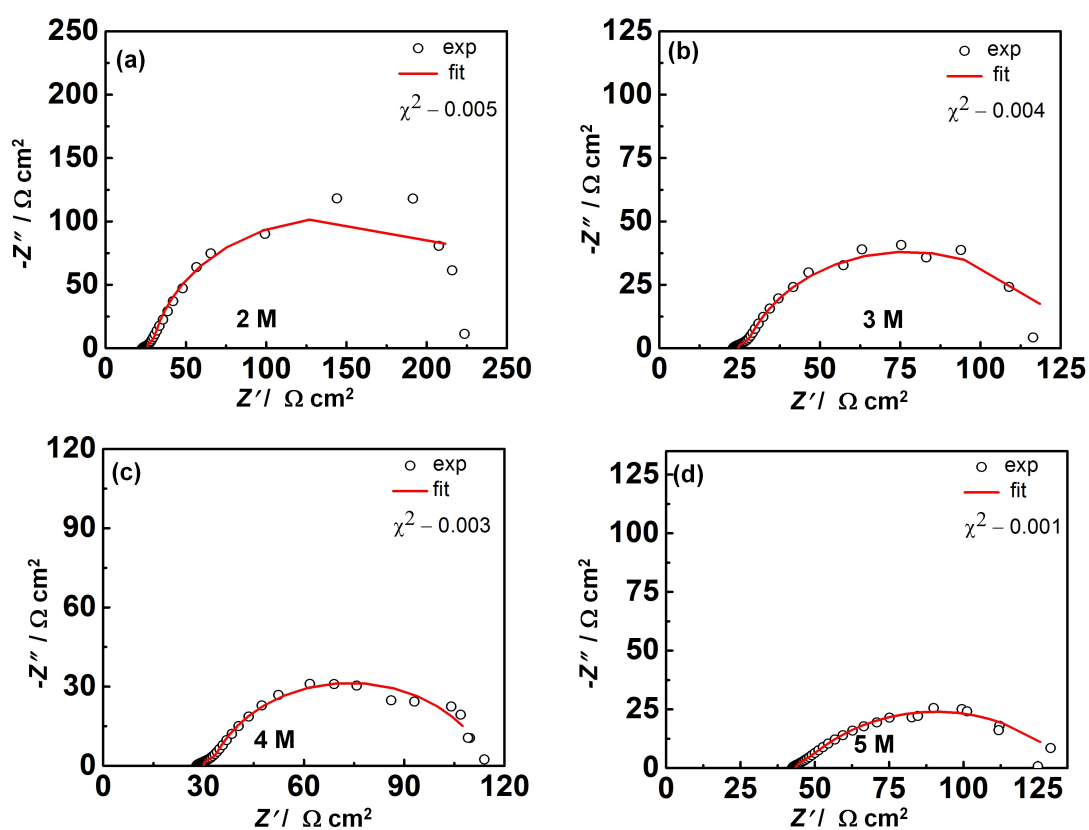
Figure 6.16: Electrochemical impedance spectra (EIS) of ethanol-dichromate fuel cell at OCV over a frequency scan range between 1 MHz-0.1 Hz at different fuel concentrations in 4 M H_2SO_4. MoO_3 NRs loading is 0.18 mg cm^{-2} at both the electrodes. Experimental data is represented by open symbols. Lines represent fitted/simulated results.
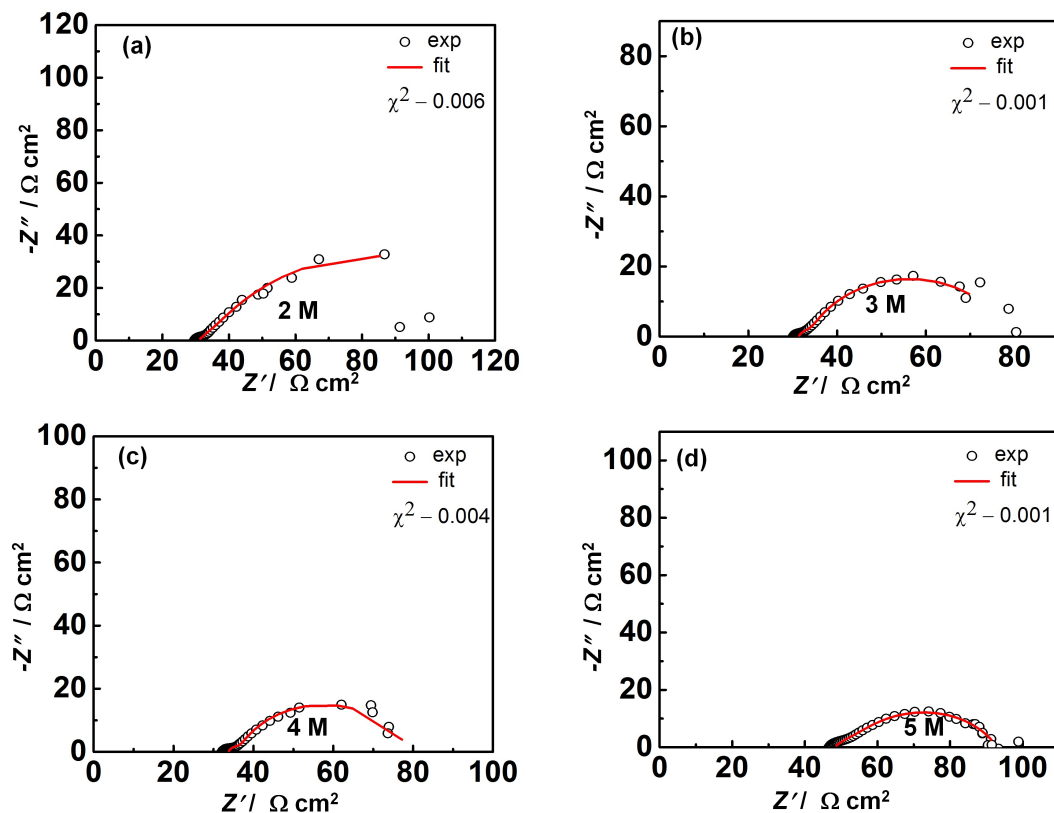
Figure 6.17: Electrochemical impedance spectra (EIS) of ethanol-dichromate fuel cell at V_{cell} = V_{max} = 0.8 V over a frequency scan range between 1 MHz-0.1 Hz at different fuel concentrations in 4 M H_2SO_4. MoO_3 NRs loading is 0.18 mg cm^{-2} at both the electrodes. Experimental data is represented by open symbols. Lines represent fitted/simulated results.

.

The capability of the paper based cell to power low power consuming devices for a short time is demonstrated by lighting a red LED. Two paper cells described in this work are stacked and then packed into a box-like acrylic scaffold designed and developed in our lab. Figure 6.18 shows the packaged cell in operation and illuminating an LED without any external bias.

For the purpose of stacking, the cells are supported in acrylic sheets with appropriately positioned holes for feeding the anolyte and the catholyte to the cells. A schematic representation of the cell assembly is shown in Fig. 6.18(b). The anolyte and catholyte are discharged using a dropper and crocodile clips are used to make the connections. The LED serves as a load for the cell. The output voltage of the cell as measured using a multimeter is 2.12 V. The overall current flowing through the cells connected in series is 4.1 mA. Since the cells are connected in series, the same magnitude of current flows through both

the cells. The cell assembly could power the LED for more than 40 minutes without the replenishing the anode and cathode with anolyte and catholyte.

This demonstration shows that this stack can be used for powering micro-analytical devices like a pregnancy test kit, glucometer, dengue detection kits and other visual monitoring based micro-nano devices. It can even replace the traditional non-rechargeable batteries which are typically used in such devices. Unlike the non-rechargeable batteries used in these devices, the fuel cell here can be easily revived by simply dispensing ethanol and dichromate solutions through the holes provided. These solutions can be provided in air-tight vials.
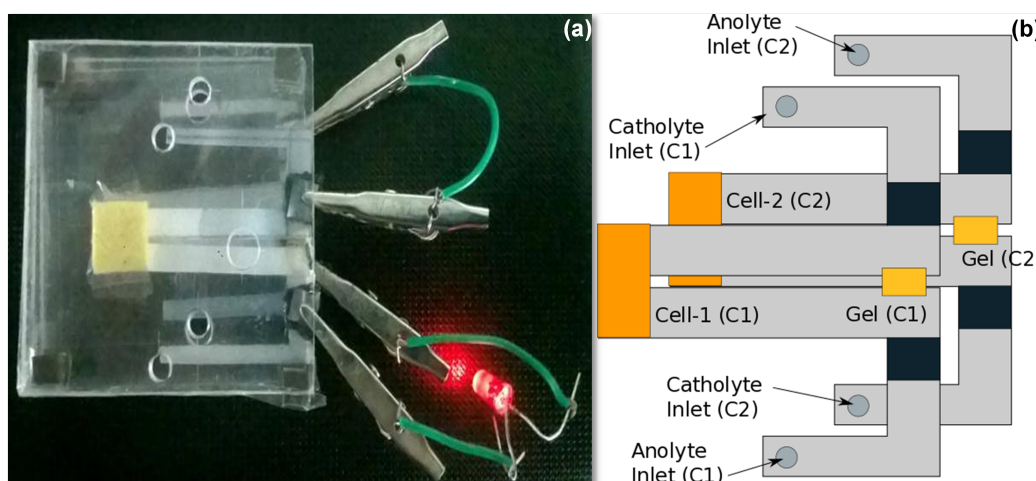
Figure 6.18: (a) Two paper cells stacked in series (dual cell stack), illuminating a LED, with an output cell voltage of 2.12 V (measured with multimeter). Anolyte is 4 M ethanol + 4 M H_2SO_4. Catholyte is 0.3 M $K_2Cr_2O_7$ + 4 M H_2SO_4. Catalyst loading is 0.18 mg cm^{-2} Mo$_3$ NRs. (b) A schematic of the dual cell stack assembly.

In order to establish the durability of the cell over a long period of 8 hours, the current density obtained from the cell is plotted against time with an interval of 2 hours and is shown in Fig. 6.19. Here, the anolyte (4 M ethanol) and catholyte (0.3 M $K_2Cr_2O_7$) were dispensed only once during each interval, and the measurements were done by chronoamperometry method under potentiostatic conditions, i.e., at a constant voltage of 0.2 V. It can be seen that the initial cell current density of 12 mA cm^{-2} is steady for 10 minutes, and the same trend is observed after an interval of 2 hours with a slight decrease in the current density, which further drops to 10.5 mA cm^{-2} at later times. The measurements recorded after 4 and 6 hours show trivial instability in the cell performance.
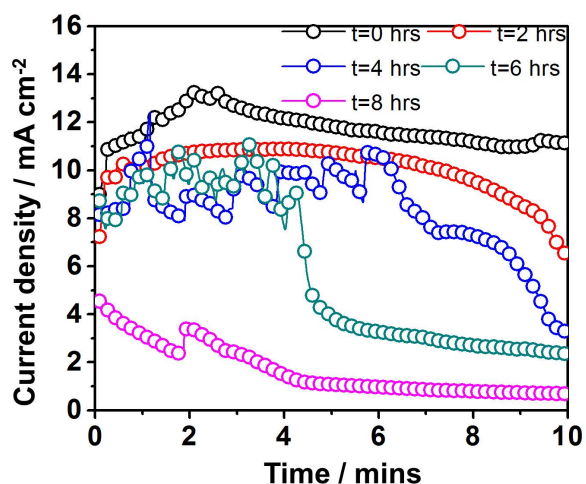
Figure 6.19: Durability of the paper based ethanol-dichromate fuel cell, with the operating voltage, V_{max}=0.2 V. The anolyte is 4 M ethanol + 4 M H_2SO_4. The catholyte is 0.3 M $K_2Cr_2O_7$ + 4 M H_2SO_4. The anode, cathode contain MoO_3 NRs.

Nevertheless, it is found that the cell could still deliver a current density of more than 9 mA cm^{-2} even after 6 hours. In addition to this, the image of the cell taken after one hour of operation is shown in Fig. 6.20. A change in the color of the dichromate loaded paper strip is expected after the redox reaction, but no color change is seen in Fig. 1(b) and (d) as these images were taken immediately after assembling the cell. At later times (after about an hour), since the electrolyte phase is H_2SO_4 (acidic), the possible by-product is $[Cr(H_2O)_6]^{3+}$, which leads to slight green color formation on the paper strip at the cathode side. The cell image showing the change in color of the paper strip is shown in Fig. 6.20(a). Similarly, a stack of two cells which was used to illuminate an LED, was left undisturbed for 24 hours and then the color of the paper strip was changed to green color as seen Fig. 6.20(b). We like to mention that when this cell was reused by dispensing the anolyte and the catholyte into the stack, it was able to illuminate the LED again. Besides these, we have also calculated the overall cost of the cell per mW to reaffirm its practical utility. The material cost for the fabrication of one ethanol-dichromate paper based cell with MoO_3 NRs catalyst is estimated to be 0.7 USD. The operational cost per mW would be 0.31 USD. A pack of two 3 V Li based coin cells which are generally employed in a glucometer cost around 2.9 USD. Since in our case, three paper cells are required to generate a voltage of 3 V (equivalent to a Li based coin cell), the cost for the three paper cells would be 2.1 USD. Furthermore, if large scale production of this device is considered, the material and operational costs are expected to drop significantly.
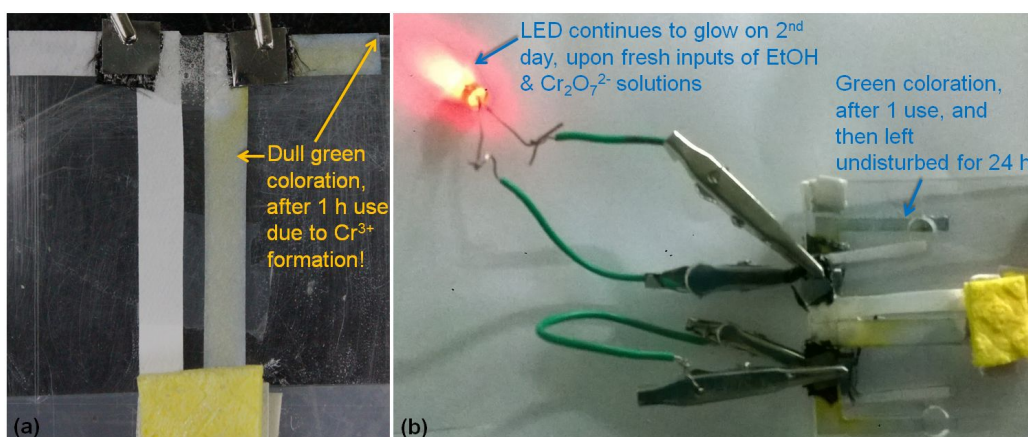
Figure 6.20: (a) Cell after 1 hour of operation. (b) Stack of two cells after 24 hours (while using second time).

6.4 Conclusions

Paper-based ethanol-dichromate fuel-oxidant microfluidic cells with ethanol as the fuel, dichromate as the oxidant, MoO_3 NRs as the anode-cathode catalyst and a Na-PSS/PVA/H$^+$ gel, were assembled and characterized by various electrochemical measurements. Hydrothermally synthesized MoO_3 NRs were characterized by electron microscopy confirming the formation of nanorods with crystalline orthorhombic lattice structure. The cell delivered an OCV of 1.42 V and 2.74 mW cm^{-2} peak power density without any catalyst loading using an anolyte containing 4 M ethanol and catholyte containing 0.3 M $K_2Cr_2O_7$. At the same conditions, with 0.18 mg cm^{-2} of MoO_3 NRs catalyst loading, the cell delivered an OCV of 1.42 V and a peak power density of 5.32 mW cm^{-2}. The cell voltage was more stable for a cell with MoO_3 NRs catalyst loaded at anode, as compared to cell without any catalyst. In order to further improve the cell performance, 0.18 mg cm^{-2} of catalyst was deposited on both the electrodes, and the power density increased to 6.32 mW cm^{-2}. Cyclic voltametry studies performed confirms the occurrence of multiple rate limiting charge transfer reactions at different voltages. Furthermore, the electroactive area increases with catalyst loading on the electrodes. EIS studies reveal that the polarization resistance of the cell increases with decrease in fuel concentration and the relaxation frequencies are of the same order for different cell processes. Finally the capability of the cell to power low power consuming devices is demonstrated by illuminating an LED using a stack of two cells connected in series and packaged into acrylic sheets based assembly. This clearly shows the potential of this cell as an alternative to batteries for powering micro-analytical devices.

Chapter 7

Summary and future studies

In an attempt to develop fuel cells supported on paper for small-scale power (milli-nano watt) generation, various paper based fuel cells with different fuel-oxidant pairs, namely-formic acid-permanganate, hydrazine-permanganate, methanol-permanganate and ethanol-dichromate, are investigated in this thesis. The paper cells are fabricated in two architectures-U-shaped (membraneless) and T-shaped (with gel membrane). In U-shaped paper cell, the slit delays the mixing and cross over of fuel/oxidant. In the T-shaped paper cell, the gel/membrane serves both as a barrier for fuel/oxidant cross over and as bridge for the transportation of ions while also imparting the ionic conductivity to the whole system. Polyacryl amide (PAM) and sodium polystyrene sulfonate (Na-PSS) are used as the gel/electrolyte in the T-shaped paper cell. Various non-noble metals are implemented as the catalysts in different morphologies, namely- Cu NPs, f-MWCNTs, Cu NPs@f-MWCNTs, $NiCo_2O_4$ (NCo), N-rGO, NCo@N-rGO and MoO_3 NRs. The presence of these catalysts helps in improving the electrochemical kinetics of the fuel/oxidant and hence enhance the overall cell performance. The maximum power density attained across all the paper cells is 6.32 mW cm^{-2}, which is delivered by the T-shaped ethanol-dichromate paper cell. This power density is sufficient for powering micro-nano devices for short-time operation. This is demonstrated by illuminating an LED by connecting two paper cells in series, which continues to glow for nearly 40 minutes. In addition to this, the cell performance for different fuel (methanol) concentration of the methanol-permanganate paper cell is predicted by a simple mathematical model based on Butler-volmer equation . The values predicted by the model and obtained by the experiments show good agreement. Based on the above findings, it can be concluded that the various paper based fuel cells investigated in this thesis could successfully generate sufficient and sustainable power for small-scale operation, i.e., for powering MNSs.

7.1 Future scope

The present study rises further questions and new areas to be investigated in future. This includes

- Exploring different redox couples with high OCV (> 1.5 V) and use of oxygen as the oxidant in paper based fuel cells. Since we aim to develop paper based fuel cells as on-board energy sources for point-of-care diagnostic devices, the use of ambient oxygen as the oxidant in these systems can reduce the storage and handling complexities of these systems.

- Synthesis and characterization of different noble and non-noble bimetallic catalysts (Pt-Ni, Pt-Co, Pt-Cu, Pd/Pt-Ni, Ni-Co, Ni-C, Co-C, Cu-c etc.), in different morphology, to promote the oxygen reduction reaction (ORR) at the cathode.

- Development of a commercial prototype of the paper based fuel cells, by employing various techniques of miniaturization (micro-machining, CO_2 laser cutting), wax impregnation of paper, electrode printing on paper.

- Studying the cell performance by changing the concentration of oxidant (O_2, $KMnO_4$, $K_2Cr_2O_7$, H_2O_2). In some cases, the cell performance can be dependent on the concentration of the oxidant more than the fuel. This investigation can throw some light on the role of different oxidants in the paper based fuel cell performance.

- Employing various analytical methods to find out the products formed at the anode and cathode (as result of the oxidation and reduction), in order to establish the corresponding reactions and the rate determining steps taking place at the electrodes. These can be used to formulate a physical/mathematical model that is relevant to the reaction kinetics taking place in the paper based fuel cell.

- Fabrication and characterization of laminar flow microfluidic fuel cells with micro-channels for fluid flow, consisting of catalyst sputtered electrodes. These catalyst can be nanoparticles of Pt, Au, Ag supported on different forms of carbon such as, graphene, reduced graphene oxide etc.

References

[1] S. Wang, L. Ge, Y. Zhang, X. Song, N. Li, S. Gea, and J. Yu. Battery-triggered microfluidic paper-based multiplex electrochemiluminescence immunodevice based on potential-resolution strategy. *Lab Chip* 12, (2012) 4489–4498.

[2] D. Dávila, A. Tarancón, C. Calaza, M. Salleras, M. Fernández-Regúlez, A. San Paulo, and L. Fonseca. Monolithically integrated thermoelectric energy harvester based on silicon nanowire arrays for powering micro/nanodevices. *Nano Energy* 1, (2012) 812–819.

[3] J. P. Esquivel, F. J. Del Campo, J. L. Gómez de la Fuente, S. Rojas, and N. Sabaté. Microfluidic fuel cells on paper: meeting the power needs of next generation lateral flow devices. *Energy Environ. Sci* 7, (2014) 1744 –1749.

[4] S. Lal, V. M. Janardhanan, M. Deepa, A. Sagar, and K. C. Sahu. Low cost environmentally benign porous paper based fuel cells for micro-nano systems. *J. Electrochem. Soc.* 162, (2015) F1402–F1407.

[5] N. Hashemi, J. M. Lackore, F. Sharifi, P. J. Goodrich, M. L. Winchell, and N. Hashemi. A paper-based microbial fuel cell operating under continuous flow condition. *Technology* 04, (2016) 98–103.

[6] E. Kjeang, N. Djilali, and D. Sinton. Microfluidic fuel cells: A review. *J. Power Sources* 186, (2009) 353–369.

[7] A. Kirubakaran, S. Jain, and R. Nema. A review on fuel cell technologies and power electronic interface. *Renew. Sust. Energ. Rev.* 13, (2009) 2430 – 2440.

[8] A. Kraytsberg and Y. Ein-Eli. Review of advanced materials for proton exchange membrane fuel cells. *Energy Fuels* 28, (2014) 7303–7330.

[9] O. Z. Sharaf and M. F. Orhan. An overview of fuel cell technology: Fundamentals and applications. *Renew. Sust. Energ. Rev.* 32, (2014) 810–853.

[10] W. R. W. Daud, R. E. Rosli, E. H. Majlan, S. A. A. Hamid, and R. Mohamed. PEM fuel cell system control: A review. *Renew. Energ.* 113, (2017) 620–638.

[11] F. Ning, X. He, Y. Shen, H. Jin, Q. Li, D. Li, S. Li, Y. Zhan, Y. Du, J. Jiang et al. Flexible and lightweight fuel cell with high specific power density. *ACS nano* 11, (2017) 5982–5991.

[12] S. K. Kamarudin, F. Achmad, and W. R. W. Daud. Overview on the application of direct methanol fuel cell (DMFC) for portable electronic devices. *Int. J. Hydrog. Energy* 34, (2009) 6902–6916.

[13] N. Nakagawa and Y. Xiu. Performance of a direct methanol fuel cell operated at atmospheric pressure. *J. Power Sources* 118, (2003) 248–255.

[14] M. Higa, S. Feng, N. Endo, and Y. Kakihana. Characteristics and direct methanol fuel cell performance of polymer electrolyte membranes prepared from poly (vinyl alcohol-b-styrene sulfonic acid). *Electrochim. Acta* 153, (2015) 83–89.

[15] A. Ozden, M. Ercelik, Y. Ozdemir, Y. Devrim, and C. O. Colpan. Enhancement of direct methanol fuel cell performance through the inclusion of zirconium phosphate. *Int. J. Hydrog. Energy* 42, (2017) 21,501–21,517.

[16] M. Bischoff. Molten carbonate fuel cells: A high temperature fuel cell on the edge to commercialization. *J. Power Sources* 160, (2006) 842–845.

[17] E. Audasso, L. Barelli, G. Bidini, B. Bosio, and G. Discepoli. Molten Carbonate Fuel Cell performance analysis varying cathode operating conditions for carbon capture applications. *J. Power Sources* 348, (2017) 118–129.

[18] A. B. Stambouli and E. Traversa. Solid oxide fuel cells (SOFCs): A review of an environmentally clean and efficient source of energy. *Renew. Sustain. Energ. Rev.* 6, (2002) 433–455.

[19] S. C. Singhal. Solid oxide fuel cells. *Interface* 16, (2007) 41.

[20] G. McLean, T. Niet, S. Prince-Richard, and N. Djilali. An assessment of alkaline fuel cell technology. *Int. J. Hydrog. Energy* 27, (2002) 507–526.

[21] F. Davis and S. P. Higson. Biofuel cellsrecent advances and applications. *Biosens. Bioelectron* 22, (2007) 1224–1235.

[22] V. Ramani. Fuel Cells. *Interface* 41–44.

[23] a. Husar, S. Strahl, and J. Riera. Experimental characterization methodology for the identification of voltage losses of PEMFC: Applied to an open cathode stack. *Int. J. Hydrog. Energy* 37, (2012) 7309–7315.

[24] J. Peters and M. Weil. A critical assessment of the resource depletion potential of current and future lithium-ion batteries. *Resources* 5, (2016) 46.

[25] J. Garche and L. Jürissen. Applications of fuel cell technology: status and perspectives. *Interface* 24, (2015) 39–43.

[26] T. Wilberforce, A. Alaswad, A. Palumbo, M. Dassisti, and A. G. Olabi. Advances in stationary and portable fuel cell applications. *Int. J. Hydrog. Energy* 41, (2016) 16,509–16,522.

[27] M. T. Gencoglu and Z. Ural. Design of a PEM fuel cell system for residential application. *Int. J. Hydrog. Energy* 34, (2009) 5242–5248.

[28] Kohlstruck. Applications with proton exchange membrane (PEM) fuel cells for a deregulated market place. *IEE conference publication* 4, (2001) 18–21.

[29] E. R. Choban, L. J. Markoski, A. Wieckowski, and P. J. Kenis. Microfluidic fuel cell based on laminar flow. *J. Power Sources* 128, (2004) 54–60.

[30] S. A. Mousavi Shaegh, N. T. Nguyen, S. H. Chan, and W. Zhou. Air-breathing membraneless laminar flow-based fuel cell with flow-through anode. *Int. J. Hydrog. Energy* 37, (2012) 3466–3476.

[31] D. R. Dekel. Review of cell performance in anion exchange membrane fuel cells. *J. Power Sources* 375, (2018) 158–169.

[32] R. Ferrigno, A. D. Stroock, T. D. Clark, M. Mayer, and G. M. Whitesides. Membraneless vanadium redox fuel cell using laminar flow. *J. Am. Chem. Soc.* 124, (2002) 12,930–12,931.

[33] K. S. Salloum and J. D. Posner. Counter flow membraneless microfluidic fuel cell. *J. Power Sources* 195, (2010) 6941–6944.

[34] E. Kjeang, J. McKechnie, D. Sinton, and N. Djilali. Planar and three-dimensional microfluidic fuel cell architectures based on graphite rod electrodes. *J. Power Sources* 168, (2007) 379–390.

[35] J. L. Cohen, D. J. Volpe, D. A. Westly, A. Pechenik, and H. D. Abruña. A dual electrolyte H_2/O_2 planar membraneless microchannel fuel cell system with open circuit potentials in excess of 1.4 V. *Langmuir* 21, (2005) 3544–3550.

[36] R. S. Jayashree, L. Gancs, E. R. Choban, A. Primak, D. Natarajan, L. J. Markoski, and P. J. Kenis. Air-breathing laminar flow-based microfluidic fuel cell. *J. Am. Chem. Soc.* 127, (2005) 16,758–16,759.

[37] H. B. Park, K. H. Lee, and H. J. Sung. Performance of H-shaped membraneless micro fuel cells. *J. Power Sources* 226, (2013) 266–271.

[38] H. Wang, S. Gu, D. Y. C. Leung, H. Xu, M. K. H. Leung, L. Zhang, and J. Xuan. Development and characteristics of a membraneless microfluidic fuel cell array. *Electrochim. Acta* 135, (2014) 467–477.

[39] E. R. Choban, J. S. Spendelow, L. Gancs, a. Wieckowski, and P. J. a. Kenis. Membraneless laminar flow-based micro fuel cells operating in alkaline, acidic, and acidic/alkaline media. *Electrochim. Acta* 50, (2005) 5390–5398.

[40] M. Gowdhamamoorthi, A. Arun, S. Kiruthika, and B. Muthukumaran. Enhanced performance of membraneless sodium percarbonate fuel cells. *J. Mater.* 2013.

[41] F. Chen, M.-H. Chang, and M.K. Lin. Analysis of membraneless formic acid micro-fuel cell using a planar microchannel. *Electrochim. Acta* 52, (2007) 2506–2514.

[42] J. I. Hur, D. D. Meng, and C.J. Kim. Self-Pumping Membraneless Miniature Fuel Cell With an Air-Breathing Cathode. *J. Microelectromech. Syst.* 21, (2012) 476–483.

[43] L. Sun, C. Liu, J. Liang, X. Zhu, and T. Cui. A self-pumping and self-breathing micro direct methanol fuel cell with polymer bipolar plates. *J. Power Sources* 196, (2011) 7533–7540.

[44] J. Esquivel, J. Buser, C. Lim, C. Domínguez, S. Rojas, P. Yager, and N. Sabaté. Single-use paper-based hydrogen fuel cells for point-of-care diagnostic applications. *J. Power Sources* 342, (2017) 442–451.

[45] S. M. Mousavi Ehteshami, M. Asadnia, S. N. Tan, and S. H. Chan. Paper-based membraneless hydrogen peroxide fuel cell prepared by micro-fabrication. *J. Power Sources* 301, (2016) 392–395.

[46] J. Esquivel, F. del Campo, J. G. de la Fuente, S. Rojas, and N. Sabaté. Paper-based microfluidic fuel cells. *17th International Conference on Miniaturized Systems for Chemistry and Life Sciences, MicroTAS* 2, (2013) 1251-1253.

[47] R. K. Arun, S. Halder, N. Chanda, and S. Chakraborty. A paper based self-pumping and self-breathing fuel cell using pencil stroked graphite electrodes. *Lab Chip* 14, (2014) 1661.

[48] C. Rice, S. Ha, R. Masel, and A. Wieckowski. Catalysts for direct formic acid fuel cells. *J. Power Sources* 115, (2003) 229–235.

[49] N. K. Thom, G. G. Lewis, M. J. DiTucci, and S. T. Phillips. Two general designs for fluidic batteries in paper-based microfluidic devices that provide predictable and tunable sources of power for on-chip assays. *RSC Adv.* 3, (2013) 6888.

[50] S.-S. Chen, C.-W. Hu, I.-F. Yu, Y.-C. Liao, and J.-T. Yang. Origami paper-based fluidic batteries for portable electrophoretic devices. *Lab Chip* 14, (2014) 2124–2130.

[51] A. Fraiwan and S. Choi. Bacteria-powered battery on paper. *Phys. Chem. Chem. Phys.* 16, (2014) 26,288–26,293.

[52] A. Fraiwan and S. Choi. A stackable, two-chambered, paper-based microbial fuel cell. *Biosens. Bioelectron.* 83, (2016) 27–32.

[53] A. Fraiwan, S. Mukherjee, S. Sundermier, H.-S. Lee, and S. Choi. A paper-based microbial fuel cell: Instant battery for disposable diagnostic devices. *Biosens. Bioelectron.* 49, (2013) 410–414.

[54] C. Fischer, A. Fraiwan, and S. Choi. A 3D paper-based enzymatic fuel cell for self-powered, low-cost glucose monitoring. *Biosens. Bioelectron.* 79, (2016) 193–197.

[55] R. Veerubhotla, A. Bandopadhyay, D. Das, and S. Chakraborty. Instant power generation from an air-breathing paper and pencil based bacterial bio-fuel cell. *Lab Chip* 15, (2015) 2580–2583.

[56] Z. Xu, Y. Liu, I. Williams, Y. Li, F. Qian, H. Zhang, D. Cai, L. Wang, and B. Li. Disposable self-support paper-based multi-anode microbial fuel cell (PMMFC) integrated with power management system (PMS) as the real time "shock" biosensor for wastewater. *Biosens. Bioelectron.* 85, (2016) 232–239.

[57] M.H. Chang, F. Chen, and N.S. Fang. Analysis of membraneless fuel cell using laminar flow in a Y-shaped microchannel. *J. Power Sources* 159, (2006) 810–816.

[58] C. A. López-Rico, J. Galindo-de-la Rosa, L. Álvarez-Contreras, J. Ledesma-García, M. Guerra-Balcázar, L. G. Arriaga, and N. Arjona. Direct Ethanol Membraneless Nanofluidic Fuel Cell With High Performance. *ChemistrySelect* 1, (2016) 3054–3062.

[59] M. Elumalaia, M. Priya, S. Kiruthikab, and B. Muthukumarana. Effect of acid and alkaline media on membrane less fuel cell using sodium borohydride as fuel. *Afinidad* 72.

[60] X. Yan, F. Meng, Y. Xie, J. Liu, and Y. Ding. Direct N_2H_4/H_2O_2 fuel cells powered by nanoporous gold leaves. *Sci Rep.* 2, (2012) 941.

[61] K. Kreuer. On the development of proton conducting polymer membranes for hydrogen and methanol fuel cells. *J Memb Sci* 185, (2001) 29–39.

[62] C. Rice, S. Ha, R. I. Masel, P. Waszczuk, A. Wieckowski, and T. Barnard. Direct formic acid fuel cells. *J. Power Sources* 111, (2002) 83–89.

[63] Y. Zhu, S. Y. Ha, and R. I. Masel. High power density direct formic acid fuel cells. *J. Power Sources* 130, (2004) 8–14.

[64] S. Ha, Z. Dunbar, and R. I. Masel. Characterization of a high performing passive direct formic acid fuel cell. *J. Power Sources* 158, (2006) 129–136.

[65] M. K. Jeon, J. Y. Won, K. S. Oh, K. R. Lee, and S. I. Woo. Performance degradation study of a direct methanol fuel cell by electrochemical impedance spectroscopy. *Electrochim. Acta* 53, (2007) 447–452.

[66] X. Yu and P. G. Pickup. Recent advances in direct formic acid fuel cells (DFAFC). *J. Power Sources* 182, (2008) 124–132.

[67] S. Tominaka, S. Ohta, H. Obata, T. Momma, and T. Osaka. On-chip fuel cell: micro direct methanol fuel cell of an air-breathing, membraneless, and monolithic design. *J. Am. Chem. Soc* 130, (2008) 10,456–7.

[68] J. Esquivel, N. Sabaté, J. Santander, N. Torres, and C. Cané. Fabrication and characterization of a passive silicon-based direct methanol fuel cell. *Microsyst. Technol.* 14, (2008) 535–541.

[69] S. Ali, M. Shaegh, N.T. Nguyen, and S. H. Chan. A review on membraneless laminar flow-based fuel cells. *Int. J. Hydrog. Energy* 36, (2011) 5675–5694.

[70] N. Kakati, J. Maiti, S. H. Lee, S. H. Jee, B. Viswanathan, and Y. S. Yoon. Anode catalysts for direct methanol fuel cells in acidic media: do we have any alternative for Pt or Pt–Ru? *Chem. Rev.* 114, (2014) 12,397–12,429.

[71] L. Wang, P. Gao, D. Bao, Y. Wang, Y. Chen, C. Chang, G. Li, P. Yang, Synthesis of crystalline/amorphous core/shell MoO3 composites through a controlled dehydration route and their enhanced ethanol sensing properties, Cryst. Growth Des. 14 (2) (2014) 569–575.

[72] A. De, J. Datta, I. Haldar, M. Biswas, Catalytic Intervention of MoO_3 toward Ethanol Oxidation on PtPd Nanoparticles Decorated MoO_3-Polypyrrole Composite Support, ACS Appl. Mater. Interfaces 8 (42) (2016) 28574–28584.

[73] M. A. F. Akhairi and S. K. Kamarudin. Catalysts in direct ethanol fuel cell (DEFC): An overview. *Int. J. Hydrog. Energy* 41, (2016) 4214–4228.

[74] B. C. Ong, S. K. Kamarudin, and S. Basri. Direct liquid fuel cells: A review. *Int. J. Hydrog. Energy* 42, (2017) 10,142–10,157.

[75] S. J. Lao, H. Y. Qin, L. Q. Ye, B. H. Liu, and Z. P. Li. A development of direct hydrazine/hydrogen peroxide fuel cell. *J. Power Sources* 195, (2010) 4135–4138.

[76] X.-B. Zhang, J.-M. Yan, S. Han, H. Shioyama, K. Yasuda, N. Kuriyama, and Q. Xu. A high performance anion exchange membrane-type ammonia borane fuel cell. *J. Power Sources* 182, (2008) 515–519.

[77] G. L. Soloveichik. Liquid fuel cells. *Beilstein J. Nanotechnol.* 5, (2014) 1399.

[78] E. Kjeang, A. G. Brolo, D. A. Harrington, N. Djilali, and D. Sinton. Hydrogen Peroxide as an Oxidant for Microfluidic Fuel Cells. *J. Electrochem. Soc.* 154, (2007) B1220.

[79] S. Lal, M. Deepa, V. M. Janardhanan, and K. C. Sahu. Paper based hydrazine monohydrate fuel cells with Cu and C composite catalysts. *Electrochim. Acta* 232, (2017) 262–270.

[80] R. Verma, S. Lal, M. Deepa, V. M. Janardhanan, and K. C. Sahu. Sodium Percarbonate Based, Mixed-Media Fuel Cells Supported on Paper with Gold/Nickel Oxide Catalysts. *ChemElectroChem* 4, (2017) 310–319.

[81] S. Durga, K. Ponmani, S. Thilaga, and B. Muthukumaran. A development of membraneless percarbonate/hydrazine fuel cell. *J. Mater. Environ. Sci* 5, (2014) 1611–1621.

[82] S. Ha, R. Larsen, and R. Masel. Performance characterization of Pd/C nanocatalyst for direct formic acid fuel cells. *J. Power Sources* 144, (2005) 28–34.

[83] H. Yang, X. Zhong, Z. Dong, J. Wang, J. Jin, and J. Ma. A highly active hydrazine fuel cell catalyst consisting of a NiFe nanoparticle alloy plated on carbon materials by pulse reversal. *RSC Adv.* 2, (2012) 5038.

[84] G. Karim-Nezhad, R. Jafarloo, and P. S. Dorraji. Copper (hydr) oxide modified copper electrode for electrocatalytic oxidation of hydrazine in alkaline media. *Electrochim. Acta* 54, (2009) 5721–5726.

[85] M. Hasanzadeh, G. Karim-Nezhad, N. Shadjou, B. Khalilzadeh, L. Saghatforoush, S. Ershad, and I. Kazeman. Kinetic study of the electro-catalytic oxidation of hydrazine on cobalt hydroxide modified glassy carbon electrode. *Chin. J. Chem.* 27, (2009) 638–644.

[86] E. Granot, B. Filanovsky, I. Presman, I. Kuras, and F. Patolsky. Hydrazine/air direct-liquid fuel cell based on nanostructured copper anodes. *J. Power Sources* 204, (2012) 116–121.

[87] B. Filanovsky, E. Granot, I. Presman, I. Kuras, and F. Patolsky. Long-term room-temperature hydrazine/air fuel cells based on low-cost nanotextured CuNi catalysts. *J. Power Sources* 246, (2014) 423–429.

[88] J. Gao, Y. Wang, Y. Ping, D. Hu, G. Xu, F. Gu, and F. Su. A thermodynamic analysis of methanation reactions of carbon oxides for the production of synthetic natural gas. *RSC Adv.* 2, (2012) 2358–2368.

[89] W. X. Yin, Z. P. Li, J. K. Zhu, and H. Y. Qin. Effects of NaOH addition on performance of the direct hydrazine fuel cell. *J. Power Sources* 182, (2008) 520–523.

[90] K. Yamada, K. Yasuda, N. Fujiwara, Z. Siroma, H. Tanaka, Y. Miyazaki, and T. Kobayashi. Potential application of anion-exchange membrane for hydrazine fuel cell electrolyte. *Electrochem commun.* 5, (2003) 892–896.

[91] A. Serov and C. Kwak. Direct hydrazine fuel cells: A review. *Appl. Catal. B Environ.* 98, (2010) 1–9.

[92] K. Asazawa, K. Yamada, H. Tanaka, M. Taniguchi, and K. Oguro. Electrochemical oxidation of hydrazine and its derivatives on the surface of metal electrodes in alkaline media. *J. Power Sources* 191, (2009) 362–365.

[93] H. Yang, X. Zhong, Z. Dong, J. Wang, J. Jin, and J. Ma. A highly active hydrazine fuel cell catalyst consisting of a Ni–Fe nanoparticle alloy plated on carbon materials by pulse reversal. *RSC Adv.* 2, (2012) 5038–5040.

[94] K. L. Stano, R. Chapla, M. Carroll, J. Nowak, M. McCord, and P. D. Bradford. Copper-encapsulated vertically aligned carbon nanotube arrays. *ACS Appl. Mater. Interfaces* 5, (2013) 10,774–10,781.

[95] H. Yin, H. Tang, D. Wang, Y. Gao, Z. Tang, L. Q. Ye, Z. P. Li, H. Y. Qin, J. K. Zhu, and B. H. Liu. Hydrazine electrooxidation on a composite catalyst consisting of nickel and palladium. *ACS nano* 6, (2011) 8288–8297.

[96] G. W. Yang, G. Y. Gao, C. Wang, C. L. Xu, and H. L. Li. Controllable deposition of Ag nanoparticles on carbon nanotubes as a catalyst for hydrazine oxidation. *Carbon* 46, (2008) 747–752.

[97] M. C. Denney, V. Pons, T. J. Hebden, D. M. Heinekey, and K. I. Goldberg. Efficient catalysis of ammonia borane dehydrogenation. *J. Am. Chem. Soc.* 128, (2006) 12,048–12,049.

[98] L. C. Nagle and J. F. Rohan. Ammonia borane oxidation at gold microelectrodes in alkaline solutions. *J. Electrochem. Soc.* 153, (2006) C773–C776.

[99] Y. Yang, F. Zhang, H. Wang, Q. Yao, X. Chen, and Z.H. Lu. Catalytic hydrolysis of ammonia borane by cobalt nickel nanoparticles supported on reduced graphene oxide for hydrogen generation. *J. Nanomater.* 2014, (2014) 30–38.

[100] O. Metin, V. Mazumder, S. Ozkar, and S. Sun. Monodisperse nickel nanoparticles and their catalysis in hydrolytic\dehydrogenation of ammonia borane Supporting Information. *J. Am. Chem. Soc* 132, (2010) 1468.

[101] L. Zhou, T. Zhang, Z. Tao, and J. Chen. Ni nanoparticles supported on carbon as efficient catalysts for the hydrolysis of ammonia borane. *Nano Res.* 7, (2014) 774–781.

[102] L. Yang, W. Luo, and G. Cheng. Graphene-supported Ag-based core-shell nanoparticles for hydrogen generation in hydrolysis of ammonia borane and methylamine borane. *ACS Appl. Mater. Interfaces* 5, (2013) 8231–8240.

[103] H. Liu, C. Song, L. Zhang, J. Zhang, H. Wang, and D. P. Wilkinson. A review of anode catalysis in the direct methanol fuel cell. *J. Power sources* 155, (2006) 95–110.

[104] M. Kamarudin, S. K. Kamarudin, M. Masdar, and W. R. W. Daud. Direct ethanol fuel cells. *Int. J. Hydrog. Energy* 38, (2013) 9438–9453.

[105] M. Jafarian, M. Mahjani, H. Heli, F. Gobal, H. Khajehsharifi, and M. Hamedi. A study of the electro-catalytic oxidation of methanol on a cobalt hydroxide modified glassy carbon electrode. *Electrochim. Acta* 48, (2003) 3423–3429.

[106] G. Chen, Y. Gao, and H. Zhang. Template-free synthesis of 3D hierarchical nanostructured $NiCo_2O_4$ mesoporous ultrathin nanosheet hollow microspheres for excellent methanol electrooxidation and supercapacitors. *RSC Adv.* 6, (2016) 30,488–30,497.

[107] A. K. Das, R. K. Layek, N. H. Kim, D. Jung, and J. H. Lee. Reduced graphene oxide (RGO)-supported $NiCo_2O_4$ nanoparticles: an electrocatalyst for methanol oxidation. *Nanoscale* 6, (2014) 10,657–10,665.

[108] M. Du, J. Sun, J. Chang, F. Yang, L. Shi, and L. Gao. Synthesis of nitrogen-doped reduced graphene oxide directly from nitrogen-doped graphene oxide as a high-performance lithium ion battery anode. *RSC Adv.* 4, (2014) 42,412–42,417.

[109] Y. Wang, S. Zou, and W.-B. Cai. Recent advances on electro-oxidation of ethanol on Pt-and Pd-based catalysts: From reaction mechanisms to catalytic materials. *Catalysts* 5, (2015) 1507–1534.

[110] L. T. Døssland. Electro-oxidation of ethanol at Pt electrodes with the use of a Dynamic Electrochemical Impedance Spectroscopy (DEIS) technique. Master's thesis, Institutt for materialteknologi 2012.

[111] H. A. Asiri and A. B. Anderson. Mechanisms for ethanol electrooxidation on Pt (111) and adsorption bond strengths defining an ideal catalyst. *J. Electrochem. Soc.* 162, (2015) F115–F122.

[112] A. Armenta-González, R. Carrera-Cerritos, A. Moreno-Zuria, L. Álvarez-Contreras, J. Ledesma-García, F. Cuevas-Muñiz, and L. Arriaga. An improved ethanol microfluidic fuel cell based on a PdAg/MWCNT catalyst synthesized by the reverse micelles method. *Fuel* 167, (2016) 240–247.

[113] A. Modjtahedi, A. Amirfazli, and S. Farhad. Low catalyst loaded ethanol gas fuel cell sensor. *Sens. Actuators B Chem* 234, (2016) 70–79.

[114] S. Carrión-Satorre, M. Montiel, R. Escudero-Cid, J. Fierro, E. Fatás, and P. Ocón. Performance of carbon-supported palladium and palladium ruthenium catalysts for alkaline membrane direct ethanol fuel cells. *Int. J. Hydrog. Energy* 41, (2016) 8954–8962.

[115] L. Wang, P. Gao, D. Bao, Y. Wang, Y. Chen, C. Chang, G. Li, and P. Yang. Synthesis of crystalline/amorphous core/shell MoO_3 composites through a controlled dehydration route and their enhanced ethanol sensing properties. *Cryst. Growth Des.* 14, (2014) 569–575.

[116] A. De, J. Datta, I. Haldar, and M. Biswas. Catalytic intervention of MoO_3 toward ethanol oxidation on Pt-Pd nanoparticles decorated MoO_3–polypyrrole composite support. *ACS Appl. Mater. Interfaces* 8, (2016) 28,574–28,584.

[117] W. Cai, L. Liang, Y. Zhang, W. Xing, and C. Liu. Real contribution of formic acid in direct formic acid fuel cell: investigation of origin and guiding for micro structure design. *Int. J. Hydrog. Energy* 38, (2013) 212–218.

[118] J. L. Cohen, D. A. Westly, A. Pechenik, and H. D. Abruña. Fabrication and preliminary testing of a planar membraneless microchannel fuel cell. *J. Power sources* 139, (2005) 96–105.

[119] M. Sun, G. V. Casquillas, S. Guo, J. Shi, H. Ji, Q. Ouyang, and Y. Chen. Characterization of microfluidic fuel cell based on multiple laminar flow. *Microelectron. Eng.* 84, (2007) 1182–1185.

[120] E. R. Chiban, L. J. Markoski, A. Wieckowski, and P. J. Kenis. Microfluidic fuel cell based on laminar flow. *J. Power Sources* 128, (2004) 54–60.

[121] T. M. D. Dang, T. T. T. Le, E. Fribourg-Blanc, and M. C. Dang. Synthesis and optical properties of copper nanoparticles prepared by a chemical reduction method. *Adv. Nat. Sci.: Nanosci. Nanotechnol.* 2, (2011) 015,009.

[122] M. S. Dresselhaus, A. Jorio, M. Hofmann, G. Dresselhaus, and R. Saito. Perspectives on carbon nanotubes and graphene Raman spectroscopy. *Nano letters* 10, (2010) 751–758.

[123] J. R. Ruffing. Quantifying individual losses in a direct methanol fuel cell. Ph.D. thesis, University of South Carolina 2014.

[124] P. Joghee, J. N. Malik, S. Pylypenko, and R. OHayre. A review on direct methanol fuel cells–in the perspective of energy and sustainability. *MRS Energy Sustain.* 2.

[125] J. S. Chen, Y. L. Cheah, S. Madhavi, and X. W. Lou. Fast synthesis of α-MoO$_3$ nanorods with controlled aspect ratios and their enhanced lithium storage capabilities. *J. Phys. Chem. C* 114, (2010) 8675–8678.

[126] Y. Wang, N. A. Lane, C.N. Sun, F. Fan, T. A. Zawodzinski, and A. P. Sokolov. Ionic conductivity and glass transition of phosphoric acids. *J. Phys. Chem. B* 117, (2013) 8003–8007.

[127] Y. Liang, Z. Cui, S. Zhu, Y. Liu, and X. Yang. Silver nanoparticles supported on TiO$_2$ nanotubes as active catalysts for ethanol oxidation. *J. Catal.* 278, (2011) 276–287.

[128] N. Abbasi, P. Shahbazi, and A. Kiani. Electrocatalytic oxidation of ethanol at Pd/Ag nanodendrites prepared via low support electrodeposition and galvanic replacement. *J. Mater. Chem. A* 1, (2013) 9966–9972.

[129] B. Prasad and V. M. Janardhanan. Modeling sulfur poisoning of Ni-based anodes in solid oxide fuel cells. *J. Electrochem. Soc.* 161, (2014) 208–213.